

Low frequency ultrasonic nondestructive inspection of
aluminum/adhesive fuselage lap splices

by

Thadd Clark Patton

A Thesis Submitted to the
Graduate College in Partial Fulfillment of the
Requirements for the Degree of
MASTER OF SCIENCE

Department: Aerospace Engineering and Engineering Mechanics
Co-Majors: Aerospace Engineering
Engineering Mechanics

Approved: /

Signature redacted for privacy

Iowa State University
Ames, Iowa

1993

TABLE OF CONTENTS

LIST OF FIGURES	iv
LIST OF TABLES	ix
NOMENCLATURE	x
CHAPTER I. INTRODUCTION	1
A. Background	1
B. The Boeing 510 Lap Splice	2
C. Current Inspection Techniques	2
1. Visual inspections	3
2. Mechanical impedance inspections	4
3. Eddy current inspections	4
4. Ultrasonic inspections	5
5. Previous efforts to improve ultrasonic pulse-echo inspections	6
a. Adhesive bond strength correlation	6
b. Improvements in basic research	7
c. Improvements in application	8
D. Improvements Still Needed	8
CHAPTER II. INITIAL ULTRASONIC INVESTIGATIONS	10
A. Ultrasonic Basics	10
1. Ultrasonic data acquisition	10
2. C-scan images	10
3. Image post-processing techniques	11
B. Boeing Lap Splice Samples	12
1. High frequency pulse-echo contact testing	13
2. High frequency immersion testing	17
3. Squirter testing	22
4. Low frequency immersion testing	22
CHAPTER III. THE LOW FREQUENCY INSPECTION TECHNIQUE	26
A. Introduction	26
B. The Technique	26
C. Realistic Aluminum/Adhesive Lap Splice Samples	27
D. Fatigue-Induced Disbond Detection	28
E. Corrosion Detection	30

1. Uniformly thinned corrosion samples	31
2. "Blow-out" samples	36
F. Low Frequency Parameter Study	39
1. Influence of focal spot size parameters on disbond detection	42
a. Influence of center frequency	42
b. Influence of frequency bandwidth	46
2. Influence of focal spot size parameters on corrosion detection	46
a. First layer corrosion detection	50
b. Second layer corrosion detection	53
3. Influence of motor step size on corrosion detection	55
4. Parameter study conclusions	56
G. RF Waveform Modeling	57
1. Complex amplitude reflection coefficient derivation	58
2. Modeling uniformly thinned lap splices	61
a. First layer metal thinning	64
b. Second layer metal thinning	64
CHAPTER IV. THE DRIPLESS BUBBLER	67
A. Comparisons with Other Techniques	67
B. Development of the Dripless Bubbler	68
1. Modified water squirter	69
2. Surface scans over flush mount riveted lap splices	71
3. Surface scans over raised surface features	72
C. Dripless Bubbler Membrane Material	74
D. Using the Dripless Bubbler	77
CHAPTER V. CONCLUSIONS	81
A. The Low Frequency Inspection Technique	81
B. The Dripless Bubbler	82
REFERENCES	84
ACKNOWLEDGMENTS	89
APPENDIX -- REFLECTION COEFFICIENT -- FORTRAN CODE	90

LIST OF FIGURES

Figure 1.1:	Schematic fuselage lap splice with cold bond adhesive strip and a three rivet row bonding area.	3
Figure 2.1:	Computer-controlled, ultrasonic data acquisition system.	11
Figure 2.2:	Schematic of the Boeing lap splice test samples showing disbond locations.	14
Figure 2.3:	20 MHz A-scan traces taken over (a) bonded and (b) disbanded regions of a lap splice.	15
Figure 2.4:	Schematic representation of reflection and transmission echoes that exist in (a) bonded and (b) disbanded lap splice.	16
Figure 2.5:	RF interference caused by two reflection echoes in a lap splice arriving at approximately the same time.	17
Figure 2.6:	High frequency (15 MHz) scan images of the (a) front side and the (b) back side of an adhesive lap splice.	18
Figure 2.7:	High frequency (15 MHz) scan images of the (a) front side and the (b) back side of a sealant bonded lap splice.	19
Figure 2.8:	Schematic example of glass/adhesive bond sample with Teflon™ inserts placed on top of the adhesive/scrim cloth layer.	21
Figure 2.9:	Pulse-echo C-scan images made using the PP amplitude of a 15 MHz 2BSE. The scan made from the front side of the glass sample (the side illustrated in Fig. 2.8) is shown on the left.	21
Figure 2.10:	High frequency (15 MHz) water squirter scan images of the (a) front side and the (b) back side of an adhesive lap splice.	23
Figure 2.11:	High frequency (15 MHz) water squirter scan images of the (a) front side and the (b) back side of a sealant bonded lap splice.	24
Figure 2.12:	Low frequency (1 MHz) pulse-echo RF waveform and time gate positions from an adhesively bonded lap-splice assembly.	24
Figure 2.13:	Low frequency (1 MHz) scan image of the back side of an adhesively bonded lap splice. Disbond is located behind the adhesive/scrim cloth layer.	25

Figure 3.1:	Low and high frequency C-scan images of a disbond in an aluminum/adhesive lap splice. (a) Scan of the front side with a 1 MHz transducer. (b) Scan of the front side with a 15 MHz transducer. (c) Scan of the back side with a 1 MHz transducer. (d) Scan of the back side with a 15 MHz transducer.	30
Figure 3.2:	Schematic example of an disbond located (a) above and (b) below the adhesive/scrim cloth layer.	31
Figure 3.3:	Experimental setup -- Electrochemical corrosion process configured for uniform metal thinning corrosion.	32
Figure 3.4:	Surface profile comparisons of skin samples produced by an electrochemical corrosion process and a skin sample taken from the belly section of a serviceable Boeing 727.	34
Figure 3.5:	Mean thickness reduction, deepest pit formation, and mean weight loss vs. corrosion reaction time for uniform metal thinning corrosion by an electrochemical process.	35
Figure 3.6:	Comparisons of RMS roughness vs. mean thickness loss for samples corroded by an electrochemical process and a sample taken from the belly section of a Boeing 727. Taken from the data of Fig. 3.4.	35
Figure 3.7:	Aluminum/adhesive lap-splice assemblies with scrim cloth and second layer corrosion. (a) Corrosion behind the scrim cloth layer on the interior side of the second layer, voids filled with aluminum powder to allow ultrasonic energy transmission. (b) Corrosion on the exterior side of the second layer.	36
Figure 3.8:	Experimental setup - Aluminum skin and platinum wire in a glass beaker, configured to produce a localized "blow-out" corrosion pit.	37
Figure 3.9:	Cross-sectional micrograph of localized "blow-out" corrosion pits. (a) Corrosion pit produced electrochemically. (b) Large corrosion pit taken from a Boeing 727 skin sample.	38
Figure 3.10:	C-scans of a localized corrosion pit on the second layer of an aluminum/adhesive lap splice. (a) Image of the overall RF signal amplitude with 1 MHz. (b) Image of the first BSE amplitude from the bottom skin with a 15 MHz pulse.	38
Figure 3.11:	1 MHz RF waveforms as reflected from a Ti block at their maximum peak-to-peak amplitude (a) Videoscan transducer. (b) Acuscan "S" series transducer.	40

Figure 3.12:	Fourier Magnitude of the RF waveforms shown in Fig. 3.11. (a) Videoscan transducer. (b) Acuscan “S” series transducer.	41
Figure 3.13:	Peak amplitude C-scans showing the fatigue-induced disbond area located along the left side of the aluminum/adhesive lap splice at different transducer broadband center frequencies. (a) 0.5 MHz. (b) 1.0 MHz. (c) 2.25 MHz. (d) 3.5 MHz. (e) 5.0 MHz.	43
Figure 3.14:	Color histograms of the images shown in Fig. 3.13. (a) 0.5 MHz. (b) 1.0 MHz. (c) 2.25 MHz. (d) 3.5 MHz. (e) 5.0 MHz.	44
Figure 3.15:	Peak amplitude C-scans showing the fatigue-induced disbond area occupying the left half side of the aluminum/adhesive lap splice as obtained with different frequency bandwidths. (a) Videoscan transducer. (b) Acuscan “S” series transducer.	47
Figure 3.16:	Color histogram of the images shown in Fig. 3.15. (a) Videoscan transducer. (b) Acuscan “S” series transducer.	48
Figure 3.17:	Side view of three samples containing first layer corrosion defects that give similar ultrasonic signatures. (a) Two aluminum skins fastened together with corrosion located interior to the splice and no adhesive bond. (b) Two aluminum skins fastened together with a disbond located between adhesive layer and the top corroded aluminum surface. (c) Single corroded aluminum skin.	49
Figure 3.18:	Lap splice with artificial second layer corrosion pits and disbond, shown in top and side views.	51
Figure 3.19:	Peak amplitude C-scans of a lap splice sample with first layer corrosion and no adhesive. (a) Videoscan transducer. (b) Acuscan “S” series transducer.	53
Figure 3.20:	Trailing signal peak amplitude C-scans of a lap splice sample with first layer corrosion and no adhesive. (a) Videoscan transducer. (b) Acuscan “S” series transducer.	53
Figure 3.21:	Peak amplitude C-scans of a bonded lap splice sample with second layer corrosion taken at 1 MHz broadband center frequency. (a) Overall amplitude signal @ 1 MHz. (b) Trailing signal @ 1 MHz.	54
Figure 3.22:	Peak amplitude C-scans of a bonded lap splice sample with second layer corrosion taken at 0.5 MHz broadband center frequency. (a) Overall amplitude signal @ 0.5 MHz. (b) Trailing signal @ 0.5 MHz.	55

Figure 3.23:	A 1 MHz peak amplitude C-scan showing the fatigue-induced disbond area located along the left side of the aluminum/adhesive lap splice. Reproduction of Fig. 3.13b at a larger step size.	56
Figure 3.24:	Peak amplitude C-scans of a bonded lap splice sample with second layer corrosion and a coarse motor step size. (a) Trailing signal @ 1.0 MHz. Reproduction of Fig. 3.21b with a larger step size. (b) Trailing signal @ 0.5 MHz. Reproduction of Fig. 3.22b with a larger step size.	57
Figure 3.25:	Procedural steps involved with the RF waveform model.	59
Figure 3.26:	Complex amplitude reflections from a single layer.	60
Figure 3.27:	Application of Eq. (3.9) to obtain the reflection coefficient from a three layered structure.	62
Figure 3.28:	1 MHz RF A-scan comparisons between experimental results and model predictions of aluminum/adhesive lap splices with uniform metal thinning in the second aluminum layer.	63
Figure 3.29:	Theoretical peak-to-peak signal amplitudes for an aluminum/adhesive lap splice assembly normalized to an uncorroded "reference" sample. (a) Corrosion thinning in the first layer. (b) Corrosion thinning in the second layer.	65
Figure 3.30:	Experimental pulse-echo C-scan images of corroded aluminum/adhesive lap splices taken with a 1 MHz pulse. (a) Corrosion interior to the first layer. (b) Corrosion interior to the second layer. (c) Corrosion exterior to the second layer.	66
Figure 4.1:	The first generation Dripless Bubbler scanning a flush-mount riveted aluminum lap splice in a vertical orientation.	72
Figure 4.2:	C-scan images of a Boeing 707 lap splice sample with flush-mount rivets using the overall amplitude of a 1 MHz pulse with the Dripless Bubbler. (a) Scan made in a vertical orientation as depicted in Fig. 4.1. (b) Scan made in an up-side-down orientation characteristic of an inspection made on the the belly section of an aircraft.	73
Figure 4.3:	Schematic view of the Dripless Bubbler.	75
Figure 4.4:	1 MHz RF pulses reflected from a reference titanium block. (a) No membrane. (b) Plastic food wrap. (c) Plastic heat shrink. (d) Latex condom.	76

Figure 4.5:	The Dripless Bubbler mounted at the end of an x-y handscanner and attached to the Foster-Miller panel.	77
Figure 4.6:	Close-up view of the Dripless Bubbler mounted at the end of an x-y handscanner. Seen are the guide rails used to provide a smooth scan motion and maintain a constant height above the sample surface.	78
Figure 4.7:	Close-up view of a hand scan image displayed on the portable computer and a RF signal displayed on an oscilloscope.	78
Figure 4.8:	Hand scanned C-scan image of a lap splice with flush mount rivets using the overall amplitude of a 1 MHz pulse.	79
Figure 4.9:	Hand scanned C-scan image of a repair patch with button head rivets using the overall amplitude of a 1 MHz pulse.	80

LIST OF TABLES

Table 2.1:	Characteristics of the fuselage lap splice test samples fabricated by Boeing	13
Table 3.1:	Characteristics of aluminum skin samples corroded with an electro-chemical corrosion process and a naturally corroded skin sample	34
Table 3.2:	Parameters of Videoscan focused-beam immersion transducers used for detection of a fatigue induced disbond in an aluminum/adhesive lap splice	45
Table 3.3:	Contrast coefficients between bonded and disbonded areas in an aluminum/adhesive lap splice at different broadband center frequencies, taken from the color histograms of Fig. 3.14	46
Table 3.4:	Parameters of Videoscan and Acuscan focused-beam immersion transducers used for detection of a fatigue induced disbond in an aluminum/adhesive lap splice at different frequency bandwidths	47
Table 3.5:	Contrast coefficients between bonded and disbonded areas in an aluminum/adhesive lap splice, at different broadband frequency bandwidths, taken from the color histograms of Fig. 3.16	48
Table 3.6:	Dimensions of artificial second layer corrosion pits	51
Table 3.7:	Parameters of Videoscan and Acuscan focused-beam immersion transducers used for detection of a first and second layer corrosion in an aluminum/adhesive lap splice	52
Table 4.1:	Acoustic transparency of three membranes using a 1MHz broadband RF pulse	76

NOMENCLATURE

ASTM	American Society of Testing and Materials
Boeing	Boeing Commercial Airplane Company
BSE	back surface echo
BW	beam half-width at the true focus point
CASR	Center for Aviation Systems Reliability
Douglas	McDonnell Douglas Airplane Company
F_o	geometric focal length
FAA	Federal Aviation Administration
FFT	fast Fourier transform
FSE	front surface echo
Hz	Hertz, cycles per second
IFT	inverse fast Fourier transform
ISU	Iowa State University
KHz	Kilo Hertz, $1.0e+03$ cycles per second
MHz	Mega Hertz, $1.0e+06$ cycles per second
MSD	multiple site damage
NAARP	National Aging Aircraft Research Program
NDI	nondestructive inspection
PA	peak amplitude
PE	pulse echo ultrasonics
PP	peak-to-peak
R	complex amplitude reflection coefficient
RF	radio frequency
SOP	standard operating procedure
TOF	time of flight
TU	Tuskegee University
TTU	through transmission ultrasonics
V	volts
W_o	Gaussian beam width at transducer face
Z	true focal length
c_L	longitudinal velocity
cm	centimeter

d	thickness, length
f	frequency
ft	foot
in	inch
k	Fourier transformed length
mil	0.001 inch
r	real reflection coefficient
t	time, real transmission coefficient
z	acoustic impedance factor = ρc_L
δ	phase factor = $4\pi\delta/\lambda$
λ	wavelength
π	radian measure
ρ	density
μsec	1.0e-06 second
2BSE	second back surface echo

CHAPTER I. INTRODUCTION

A. Background

The Federal Aviation Administration's (FAA) Center for Aviation Systems Reliability (CASR), located at Iowa State University (ISU), was established in 1990 in response to the Aviation Safety Act (Public Law 100-591) of 1988 [1]. The Aviation Safety Act, created primarily as the result of an in-flight mishap involving an Aloha Airlines' Boeing 737, mandated that the FAA develop research technologies to aid the aviation industry to (1) better predict the effects of design, maintenance, testing, wear, and fatigue life of an aircraft; (2) develop methods for improving aircraft maintenance technology and practices; and (3) expand general long-range research activities applicable to aviation systems [2,3].

In the Aloha Airlines accident a large section of the top forward fuselage was torn off in-flight. Fortunately, the damage to the structural integrity of the airplane was not catastrophic, and the flight crew was able to return the aircraft for a landing with minimal loss of life. Upon subsequent investigation it was determined that the primary cause of the accident was multiple site damage (MSD), undetected by the airline's maintenance procedures [4]. The Aloha Airlines mishap contributed to recognition of the aging aircraft problem, but as early as 1983 the symptoms of an aging air carrier fleet have been documented as a contributing cause in at least one other aircraft disaster [5]. By the turn of the century, 64 percent of the current aircraft fleet will be at least 20 years old [1,3]. With an ever aging air carrier fleet, efficient cost effective inspection and maintenance programs are necessary to extend the useful life of aircraft beyond their original design life.

Steve Bobo, in a 1989 lecture to the attendees of the Review of Progress in Quantitative Nondestructive Evaluation Conference, stated that:

Two short term inspection problems exist within the aircraft fleet: the need to reliably inspect large areas of rivets for the existence of MSD, and the ability to inspect extensive areas of fuselage for adhesive bond integrity in the presence of corrosion and other contaminants. . . .Existing methods for detecting adhesive bond (quality) are generally satisfactory in uncontaminated areas, but when corrosion, its by-products, or other contamination exist in riveted lap splices and butt doubler splices, detection of adhesive bond integrity becomes unreliable. [6]

Determining the integrity of the adhesive bond along the fuselage is seen as a preventive measure. When the adhesive in a riveted lap splice deteriorates through poor initial surface preparation, age, or chemical and corrosion contamination, the stress load previously main-

tained by the adhesive, transfers to the rivets. The chance of MSD greatly increases when the rivets are maintaining a majority of the stress loading in a lap splice [7].

An adhesive lap splice provides increased strength across the bonding surface and the need for additional fasteners should be eliminated [8]. To date, a reliable method does not exist to inspect the quality of a lap splice bond as the aircraft ages. Rivets are used to insure the strength of the lap splice, while the adhesive provides an additional factor of safety and a mechanism to seal the bondline. If a reliable determination of the adhesive bond quality in a riveted lap splice can be made, the progress of MSD from rivet to rivet can be reduced and a catastrophic failure may be averted.

B. The Boeing 510 Lap-Splice

During the 1970's, the Boeing Commercial Airplane Group (Boeing) attached the fuselage skins of their 727 and 737 passenger aircraft using the simple riveted lap splice configuration shown in Fig. 1.1. This lap splice configuration is referred to as the "Boeing 510 lap splice". Prior to 1971, the aircraft lap splices were cold-bonded with adhesive and scrim cloth. A sealant bonded lap splice was used in the aircraft manufactured after 1971. The change from adhesive to sealant was made after it was determined that a cold-bond adhesive was not very effective as a bonding agent. However, a seal was still needed to maintain cabin pressurization and prevent fluid contaminants from entering the splice area. Sealant has occasionally been used to repair the bondline of older aircraft that previously contained adhesive. There exists the possibility that some aircraft may contain a mixture of adhesive and sealant in their bondline [9].

C. Current Inspection Techniques

Scheduled maintenance, or preventive maintenance, is performed on a regular calendar basis and/or specified flight hour intervals. Scheduled maintenance is designed to prevent aircraft system and component failures by inspecting and replacing components before they reach the end of their life cycle. Between scheduled maintenance events, any maintenance performed on the aircraft is considered to be unscheduled. Component and systems failures comprise the bulk of unscheduled maintenance.

Scheduled maintenance is either mandated by the FAA or required by the aircraft manufacturers. The aircraft manufacturers determine the aircraft systems to inspect and/or replace

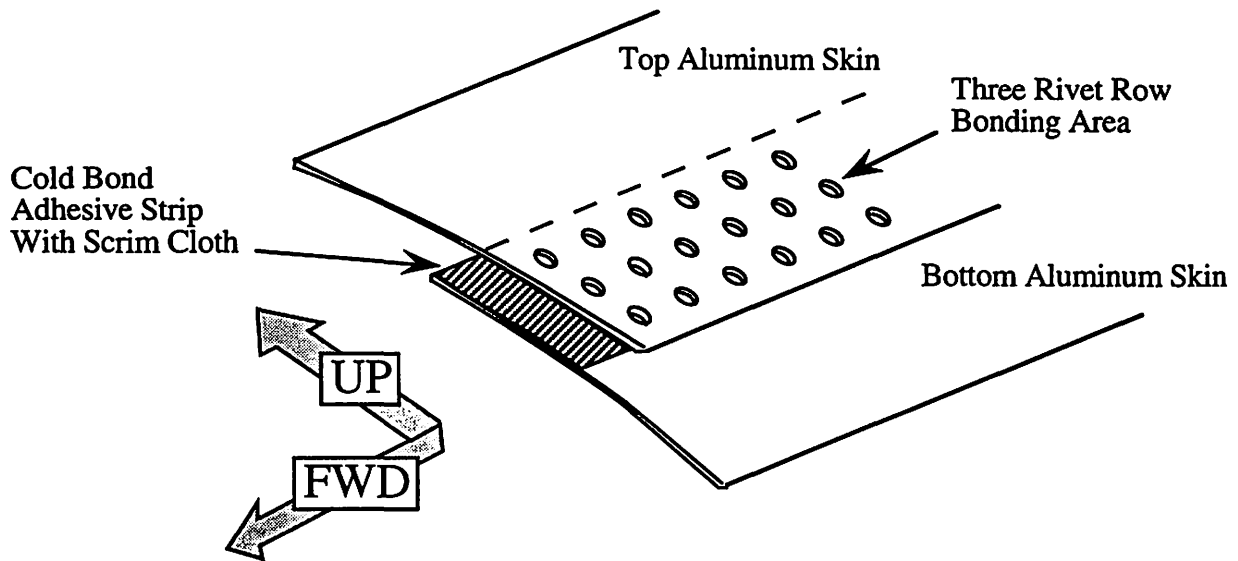


Figure 1.1: Schematic of fuselage lap splice with cold bond adhesive strip and a three rivet row bonding area.

and the maintenance schedules required on them. The role of the FAA, as a regulating agency, is to insure that the scheduled maintenance was completed and the appropriate paperwork maintained [10]. Air carriers only perform required inspections on the aircraft. There are certain legal issues that prevent air carriers from performing unauthorized inspections [11]. Air carriers prefer inspections that are quick, provide yes/no answers, and do not require the subjective judgment of the inspector. Air carriers may have their preferences, but the final judgment concerning inspection requirements is made by the aircraft manufacturers and the FAA while maintaining the best interests of the air carriers.

1. Visual inspections

The exterior fuselage of the aircraft is visually inspected by a member of the flight crew before and after each flight. The crew member glances over the fuselage for any obvious signs of impact damage such as bird strikes, rock chips, or ground handling equipment. The crew member also looks for paint blisters — indications of corrosion, and for fluid trails streaming out of the lap splices — indications of a possible disbond in the lap splice. Other than these quick walk-around visual inspections, no other inspections of the fuselage are made by the flight crew. When the aircraft reaches a scheduled maintenance period, a more detailed inspection of the fuselage may be made.

In the hangar, the fuselage of an aircraft can be inspected using any one of several different techniques. The technique choice depends upon the scheduled maintenance requirements of the aircraft at that time. A visual inspection is the simplest and least costly. This inspection is made much the same way as the member of the flight crew does. The difference being that an inspector now examines the fuselage from an arm's length away while the flight crew member looks at the fuselage as they walk around the aircraft. At certain inspection intervals, a visual inspection is made from the interior side of the aircraft as well as from the exterior. Many fuselage defects are found with a visual inspection; however a visual inspection can not detect a fuselage defect until its presence becomes known through other clues [12]. Interior lap splice corrosion is an example of a lap splice defect that often times can not be detected with a visual inspection. Corrosion hidden in the interior of a lap splice usually does not manifest itself until it has entirely corroded through the skin; thus its detection must be determined using other nondestructive inspection (NDI) techniques.

2. Mechanical impedance inspections

Along with hidden corrosion, a visual inspection can not determine the quality of the adhesive bond in a lap splice. Low frequency (1 to 10 KHz range) sonic methods (mechanical impedance methods) are currently the only established means available to determine bonding quality [13]. Sonic devices use mechanically induced sinusoidal excitations to locally strain the lap splice. Changes in surface particle velocity, material stiffness and, mass, as a function of signal amplitude and phase, are measured between the transmitting and receiving transducers [14]. The technique can also be used to detect bonding defects in composite and honeycomb layered structures. Sonic methods are primarily oriented towards a single point inspection. Inspections of large areas of a fuselage are possible, yet very time consuming and likewise expensive to perform.

3. Eddy current inspections

Eddy current methods are employed to inspect aircraft fuselage lap splices for the presence of cracks and metal thinning due to corrosion. Eddy current methods perform well on conducting materials such as the aluminum skins, but suffer from a lack sensitivity in non-conducting materials such as adhesives and composites. Thus, eddy current methods are not sensitive to adhesive bond quality; however they can be used to determine the bondline thickness between the aluminum skins [15]. There are two accepted techniques currently

used to inspect fuselage lap splices. A line scan technique is used to detect metal thinning due to corrosion, and a rotating probe technique is used to detect cracks emanating from rivet holes.

Line scans are performed by sliding an eddy current probe horizontally between a row of rivets using a straight edge as a guide. Lift-off of the probe is maintained by direct contact between the eddy current probe and the aircraft skin. Cracks, characteristic of MSD, usually run horizontally along the rivet row, thus a sliding probe inspection primarily checks for metal thinning due to corrosion in the top aluminum skin (first layer corrosion). Detection of second layer metal thinning due to corrosion is possible, however its acceptance as a standard inspection procedure has not yet been established by the airline manufacturers [16]. A rotating eddy current probe inspection detects cracking emanating from a rivet hole. It has been determined that this inspection is necessary only around rivets located in the top row of the fuselage lap splice — where MSD cracks generally start.

4. Ultrasonic inspections

The current inspection of aircraft fuselage lap splices using ultrasound has been directed toward skin thickness gauging. The inspections are typically high frequency, (> 10 MHz) single point direct contact styles, and are often times only used to verify eddy current results [12]. Direct contact, single-sided, pulse-echo (PE) inspections are made by placing a single transducer coupled directly onto the aluminum skin. A stress wave pulse is sent into the lap splice and reflection echoes are received back at the transducer and recorded. Prior knowledge about the character of the lap splice such as its layer velocities, thicknesses, and densities can be combined with the received radio frequency (RF) signal to determine the material properties, uniformity, and quality of adhesive bond. When used by properly trained individuals, ultrasound can provide a great deal of information about the integrity of the fuselage lap splice.

The ultrasonic inspection of lap splices has not gained the acceptance of air carriers because it is very difficult to obtain a reliable contact data over large areas of the fuselage. The received RF signal is influenced by couplant, surface conditions, and pressure applied to the transducer. Contact style inspections of the fuselage are hampered by the many rivets placed every inch or so apart. The problems associated with rivets and other surface protrusions can be eliminated by using a noncontact style of inspection such as an ultrasonic water

squirter system. A water squirter is considered to be a “noncontact” ultrasonic inspection because the transducer is not directly in contact with the lap splice. The transducer is coupled to the lap splice by a column of water sprayed onto the lap splice, while the ultrasonic pulse is collimated within the water stream.

5. Previous efforts to improve ultrasonic pulse-echo inspections

Despite its short comings, ultrasound holds promise as a tool to inspect fuselage lap splices and a considerable amount of time and money has been invested into its research. Efforts to improve the ultrasonic inspections of fuselage lap splices have been concerned with either improving the ultrasonic technology through basic research on laboratory lap splice samples or improving the means to apply the technology on the aircraft.

Nondestructive inspection of adhesive bonding is not a recent topic created because of the FAA’s interest in aging aircraft. Many individuals have contributed to the current knowledge base in the areas of the adhesion process, adhesive bond strength testing, and NDI of bonded structures. It should be noted that none of the aforementioned areas have been sufficiently resolved so that adhesive bonding can become a completely reliable structural alternative [17]. It is not the intention of this thesis to provide an exhaustive review of all ultrasonic research performed on adhesively bonded structures. Review papers discussing adhesive bond research using ultrasonics and other NDI techniques can be found in Refs. [18-26]. In the interests of brevity, only longitudinal wave, PE ultrasonic techniques will be discussed. It has been shown that with PE ultrasonics, the thickness, chemical composition, and cure state of the adhesive can be determined. Pulse-echo techniques, over other ultrasonic techniques, have the distinct advantage of being easily adaptable to one-sided, computer-controlled scanning systems.

a. Adhesive bond strength correlation

It is generally accepted that a “good” adhesive bond is one that maintains its structural requirements. During the life of a bonded structure, a “good quality” adhesive bond refers to a bond that is free of bondline defects such as debonds, delaminations, voids, etc. The true strength of an adhesive bond can only be measured destructively [27]. It would be reasonable to assume that a high strength adhesive bond would be one with good adhesive bond quality; thus far no consensus exists on defining bond quality in a quantitative manner based

upon defect content and location, mechanical strength, and durability data [17, 28]. However, the strength of an adhesive bond, measured destructively, can be correlated with adhesive bond quality by comparing features of an ultrasonic pulse reflected from well-bonded adhesive lap splice samples against the same features reflected from samples containing simulated bond defects.

It is assumed that the performance of an adhesive bond is related to its adhesive strength (failure likely to occur at the interface between the adhered and the adhesive) and its cohesive strength (failure likely to occur in the adhesive layer). With this knowledge, a generalization can be made about the quality of the adhesive bond. Adhesive strength can be monitored (not directly measured) by using PE reflection echoes within the lap splice layers. The amplitude and phase of each reflection echo contain information about the quality of the adhered/adhesive interfaces (at the locations measured). The cohesive strength of the adhesive can be inferred through ultrasonic velocity and attenuation measurements of its bulk properties. It is assumed here, that an adhesive consistent in bulk properties can be measured from one that is not, without other unknown parameter influences. It was shown in Ref. [29] that the ultrasonic velocity and attenuation measurements can be correlated to the cohesive quality of the bond. The condition of the adhesive can be monitored as it cures and during its service life in environmentally degrading conditions [30,31].

b. Improvements in basic research

Time-domain reflection echo techniques use the knowledge that an ultrasonic pulse reflected from a well-bonded adhesive lap splice is dependent upon the acoustic mismatch between the aluminum and adhesive layers. The acoustic mismatch can be easily calculated from the individual layer acoustic impedance. A substandard adhesive bond will reflect a greater portion of the ultrasonic energy back due to the presence of bondline defects or interface contamination. Either the amplitude of the reflected signal from the adhered/adhesive interface is directly monitored, or the ratio of the reflected interface signal to the front surface echo is monitored. Adhesive bondline defects such as disbonds and delaminations are generally determined through reflection echo inspections. Reflection echoes have also been used to ultrasonically discriminate between aluminum/adhesive lap splices whose aluminum surfaces were properly prepared for bonding (surface etching) from those that were not prepared at all [32].

Thickness measurements of the top aluminum skin are possible with knowledge of the longitudinal velocity in the aluminum and the measurements of the time differentials in subsequent top aluminum skin reflection echoes. Normally, thickness measurements require that the ultrasonic wavelength be less than the thickness of the material under investigation (resolved echoes); however resonance wavelength inspections have also been used to accurately measure the thickness of the adhesive layer [33].

The ultrasonic inspection process can be improved by incorporating signal processing techniques and pattern recognition algorithms. Several researchers have used features of the time-domain waveforms and frequency domain spectra compared on lap splice samples with and without adhesive and/or adhered defects. Some of the processes can discriminate between “good” and “bad” lap splices with over a 90 percent reliability [34]. Even though the comparisons have been between laboratory prepared lap splice sample, their contributions however, to the inspection process can not be ignored.

c. Improvements in application

Many of the recent improvements in adhesive bond research have been aimed toward improving basic research, but there have been some commercial developments toward applying ultrasound onto aircraft fuselages. Several commercially available scanners now allow for ultrasonic and eddy current C-scan image maps to be made of the fuselage bonding area [35]. The scanners are attached to the fuselage with suction cups and/or vacuum attachments. The scanners remain temporarily fixed onto the fuselage so that position encoders can properly coordinate scan position with received signal. The probe end of these scanners glides over the surface of the lap splice maintaining direct contact with the surface. These scanners work well on fuselage lap splice areas with flush mount rivets; however direct contact style of inspections are very difficult and in some instances impossible because of raised surface features.

D. Improvements Still Needed

Ultrasonic inspection techniques, other than thickness gauging, can be used to inspect aircraft fuselage lap splices. Ultrasound will probably never replace eddy current as the preferred inspection technique for detecting cracks and metal thinning due to corrosion in aluminum (conducting) structures. Ultrasound does, however, hold promise as an inspection

tool for determining adhesive bond quality and the inspection of composite parts, supplementing in areas where eddy current does not fare as well. No NDI technique does everything and it is unwise to think that one will. A reliable ultrasonic technique will supplement the current library of possible NDI techniques that can be used.

Assessing the quality of adhesive bonding is a preventive maintenance measure. A well-bonded lap splice prevents fluids and other contaminants from entering into the lap area, retarding corrosion decay. Preventive maintenance is an expensive but necessary requirement that must be undertaken and its importance can not be ignored. Any comprehensive inspection takes time and money to perform. The goal of an NDI technique is to prevent or at least reduce unnecessary maintenance costs.

Improving the inspection process only reduces the probability of a catastrophic failure — it does not prevent them. Currently, the National Aging Aircraft Research Program (NAARP) is concentrating its efforts on aircraft manufactured earlier than 1980. At that time, composite structures were not used as extensively as they are today. Interviews conducted with NDI representatives from five of the nation's major air carriers revealed that composite inspection is an area where further research attention should be directed by the FAA [36]. It would be advantageous to have several NDI techniques available to inspect composite structures when these aircraft are operated beyond their service life and enter the ranks of aged aircraft.

This thesis is a coalition of research works performed at ISU for the NAARP directed at determining the adhesive quality of an adhesive lap splice through ultrasonic NDI techniques. The lap splice samples used through out this work are designed to simulate the Boeing 510 lap splice, complete with scrim cloth, primers, and rivets. The objective of the research is to provide the airline maintenance community with a simple and reliable ultrasonic inspection technique that can be used in the presence of bondline contaminants, and a means for applying the technique on an aircraft fuselage inspection in a practical and cost effective manner.

CHAPTER II. INITIAL ULTRASONIC INVESTIGATIONS

A. Ultrasonic Basics

This first section is provided for the benefit of those not familiar with ultrasonic measurement methods and terminology. It is not intended to be an all encompassing description of ultrasonic inspection, but rather a brief description of the ultrasonic data acquisition and image post processing techniques used in support of the research described herein. Thorough discussions concerning ultrasonic experimental methods and image processing techniques can be found in Refs. [37-39].

1. Ultrasonic data acquisition

The ultrasonic data for this research was acquired using one of several systems available at ISU. Each system is slightly different, but all consist of various combinations of an ultrasonic transducer, a spike voltage pulser/receiver, and a digitizing device controlled by a personal computer as shown in Fig. 2.1. The pulser/receiver produces a very high voltage pulse (> 200 Volts) in a very short time (< 10 nsecs) to a broadband frequency ultrasonic transducer. The ultrasonic transducer, in a loose definition, changes electrical energy into mechanical energy and vice-versa. The transducer sends a stress wave into a test sample and reflected waves return to the transducer where they are converted into RF signals (voltage versus time). The received RF signal (waveform)-is captured using a digitizing device synchronized with the spike voltage pulser/receiver. If necessary, the digitized waveforms are stored in a data file for later use. A single ultrasonic waveform, measured at one location on the sample, is referred to as an A-scan. With the aid of a motor position controller, several adjacent A-scan inspections can be combined to form a C-scan image. A C-scan image is a color or gray scale representation of a RF signal feature within a time gate, displayed in two dimensional spatial coordinates. Many images of the lap splice can be created during a single C-scan, each one containing information specific to its time gate.

2. C-scan images

The data acquisition systems generate (0-255) color-scaled C-scan images (shown in this report as gray-scaled images) by time-gating a feature of the received pulse-echo ultrasonic signal as the transducer moves over the sample in an x-y spatial grid. In this research two C-scan images are used: peak amplitude (PA) and time of flight (TOF). Peak amplitude images

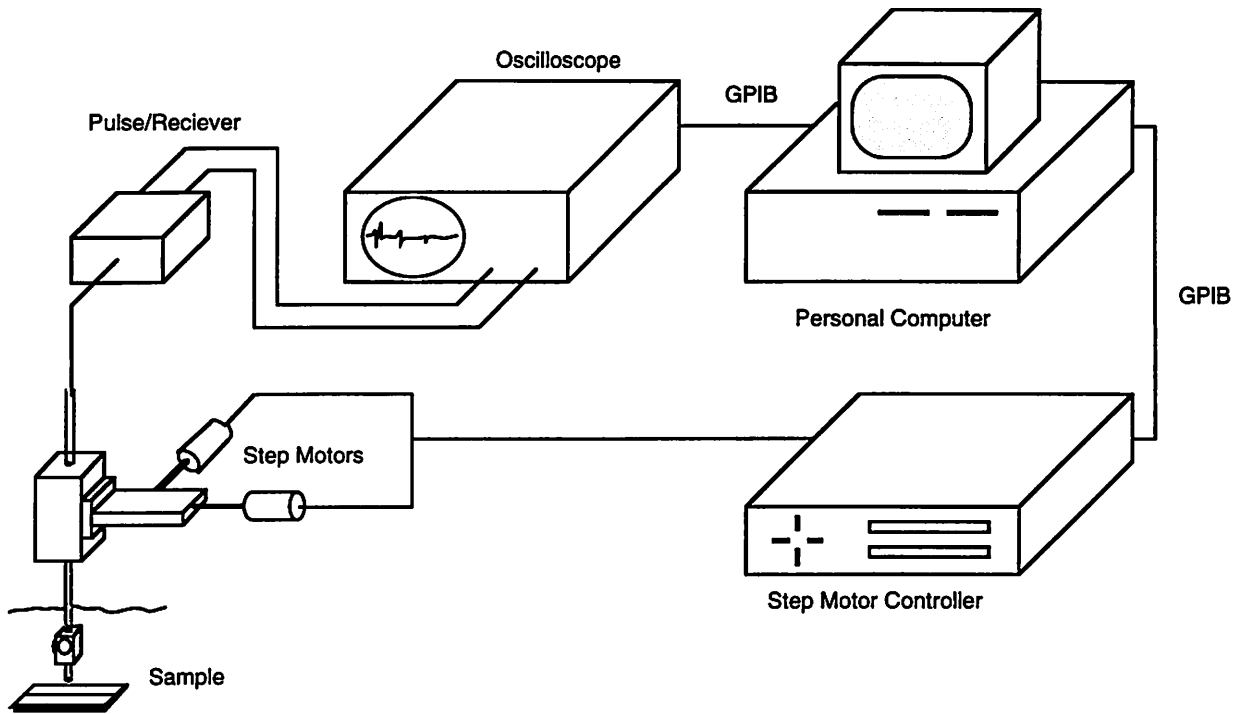


Figure 2.1: Computer-controlled, ultrasonic data acquisition system.

are color-scaled representations of the maximum signal amplitude that occurred within the time gate at a particular x-y position over the sample. Time-of-flight images are color-scaled representations of the position within the time gate that the peak amplitude signal occurred. In the peak amplitude images, 0 is representative of a low voltage (white color) and 255 is representative of a high voltage (black color). In the time-of-flight images, 0 represents a maximum amplitude signal that occurs at the beginning of the time gate, while 255 represents a maximum amplitude signal occurring at the end of the time gate.

3. Image post processing techniques

The technique described herein relies upon the simple image processing techniques of contrast and brightness enhancements. Image contrast enhancements linearly compress or expand the color spectrum (scale), while brightness enhancements linearly shift the color spectrum brighter or darker. The operations of these adjustments are analogous to the contrast and brightness adjustments found on most television sets and computer monitors.

In this report all images are shown as contrast-enhanced gray-scaled images for the purposes of publication and photo duplication. The (0-255) color assignments were created using a feature of the RF signal and are not based upon the choice of color spectrum used for display.

B. Boeing Lap Splice Samples

In 1988 Boeing fabricated a set of 32 laboratory test samples simulating the fuselage lap splice found on their older 727 and 737. The samples were designed as a means for comparing a through transmission ultrasonic (TTU) inspection with commercially available bond testers. The samples, listed in Table 2.1, contain various combinations of defects, aluminum skin thickness and bonding conditions. A schematic representation of the lap splice samples listed in Table 2.1 can be seen in Fig. 2.2. Interior corrosion defects were created by spraying the interior side of the aluminum skins with a salt spray for two weeks. Water was introduced into the bondline by immersing the fully assembled lap splices in a bucket of water for two weeks. (Boeing engineers did not see any effects due to corrosion or water in the bondline in their testing.) Disbonds of dimensions 4.0 x 3.0 in (10.2 x 7.62 cm) or 1.0 x 3.0 in (2.54 x 7.62 cm) were fabricated into the lap splice test samples during the assembly process. Disbonds in the adhesive/scrim cloth samples were created by inserting a layer of Teflon™ film under one of the aluminum skins. Disbonds in the sealant samples were created by applying the sealant partially onto one of the aluminum skins with an ink roller, while leaving strips of bare metal exposed.

Eleven of the 32 lap splice test samples (entries marked with a “yes” in column 9 of Table 2.1) were loaned to the CASR program in February of 1991. There are three details concerning the construction of the adhesive/scrim cloth samples that were unknown at the time the samples were received at ISU: (1) whether a single or double layer of Teflon™ film was used to create the disbond areas; (2) if the adhesive was applied on the aluminum skin next to the Teflon™ film; and (3) if the surfaces of the aluminum skins were prepared for adhesive bonding. Regardless of the unknown details about the adhesive/scrim cloth samples, the samples were our first exposure to a physical aluminum/adhesive lap splice, and their use was greatly appreciated.

Table 2.1: Characteristics of the fuselage lap splice test samples fabricated by Boeing

No.	Top Skin Thickness (mils)	Bottom Skin Thickness (mils)	Bonding Material	Bondline Corrosion	Bondline Water	Disbond Width (inch)	Disbond Location (inch)	Loaned to CASR
1	40	40	Adhesive	-	-	1.0	3.75	-
2	40	40	Adhesive	Yes	Yes	4.0	2.05	Yes
3	40	40	Sealant	-	Yes	4.0	0.56	-
4	40	40	Sealant	Yes	-	1.0	0.76	-
5	40	71	Adhesive	-	Yes	1.0	5.18	-
6	40	71	Adhesive	Yes	-	4.0	1.59	Yes
7	40	71	Sealant	-	-	4.0	0.42	Yes
8	40	71	Sealant	Yes	Yes	1.0	1.10	Yes
9	71	40	Adhesive	-	-	4.0	1.57	-
10	71	40	Adhesive	Yes	Yes	1.0	3.49	Yes
11	71	40	Sealant	-	Yes	1.0	1.05	Yes
12	71	40	Sealant	Yes	-	4.0	2.07	Yes
13	71	71	Adhesive	-	Yes	4.0	0.70	Yes
14	71	71	Adhesive	Yes	-	1.0	1.28	Yes
15	71	71	Sealant	-	-	1.0	3.77	Yes
16	71	71	Sealant	Yes	Yes	4.0	1.33	Yes
17	40	40	Adhesive	-	-	-	-	-
18	40	40	Adhesive	-	-	-	-	-
19	40	40	Sealant	-	-	-	-	-
20	40	40	Sealant	-	-	-	-	-
21	40	71	Adhesive	-	-	-	-	-
22	40	71	Adhesive	-	-	-	-	-
23	40	71	Sealant	-	-	-	-	-
24	40	71	Sealant	-	-	-	-	-
25	71	40	Adhesive	-	-	-	-	-
26	71	40	Adhesive	-	-	-	-	-
27	71	40	Sealant	-	-	-	-	-
28	71	40	Sealant	-	-	-	-	-
29	71	71	Adhesive	-	-	-	-	-
30	71	71	Adhesive	-	-	-	-	-
31	71	71	Sealant	-	-	-	-	-
32	71	71	Sealant	-	-	-	-	-

1. High frequency pulse-echo contact testing

After receiving the Boeing samples, the first ultrasonic test performed on them was a simple one-sided PE contact inspection. A high frequency (20 MHz) transducer, with a delay rod, was placed directly onto the top aluminum skin of the lap splice. The A-scan traces were compared over the bonded and disbanded regions of the lap splice. Figure 2.3 illustrates two

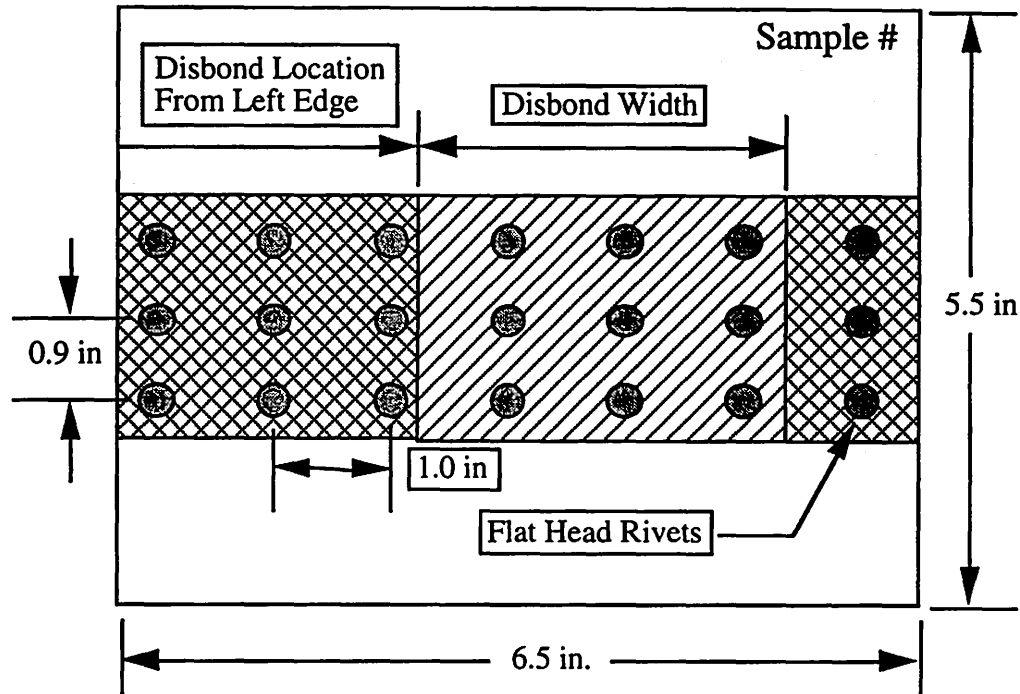


Figure 2.2: Schematic of the Boeing lap splice test samples showing disbond locations.

representative A-scan traces taken over bonded and disbonded areas of an adhesive lap splice. Comparing these two traces, the decay of the signal envelope is the most predominant feature. Measurements taken over bonded regions in an adhesive lap splice are attenuated into the signal noise faster than measurements taken over disbonded regions. At least sixteen “reflection echoes” of the top aluminum skin are seen in the A-scan trace taken over the disbonded region, while only eleven top skin reflection echoes are recognizable in the A-scan trace taken over the bonded region. The reflection echo response can be explained through consideration of acoustic reflections and transmissions. At each interface in a bonded aluminum lap splice a portion of the ultrasonic energy is reflected back toward the transducer, and a portion of the energy is transmitted through. In a disbonded lap splice, where the aluminum skin is separated from its adjoining adhesive layer, all energy is reflected within the top aluminum skin back toward the transducer. This effect is shown in Fig. 2.4. In this figure, the reflection echoes are shown at an angle of incidence to the surface normal only for the purposes of illustrating the interface reflections and transmissions.

From Fig. 2.3 and Fig. 2.4 it can be seen that the reflected echoes taken over a disbonded region have “cleaner” reflection echoes; and by conservation of energy, the reflection echoes

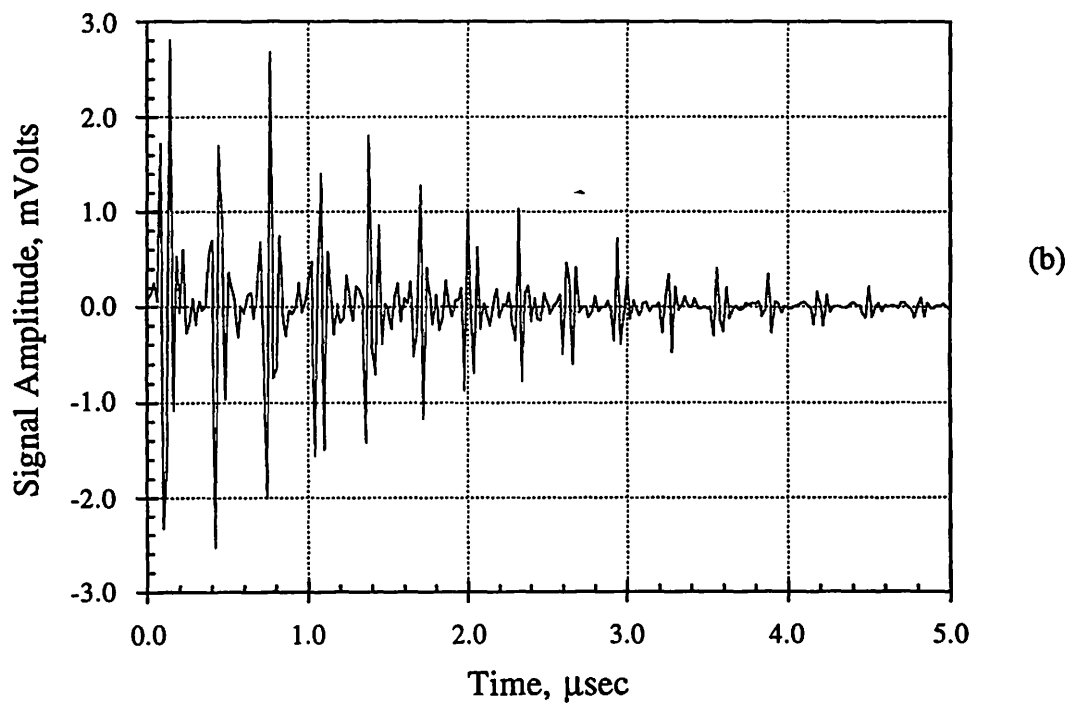
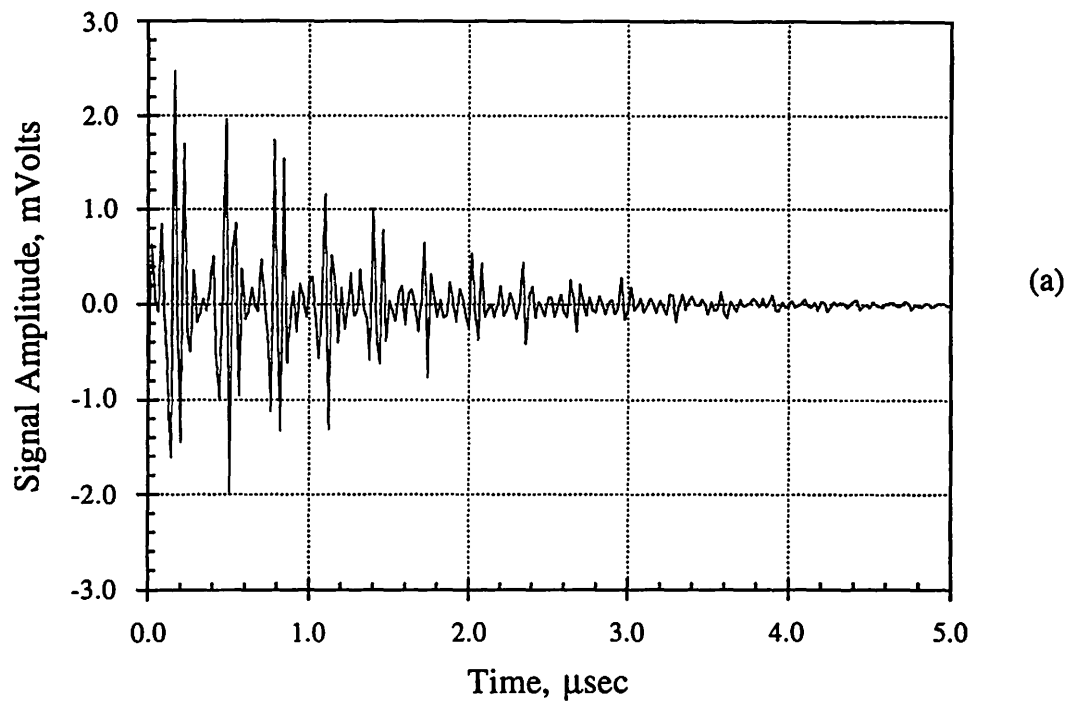


Figure 2.3: 20 MHz A-scan traces taken over (a) bonded and (b) disbonded regions of a lap splice.

will “ring” longer because they do not experience any transmission losses. Using this observation, a method of imaging the disbond region in an adhesive lap splice can be made by time-gating the amplitude of one of its reflection echoes. A natural choice of reflection echo in which to time gate would be the top aluminum skin’s second back surface echo (2BSE). In the adhesive lap splices studied here, both metal skins are made out of Al2024-T3 aluminum with identical velocities, attenuation and comparable thicknesses. Considering the adhesive layer to be very thin, the time for a reflection echo to make one complete trip

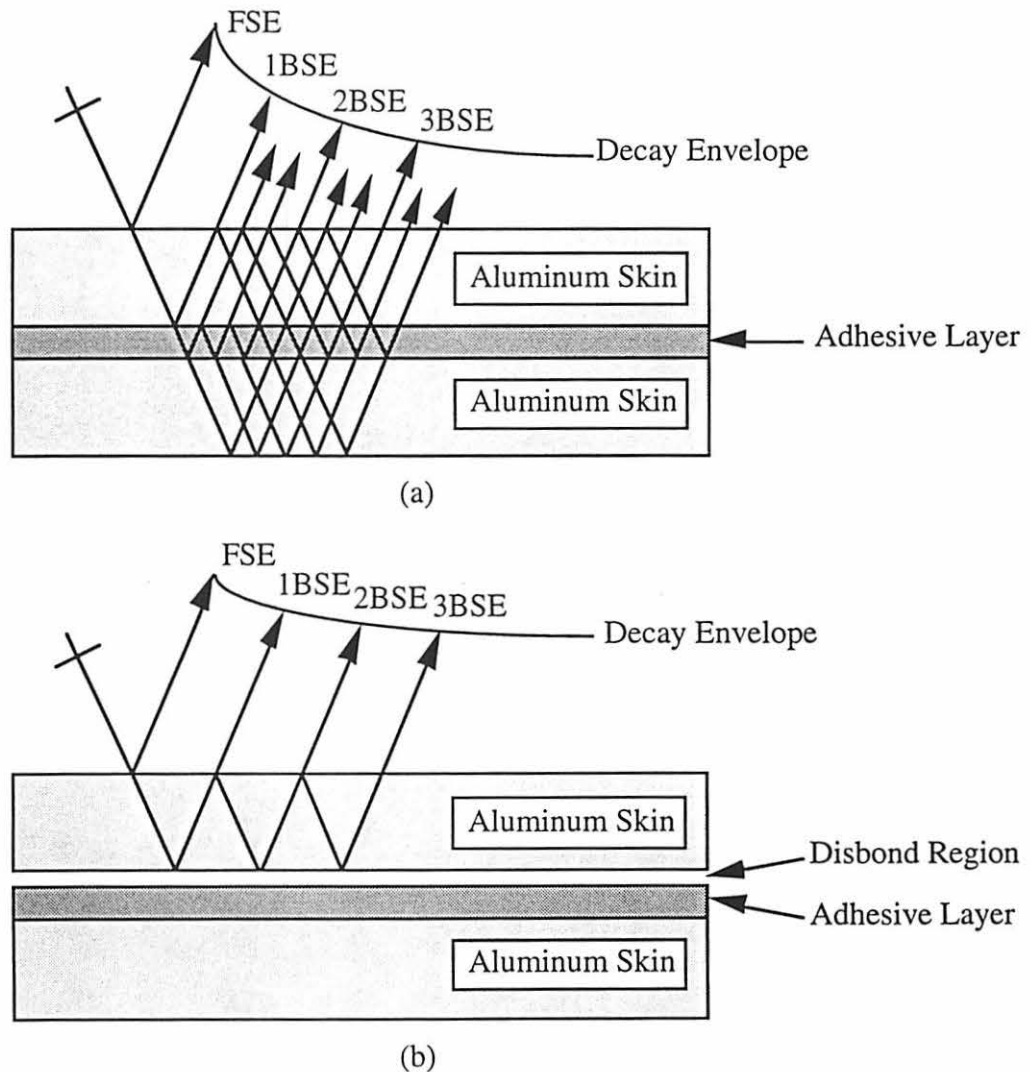


Figure 2.4: Schematic representation of reflection and transmission echoes that exist in (a) bonded and (b) disbonded lap splice.

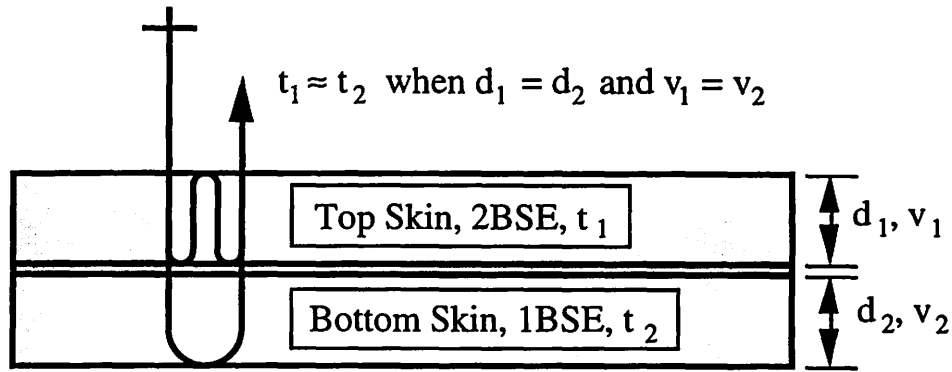
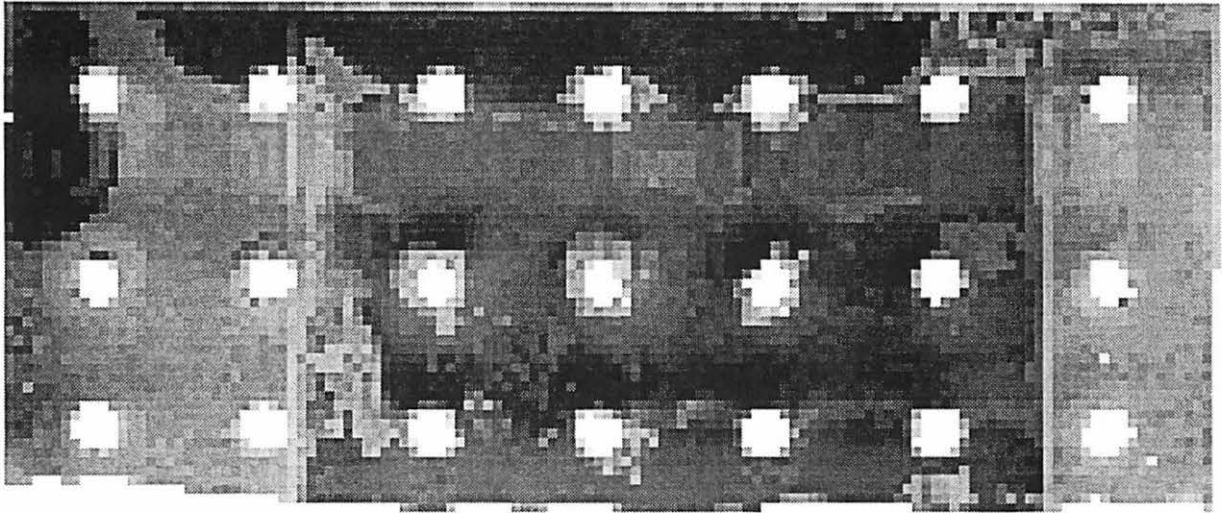


Figure 2.5: RF interference caused by two reflection echoes in a lap splice arriving at approximately the same time.

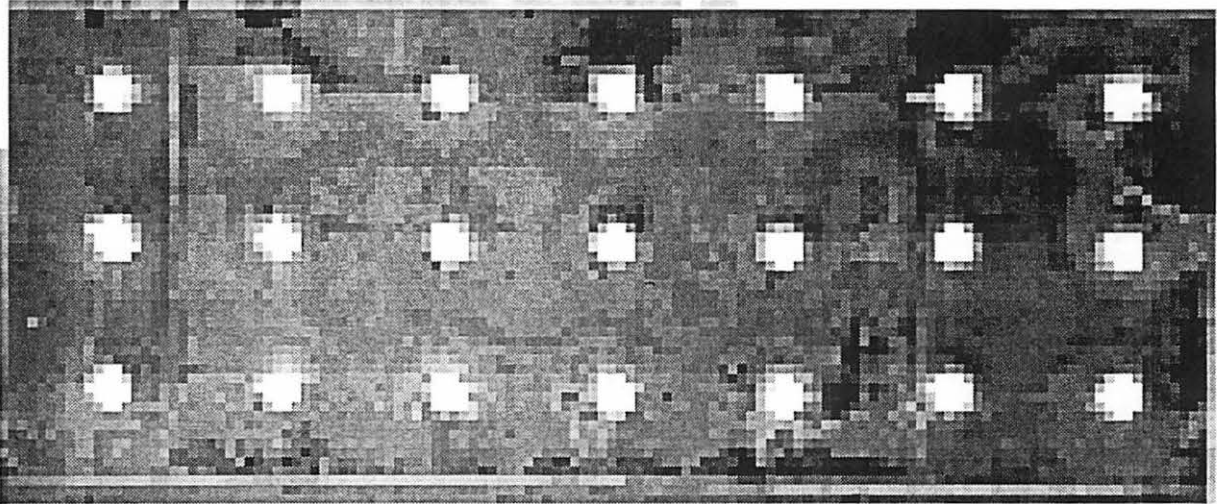
through the lap splice is approximately the same time as two complete trips in the top aluminum skin as shown in Fig. 2.5. Since the reflection echoes are arriving at nearly the same time, but from different paths in the lap splice, constructive and destructive interference may exist in the resulting RF signal. Other back surface echoes can be time-gated to produce a C-scan image of the adhesive lap splice.

2. High frequency immersion testing

Using the results of the PE contact inspection on the Boeing lap splice samples, an experiment was designed (much like Ref. 34, without the digital signal processing) to produce C-scan images of the disbond regions. The sample was placed in an immersion tank and a 15 MHz, 0.5 in (1.27 cm) diameter, 3.0 in (7.62 cm) spherical focal length (in water) transducer, was focused onto the surface of the lap splice's top aluminum skin. Depending on the individual sample, the amplitude of the second or third top skin reflection echo was time-gated to produce the C-scan image. The choice of BSE reflection echo was dictated by the sample's signal-to-noise ratio and chosen arbitrarily. Four representative C-scan images (the front and back side of an adhesively bonded and a sealant bonded samples respectively) are shown in Figs. 2.6 and 2.7 respectively. The back side images are flipped horizontally with respect to the front side images. In regions of disbond a greater portion of the ultrasonic energy is reflected back toward the transducer, compared to bonded areas where some of the energy is coupled through. This manifests itself on the images as darker regions that correspond to high signal amplitudes occurring in the time gate. In these images the disbond is clearly seen from all front side scans. In samples containing adhesive and scrim cloth in the



(a)



(b)

Figure 2.6: High frequency (15 MHz) scan images of the (a) front side and the (b) back side of an adhesive lap splice. Images made using the amplitude of the 2BSE in the top aluminum skin. White circles are rivets. The disbonds are shown as dark colored regions. Scan area: 6.5 x 3.5 in (16.5 x 8.9 cm); step size: 20 mils (0.5 mm).

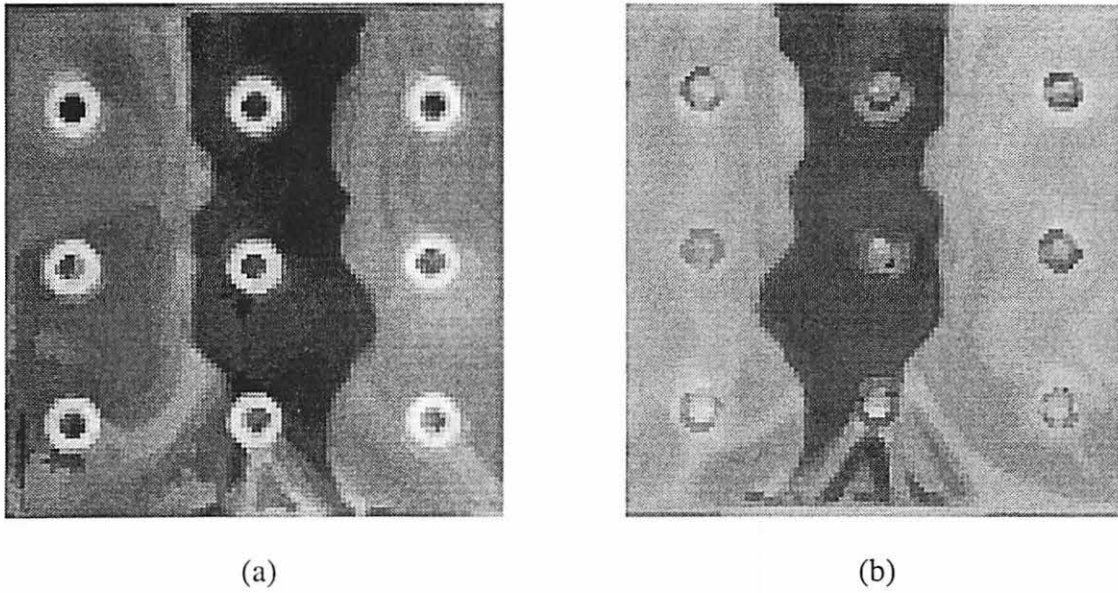


Figure 2.7: High frequency (15 MHz) scan images of the (a) front side and the (b) back side of a sealant bonded lap splic. Images made using the amplitude of the 2BSE in the top aluminum skin. White circles are rivets. The disbonds are shown as dark colored regions. Scan area: 2.5 x 3.5 in (6.4 x 8.9 cm); step size: 10 mils (0.25 mm).

bondline, scans made from the back side do not readily indicate the presence of a disbond. Scans made from the back side indicate that the amount of ultrasonic energy reflected back over the disbond and bonded regions are nearly the same. This would suggest that the disbond (Teflon™ insert) is located next to the top aluminum skin layer. The most obvious feature visible in the back side scans of the adhesive lap splices is the edge location of the Teflon™ inserts. At the edge of the inserts, the ultrasonic beam is scattered away from the normal, producing a lower signal amplitude than the surrounding area. Disbonds created using Teflon™ tend to provide sharply defined straight edge lines on the images. When the sealant samples were fabricated, a portion of the sealant was left out of the bondline and upon assembly it crept into the disbond area, resulting in disbond edges that are not well defined. In the sealant samples the images taken from the front and back sides are nearly mirror images of each other. The overall color of Figure 2.7b is lighter than Fig. 2.7a because the bottom aluminum skin is thicker than the top aluminum skin.

The nonuniformity of the adhesive thickness is seen in the images as fringe patterns. This is particularly noticeable around the rivet locations. At first it was believed that the patterns were the result of minor surface curvature caused by the rivet installation; however

an image made from a disbond calibration standard sample did not reveal the same type of fringe patterns. Another explanation is the possibility of interfering echoes arriving at the transducer face. Reference [40] showed that the fringe patterns are analogous to the interference patterns called Newton's Rings typically seen in optics. The interference effect is useful if the purpose is to measure the adhesive bondline uniformity; however they may interfere with the detection of other lap splice defects such as corrosion.

A glass lap splice sample was fabricated to provide a transparent visual model of an adhesive lap splice. The sample was made out of a 0.125 in (3.18 mm) thick plate glass with overlap dimensions of 4.0 x 4.0 in (10.2 x 10.2 cm). The sample contained adhesive and scrim cloth in the bondline at same thickness as the lap splice samples provided by Boeing. Strips of Teflon™ tape were placed in the bondline to establish how the Teflon™ disbonds were created in the Boeing adhesive lap splice samples. Disbonds using Teflon™ in lap splices are made by placing two strips of Teflon™ tape together in the bondline, while one strip of Teflon™ tape alone in the bondline typically represents an inclusion. The Teflon™ inserts were placed in three rows in the sample as shown in Fig. 2.8. In this figure, the top row contained two strips of Teflon™ tape placed together, the middle row contained one strip of Teflon™ tape with a thin layer of adhesive applied on top of the tape, and the bottom row contained a single strip of Teflon™ tape only. All the Teflon™ inserts placed in the glass lap splice sample are located above the adhesive/scrim cloth layer.

Pulse-echo C-scan images made using the PP amplitude of the 2BSE on the glass lap splice are shown in Fig. 2.9. The scan made from the front side of the glass sample (the side illustrated in Fig. 2.8) is shown on the left. The back side image is horizontally opposed to the front side image. The scan from the front side of the glass sample does not readily indicate the difference between a single or double Teflon™ layer; but the middle row, with the thin layer of adhesive on top of the Teflon™ tape, is seen as a lighter color compared to the other two rows. The lighter color over the middle row is related to a decrease in signal amplitude found over the thin adhesive layer. A scan made from the back side of the glass sample reveals the double Teflon™ layer through the adhesive/scrim cloth layer, while the other two single Teflon™ layers are seen as similar. The color assignments in the images corresponding to Teflon™ insert placement can be explained by considering the material adjacent to the aluminum layers in the lap splice. From the front side scan, the adhesive layer placed over the Teflon™ insert couples a portion of the ultrasonic energy into the sample decreasing the signal amplitude slightly, whereas over the other two rows, with their

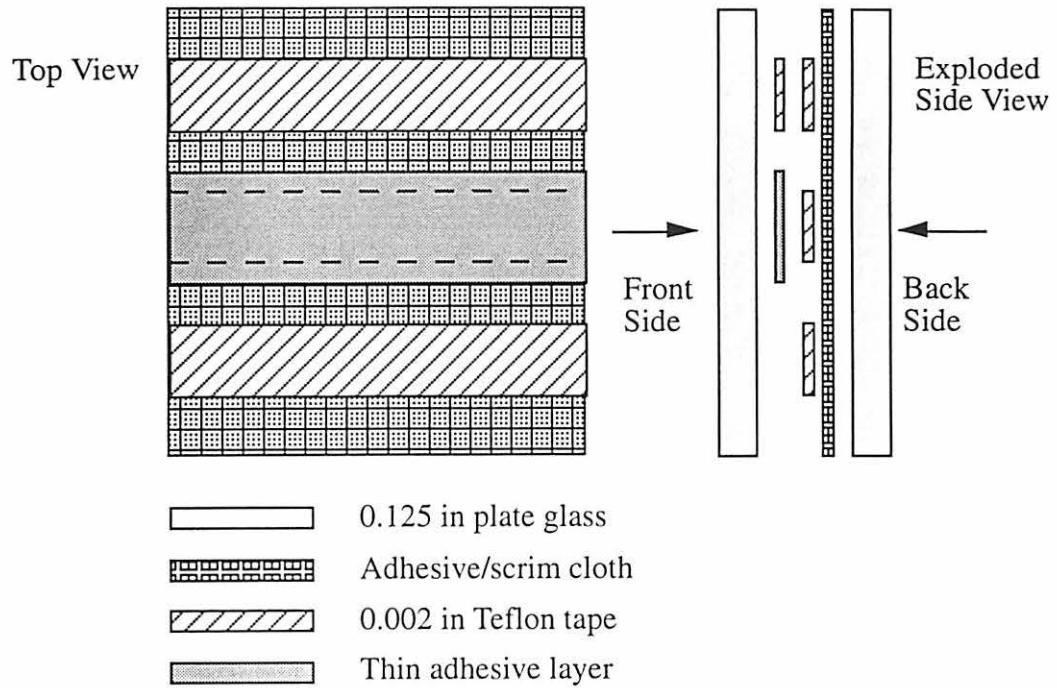


Figure 2.8: Schematic example of glass/adhesive bond sample with Teflon™ inserts placed on top of the adhesive/scrim cloth layer.

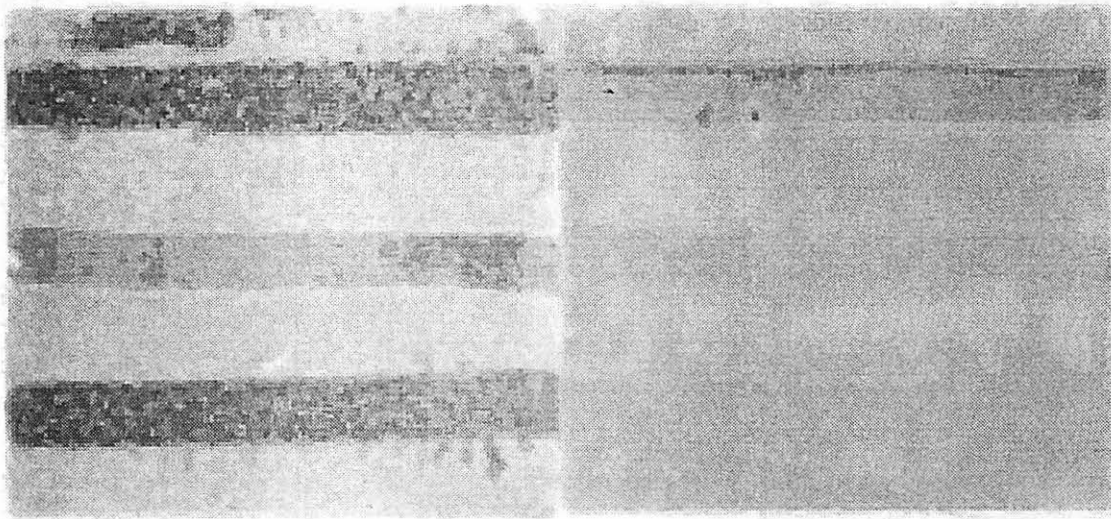


Figure 2.9: Pulse-echo C-scan images made using the PP amplitude of a 15 MHz 2BSE. The scan made from the front side of the glass sample (the side illustrated in Fig. 2.8) is shown on the left. Scan area: 8.0 x 4.0 in (20.3 x 10.2 cm); step size: 10 mils (0.25 mm).

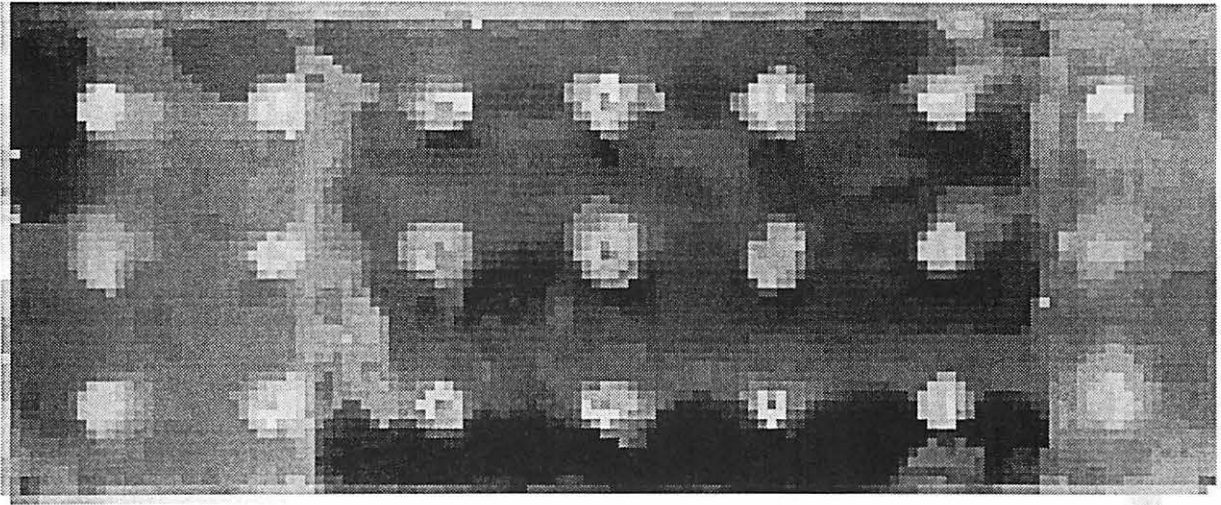
back side air condition, all energy is reflected back toward the transducer. Through the adhesive/scrium layer, from the back side, the signal amplitude is decreased and the contrast between bonded and disbonded areas is decreased. Also of interest are areas where the adhesive did not fully wet the glass plate and air pockets formed. These are shown as dark colored areas not associated with the Teflon™ inserts.

3. Squirter testing

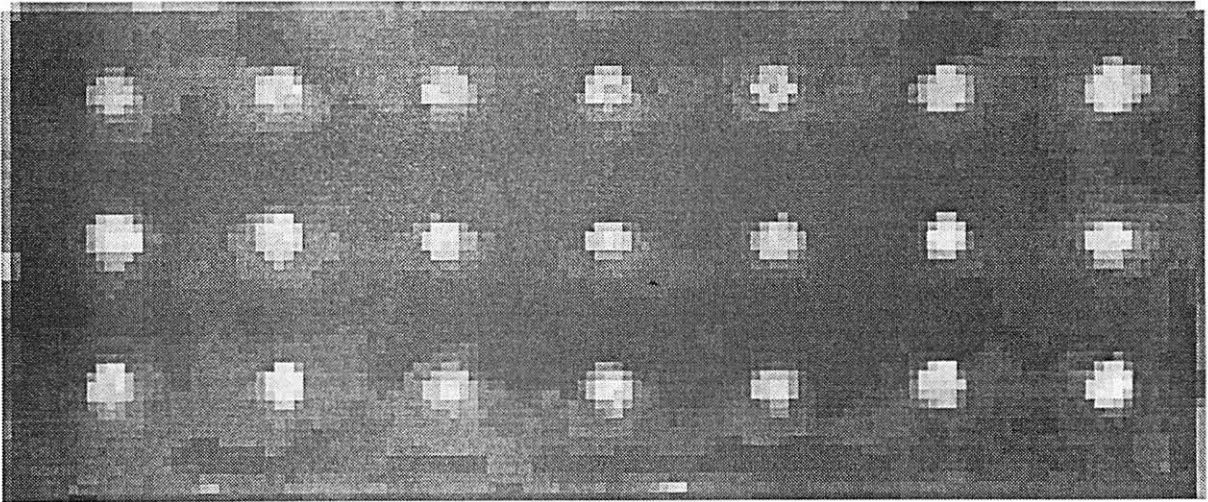
Ultrasonic water squirters are normally reserved for TTU inspections; however, PE squirter inspections are possible. A “squirter” inspection uses an immersion transducer enclosed in a water jacket housing with the focal point of the transducer positioned at the housing outlet. The ultrasonic energy is collimated onto the sample’s surface trapped within the outlet water column. The squirter available at ISU was oriented vertically and operated at a very low flow rate to avoid turbulent water flow. Two of the Boeing samples, tested using high frequency PE immersion, were rescanned in a PE squirter mode for comparison. The same transducer was used for the comparison; and the gain settings on the pulser/receiver were adjusted to compensate for the signal loss that occurs as the sound beam is collimated and reflected from the nozzle. The RF signals are not as “clean” as those taken in immersion, but the top skin reflection echoes are still observable. The results of the squirter inspections on adhesive and sealant bonded lap splices are shown in Figs. 2.10 and 2.11 respectively. There is a difference in image quality between immersion and water squirter scans; however, each method provides the same information regarding the existence of disbonds in the lap splices. With a water squirter, near immersion quality C-scan images can be made out of the immersion tank. The airline industry does not routinely use squirters to inspect fuselage lap splices because of the uncontained water problem associated with a water squirter inspection. When squirters are used they are often used on parts removed from the aircraft.

4. Low frequency immersion testing

One Boeing adhesive lap splice was scanned in PE using a low frequency 1 MHz, 1.0 in (2.54 cm) diameter, 2.0 in (5.08 cm) focal length (in water) broadband transducer. Low frequency, in the context of this thesis, refers to center frequencies whose wavelengths are greater than the lap splice layer thicknesses. This is not to be confused with “sonic” techniques that typically operate in the KHz range. In the aluminum/adhesive lap splices studied here, the wavelength of a 1 MHz pulse (in aluminum) is 3 times larger than the entire thick-



(a)



(b)

Figure 2.10: High frequency (15 MHz) water squirter scan images of the (a) front side and the (b) back side of an adhesive lap splice. Images made using the amplitude of the 2BSE in the top aluminum skin. Figure 2.10a is reproduced from Fig. 2.6a. Scan area: 6.5 x 3.5 in (16.5 x 8.9 cm); step size: 20 mils (0.5 mm).

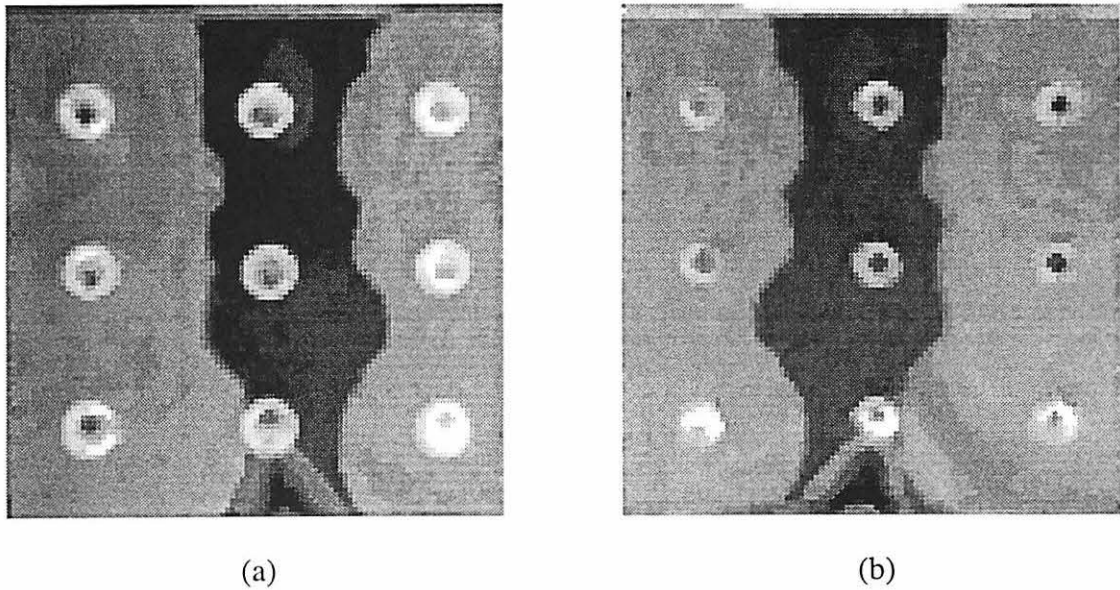


Figure 2.11: High frequency (15 MHz) water squirter scan images of the (a) front side and the (b) back side of a sealant bonded lap splice. Images made using the amplitude of the 2BSE in the top aluminum skin. Figure 2.11a is reproduced from Fig. 2.7a. Scan area: 2.5 x 3.5 in (6.4 x 8.9 cm); step size: 10 mils (0.25 mm).

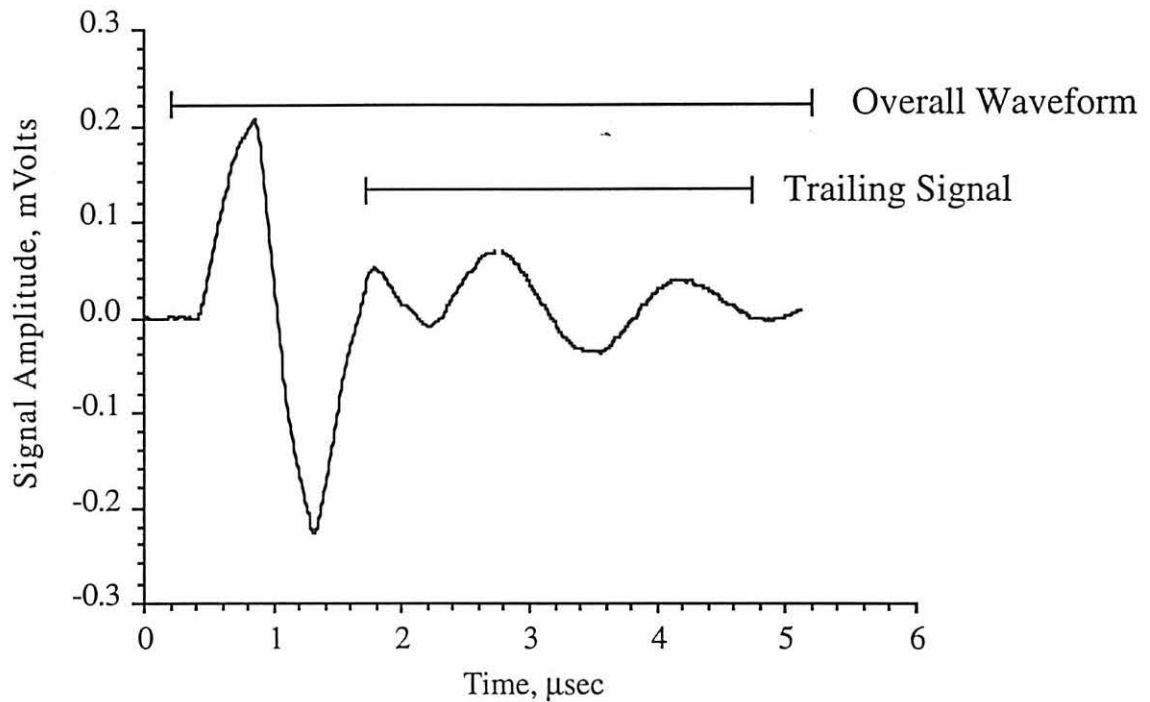


Figure 2.12: Low frequency (1 MHz) pulse-echo RF waveform and time gate positions from an adhesively bonded lap-splice assembly.

ness of the lap splice. The resulting waveform, shown in Fig. 2.12 contains unresolved interface echoes, and is a function of frequency, layer thickness and material properties. Also shown in Fig. 2.12 are the two time gate locations used throughout the remainder of this thesis. The “Overall Signal” time gate represents a period of time that captures the overall amplitude of the reflected RF signal. The “Trailing Signal” corresponds to a time gate that starts after the tri-polar pulse and extends in time far enough to capture any relevant trailing signals. Trailing signal images are made with an increased pulser/receiver gain for a larger dynamic range of image color assignments. The overall amplitude images are made in the usual manner.

As shown earlier (Fig. 2.6b), the image made from the back side of an adhesive lap splice with a 15 MHz pulse did not readily illustrate the presence of a disbond. What was identifiable was the disbond edges where the ultrasonic energy was scattered away from the transducer, producing light color strips. Using a low frequency pulse, the disbond area is easily seen from the back side (with the aid of image contrast enhancements) as shown in Fig. 2.13. Absent from the images are the interference patterns that were seen when scanned with the high frequency transducer. The technique provides a means for designing a technique that gives a yes/no answer when inspecting bonded lap splice samples.

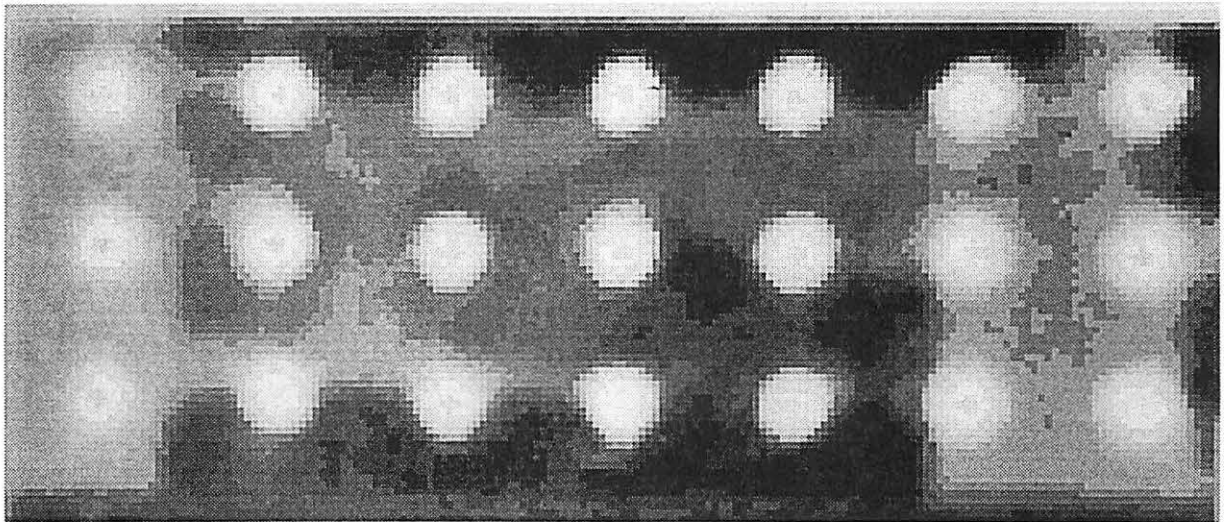


Figure 2.13: Low frequency (1 MHz) scan image of the back side of an adhesively bonded lap splice. Disbond is located behind the adhesive/scrim cloth layer. Scan area: 6.5 x 3.5 in (16.5 x 8.9 cm); step size: 20 mils (0.5 mm).

CHAPTER III. THE LOW FREQUENCY INSPECTION TECHNIQUE

A. Introduction

Traditionally, ultrasonic NDI of thin structures such as a fuselage lap splice, has been oriented toward high frequency inspections with resolved echoes within the layers. There are a number of disadvantages associated with a high frequency inspection: high attenuation of the RF signal, shallow integration depth, and RF signal interference. Additionally, a high frequency C-scan inspection requires time gates to separate the individual interface reflections. A low frequency inspection, on the other hand, provides deep penetration into the layered structure and does not suffer from complicated RF waveforms. A low frequency C-scan inspection isn't without its disadvantages. Because the unresolved echo represents small changes in the layered structure as a whole, the contrast between image areas is very low. A focused ultrasonic beam is used to improve the spatial resolution and image enhancements are used to improve the image contrast.

This chapter describes the low frequency inspection technique and its application toward inspecting fuselage lap splices. Comparisons between the low frequency inspection technique and high frequency inspections are made using comparable C-scan images. The technique is used to detect lap splice disbonds located above and below the adhesive/scrim cloth layer. Abedin et al [40] reported that for detection of disbond in aluminum/adhesive lap splice, their best results were obtained at centerband frequencies operating close to the resonance condition in the top aluminum skin. In this research, ultrasonic frequencies even lower than top skin resonance are used to extend the NDI of lap splices past just detecting disbonds to include detection of second layer corrosion as well. The parameters associated with the technique are investigated using C-scan images as a guide. The response of the low frequency pulse as reflected from layered structure is modeled to provide insight into inspection capability of the technique.

B. The Technique

The low frequency inspection technique exploits the advantages of a visual image. Ultrasonic C-scan images are widely used by aircraft manufactures for the detection of manufacturing flaws, but are not routinely used by air carriers as a maintenance tool. A C-scan image allows an inspector to "see" subtle changes in the character of the lap splice that would otherwise go unnoticed using an A-scan inspection. A C-scan assigns a color scale to the

subtle changes, and with the use of simple image enhancements, the small changes are easily seen.

The low frequency inspection technique is quite simple. An image is made of the overall amplitude of an unresolved, focused-beam, broadband pulse over the lap splice surface. With the technique, time gates can be eliminated to provide a considerable speed advantage during the scan process [42]. Even though the technique primarily uses the overall amplitude of the RF signal, the trailing portion of the RF signal can be used to obtain information about the second layer of the lap splice. The trailing signal portion of the reflected RF waveform, though unresolved, does contain information about the character of the lap splice. The technique is relatively insensitive to minor surface curvature because the focal zone of the transducer is relatively long, and the precise location of the focal spot is not critical. The technique lends itself to rapid scanning of structures. It is easily implemented, uses the power of a visual image, does not require sophisticated software, or critical alignment of the transducer.

C. Realistic Aluminum/Adhesive Lap Splice Samples

In the past, very little adhesive bond research has been conducted using truly representative fuselage lap splice samples. Given that the problem of bond strength assessment using NDI techniques has not been solved, it is not surprising that past researchers have directed their attention toward very simple adhered/adhesive lap splice samples. It is assumed that by simplifying the lap splice some of the unknown parameters affecting adhesive bond strength can be eliminated, or at least, kept to a minimum. It is common practice to simplify and scale-down experiments in the laboratory for the purposes of minimizing experimental unknowns. If the unknown parameters can be isolated through a systematic study, their influence on the whole can be determined. Dangers occur when the simplified analysis and/or experiments only work in a laboratory environment and can not be applied in a realistic situation. This research is tasked with developing an ultrasonic inspection technique that can be used directly on an aircraft to inspect fuselage lap splices [43]. To achieve the task objectives, realistic samples must be inspected in a realistic environment. It was the intention of this research to concentrate on realistic lap splice samples; however, realistic lap splice samples are not easily obtainable.

The difficulty in obtaining realistic samples is best illustrated with lap splices containing

corrosion defects. Current maintenance procedures make it difficult for researchers to obtain lap splice corrosion samples from serviceable aircraft. The detection of corrosion in lap splice assemblies has been given an important inspection priority by the airline industry, and regular inspection procedures have been developed to meet these new requirements. During maintenance, if corrosion is suspected in a lap splice area, the area is opened up for further inspection by removing the rivets, adhesive and sometimes the paint. If the corrosion damage is beyond the manufacturer's tolerances, the corroded area is cut out and patch-repaired; otherwise, the corrosion is removed by chemical or mechanical means, leaving a serviceable but thinner metal skin when the joint is reassembled [12]. In either case, the original character of the lap splice has been destroyed by the maintenance process, and its use for NDI purposes is lost. In this light, it becomes necessary for researchers to fabricate their own laboratory samples and compare these artificial samples with actual in-service samples.

The aluminum/adhesive lap splice samples fabricated for this research are representative of the Boeing 510 adhesive lap splice found on early model Boeing 727 and 737. These lap splice samples have 40 mil (1.02 mm) thick aluminum skins (Al2024-T3) with a 5.0-8.0 mil (0.13-0.20 mm) thick bondline that contains a composite cold-bond adhesive and scrim cloth mixture. Within the capability and confines of a laboratory environment, all the lap splice samples were prepared, fabricated and cured using the procedures established by a Boeing standard operating procedure (SOP), or an American Society of Testing and Materials (ASTM) standard. There are some noticeable differences between the SOPs and the ASTM standards concerning process time, temperature, and chemical concentration. Whenever possible the chemical manufacturers' instructions were used; and ASTM standards were used instead of the SOPs [44,45].

D. Fatigue-Induced Disbond Detection

This phase of the research was coordinated through cooperation with the Mechanical Engineering Department at Tuskegee University (TU) in Alabama. The lap splice samples were fabricated at ISU using the procedures found in Ref. 46. After the samples cured fully, an ultrasonic baseline reference was established to determine if any pre-fatigue defects were present in the bondline. On the basis of the initial scans, several samples were sent to TU to have artificial disbonds created in them through flexural mechanical fatigue test. Details of the mechanical fatigue process can be found in Ref. 47. The cleavage-style fatigue process separates the adhesive from the adherend and allows a correlation between the surface area of

the disbond and the number of fatigue cycles. Apart from slight bondline thickness variations, the samples contain a disbond condition as their only defect. It should be noted that the disbond created in the laboratory lap splices may not be representative of a disbond that occurs in an actual aircraft fuselage lap splice section.

After the samples were fatigued they were sent back to ISU for post-fatigue ultrasonic inspection. The lap samples were ultrasonically scanned in an immersion tank from both sides using low (1 MHz) and high frequency (15 MHz) focused-beam, broadband, immersion transducers. Before the samples were immersed, the edges of the samples were sealed to prevent water from entering the disbond area during the inspection. The results of the C-scan inspection from one of the lap splice samples are shown in Fig. 3.1. The C-scan images shown on the left, (a) and (c), were scanned using the low frequency inspection technique, while the high frequency C-scan images, scanned using the amplitude of the 2BSE in the top aluminum skin, are shown on the right, (b) and (d). Images made from the “front side” of the lap splice are shown on the top row while the “back side” images are shown on the bottom row. The back side images are shown flipped vertically with respect to the top side images. The disbond area in each image is located on the left 1/3 of the images.

The location of the disbond in this sample is schematically shown in Fig. 3.2. The top figure illustrates that the adhesive/scrim cloth layer is separated from the top aluminum skin, corresponding to the images shown in the top row of Fig. 3.1. Likewise, the bottom figure in Fig. 3.2 correspond to the scans shown in the bottom row of Fig. 3.1.

C-scan images made with the low frequency inspection technique are much “cleaner” than those made using a higher frequency inspection. Much as “sonic” methods, the low frequency inspection technique samples the mechanical response of the lap splice as a whole; and bond and disbond areas influence the amplitude of the unresolved reflected echoes differently. As shown in Fig. 3.1, images made with the low frequency inspection technique leave little doubt that a disbond exists in the lap splice; however depth information concerning the location of the disbond above or below the adhesive/scrim cloth layer is lost. Disbond depth information, if needed, should be obtained using a higher frequency ultrasonic inspection or another NDI technique. However, because of the complex image patterns (seen earlier in the Boeing lap splice samples — Chapter 2) a higher frequency inspection may have difficulty detecting whether a disbond condition exists below the scrim cloth layer.

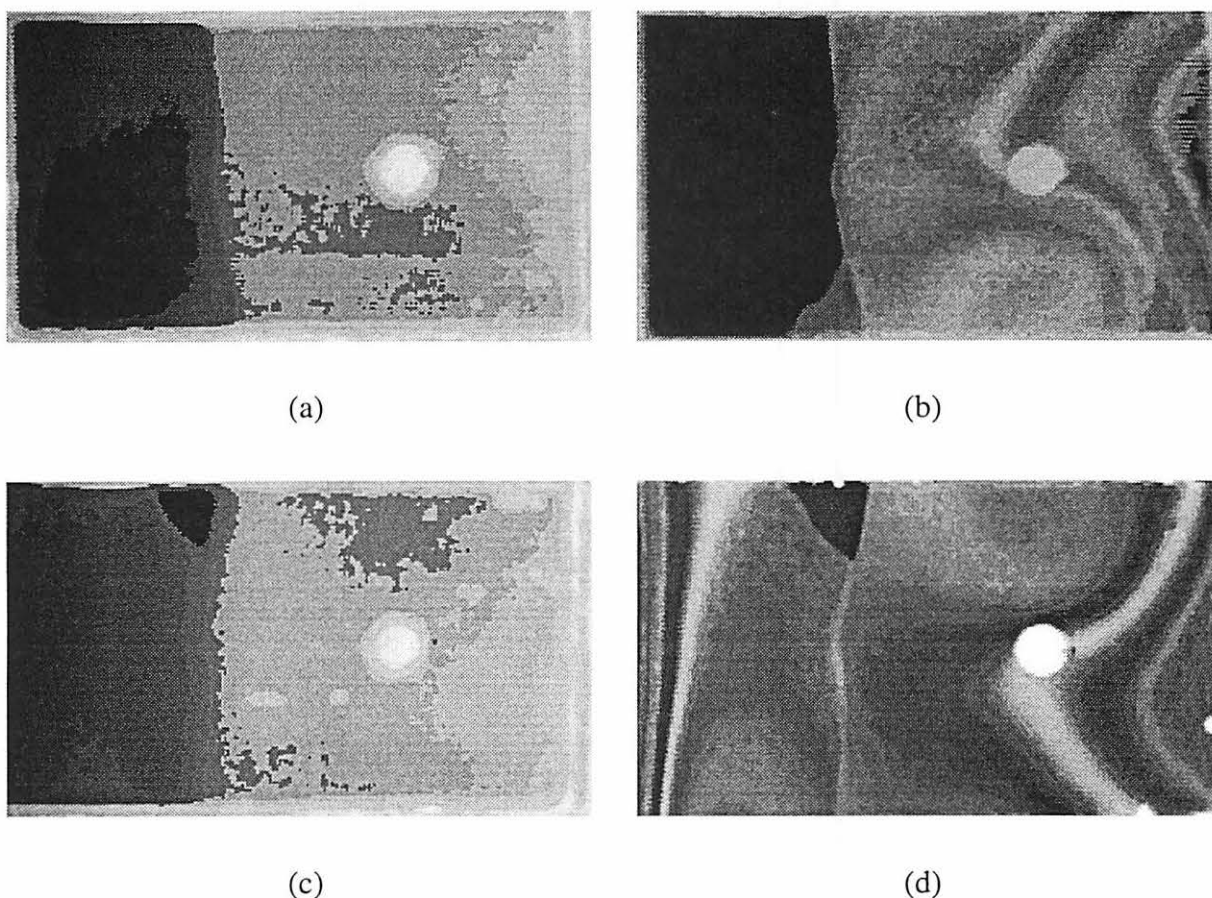


Figure 3.1: Low and high frequency C-scan images of a disbond in an aluminum/adhesive lap splice. (a) Scan of the front side with a 1 MHz transducer. (b) Scan of the front side with a 15 MHz transducer. (c) Scan of the back side with a 1 MHz transducer. (d) Scan of the back side with a 15 MHz transducer. Scan area: 5.0 in x 3.0 in (12.7 x 7.62 cm); scan step size: 10 mils (0.25 mm).

E. Corrosion Detection

Corrosion can exist in either layer of a simple aluminum/adhesive lap splice. For lap splices where only one aluminum surface is accessible, first layer corrosion refers to corrosion that occurs on or under the accessible skin; and second layer corrosion is that which exists behind the adhesive/scrim layer on the upper or lower surface of the inaccessible skin. Detecting and characterizing corrosion that occurs in an aluminum/adhesive lap splice is more difficult than detecting a disbond condition within the lap splice. First layer corrosion is relatively easy to detect and can be characterized using eddy current methods [48]. De-

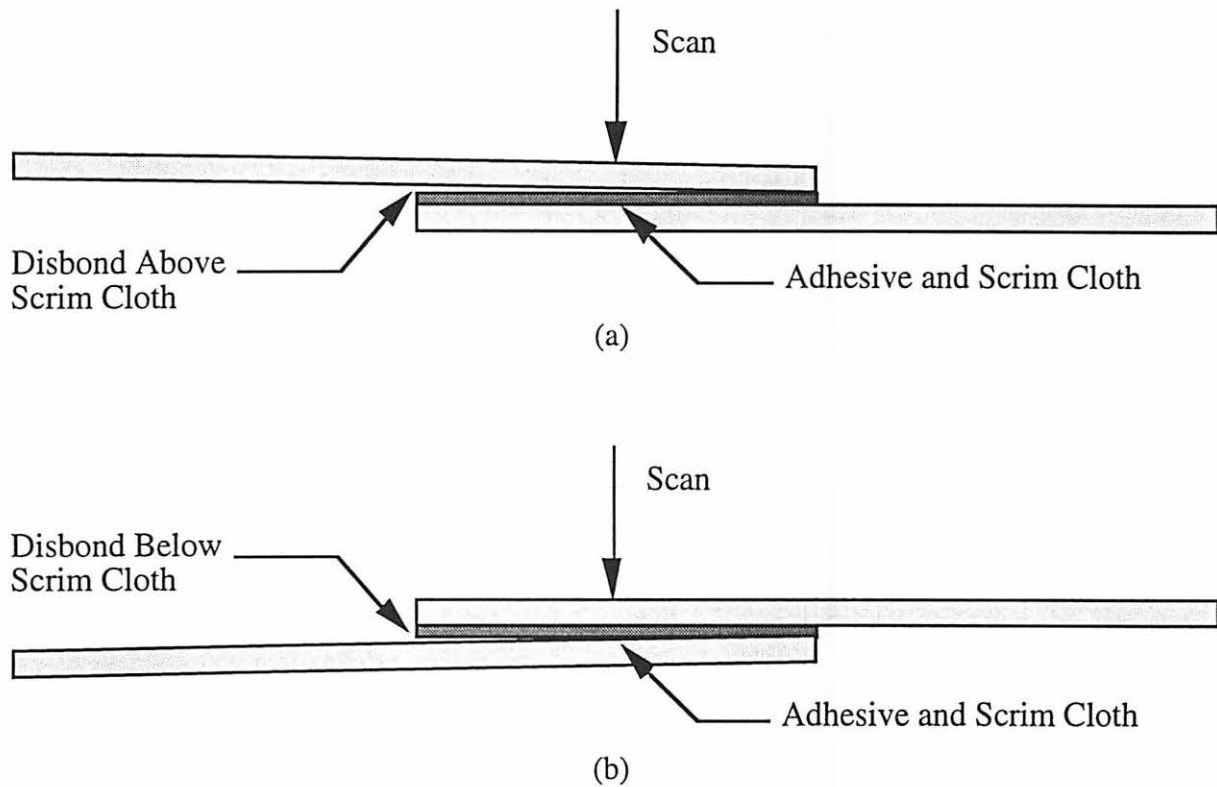


Figure 3.2: Schematic example of a disbond located (a) above and (b) below the adhesive/scrim cloth layer.

fects such as corrosion located under a disbond are very difficult to detect using pulse-echo ultrasonic inspection. A disbond condition “shadows” any lower subsequent lap splice defects. However, the hidden corrosion can be detected under a disbond if there is contact between the adhesive layer and the bottom aluminum skin. The contacts, called asperities, are anything that will allow ultrasonic energy to pass through the disbond, such as corrosion products or trapped water.

1. Uniformly thinned corrosion samples

At the start of this phase of the research, no completely assembled, corroded lap splice samples were available for use. It was necessary then to artificially corroded the lap splice samples in the laboratory and validate the corrosion process against single sheets of corroded aluminum skins taken from actual in-service aircraft.

The aluminum skins were artificially corroded in the laboratory by using them as an electrode in a constant potential electrochemical cell [49]. The electrochemical cell was created by immersing parallel sheets of 3 mil (0.076 mm) platinum and 40 mil (1.02 mm) aluminum in a 0.5 M sodium chloride electrolyte solution while a constant voltage was maintained between them as seen in Fig. 3.3. Shown in Fig. 3.4 are several surface profiles corroded in the laboratory, along with a naturally corroded surface profile taken from a Boeing 727 sample [50]. These surface profiles were obtained from digitized, edge-on-view micrographs of the corroded aluminum skins. In this figure the vertical axis is expanded 10x the horizontal axis to show detail. The surface profile characteristics of Fig. 3.4 are listed in Table 3.1.

Consistency between samples corroded for uniform metal thinning was monitored using mean thickness reduction, deepest pit formation, and mean weight loss, versus corrosion reaction time. These results are shown in Fig. 3.5, with the error bars representing one standard deviation about a mean of six samples. In Fig. 3.5 the mean weight ratio decreases monotonically with corrosion reaction time and shows no indication of sensitivity to cladding removal; however the cladding layer does influence the mean thickness reduction and deepest pit formation.

The RMS roughness (one standard deviation about the mean) versus mean thickness loss, shown in Fig. 3.6, was obtained from the data in Fig. 3.4. As seen in these figures, the RMS roughness of the laboratory samples remains fairly constant until the protective cladding layer is lost to corrosion. At this point, the exposed surface facing the platinum electrode is no longer pure aluminum, but an alloy, which greatly accelerates the corrosion reaction and dramatically increases the corresponding RMS roughness with mean thickness loss. In Fig. 3.6 the x and y error bars for the Boeing 727 skin sample corresponds to measurements made at several locations on the provided sample. The comparisons of RMS roughness versus mean thickness loss between naturally occurring and artificially corroded surfaces and the surface profile plots demonstrate that a corroded surface produced in the laboratory can be representative of naturally occurring corrosion.

After the surfaces of the corroded aluminum skins were characterized with mean thickness and RMS roughness, they were fabricated into aluminum/adhesive lap splices. Shown schematically in Fig. 3.7 are two examples of second layer corrosion that can exist in an adhesive lap splice assembly. It can be seen in this figure that, by flipping the samples up-

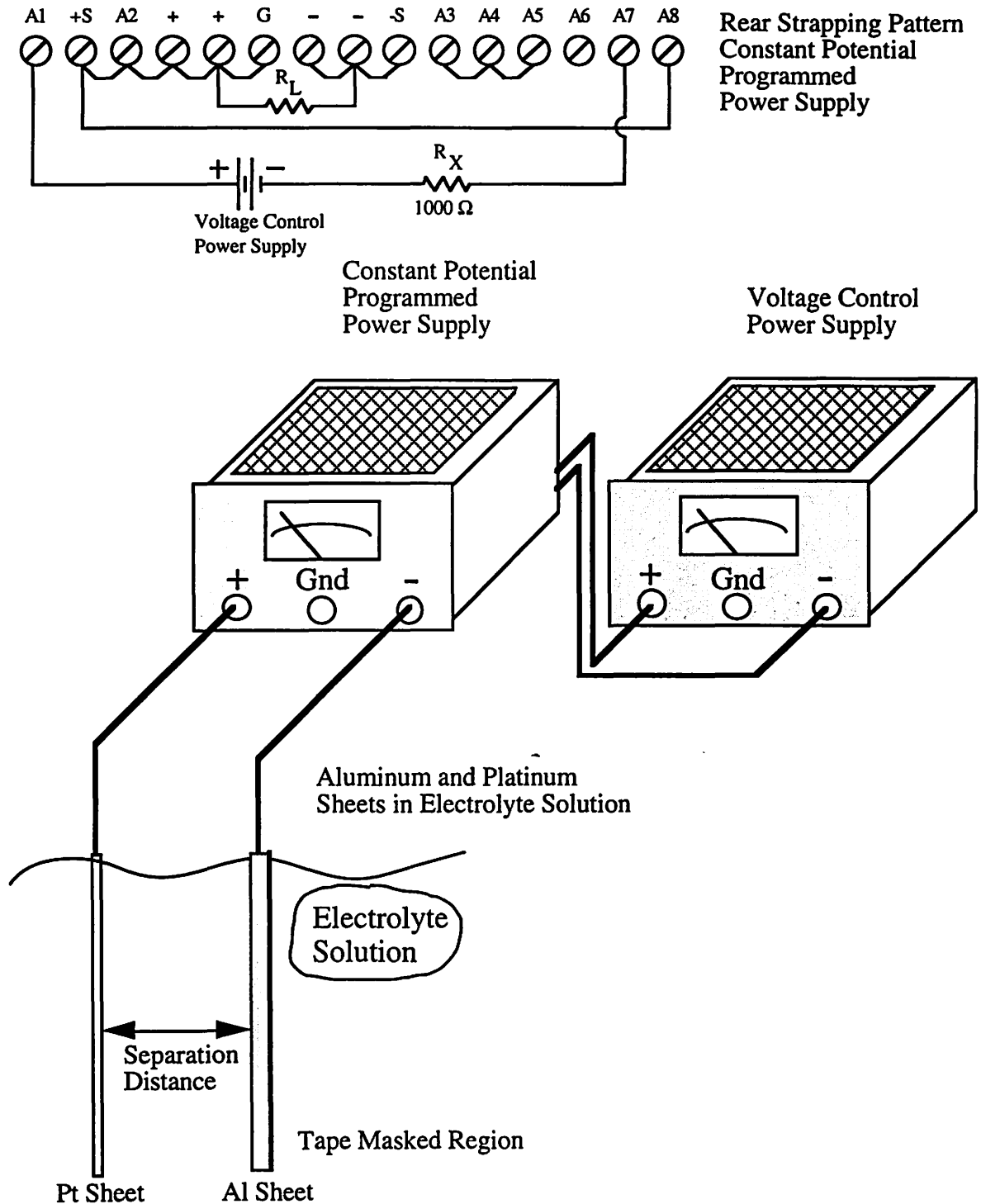


Figure 3.3: Experimental setup — Electrochemical corrosion process configured for uniform metal thinning corrosion.

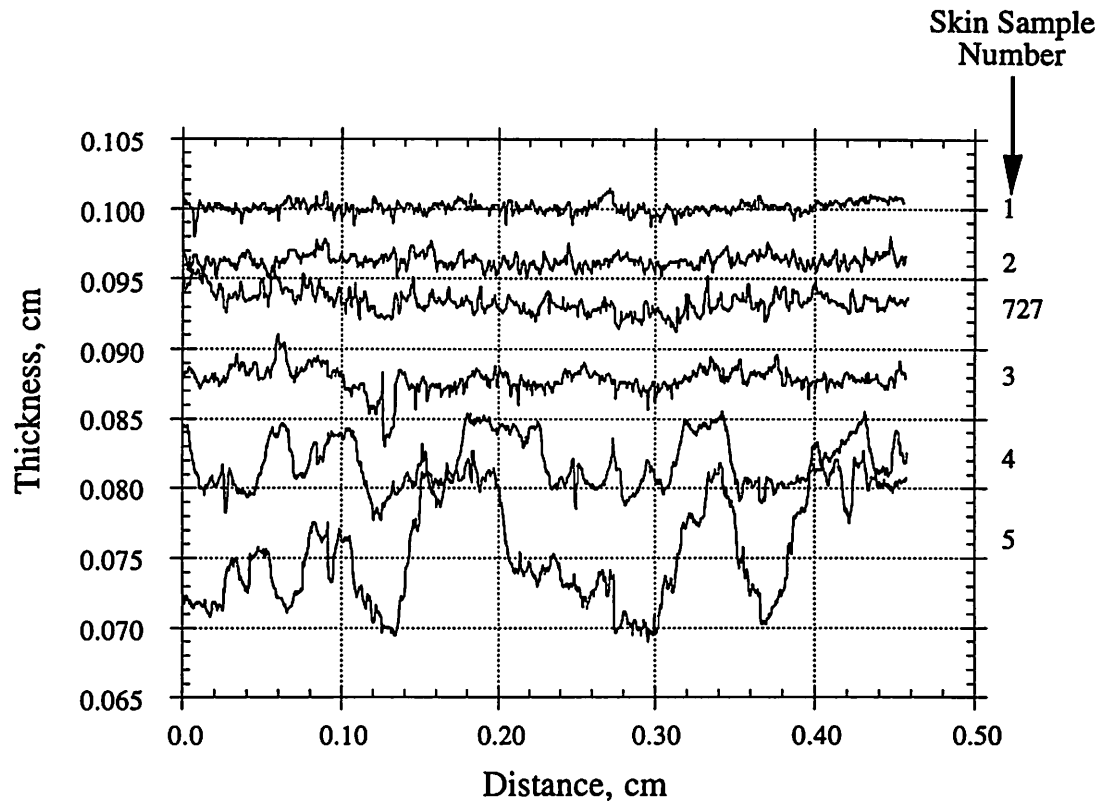


Figure 3.4: Surface profile comparisons of skin samples produced by an electrochemical corrosion process and a skin sample taken from the belly section of a serviceable Boeing 727. Original aluminum skin thickness was 40 mils (1.02 mm).

Table 3.1: Characteristics of aluminum skin samples corroded with an electrochemical corrosion process and a naturally corroded skin sample

Skin Sample Number	Corrosion Reaction (hours)	Mean Thickness (cm)	Thickness Loss (mm)	Thickness Loss (%)
1	4.0	0.100	0.016	1.60
2	8.0	0.096	0.056	5.50
727	—	0.093	0.086	8.60
3	10.0	0.088	0.140	13.4
4	12.0	0.082	0.200	19.3
5	16.0	0.076	0.260	25.2

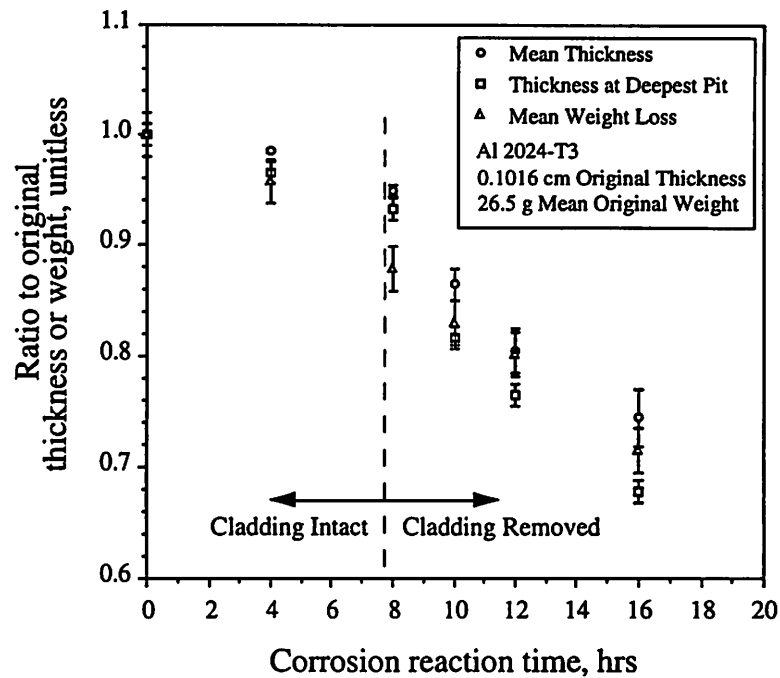


Figure 3.5: Mean thickness reduction, deepest pit formation, and mean weight loss vs. corrosion reaction time for uniform metal thinning corrosion by an electrochemical process.

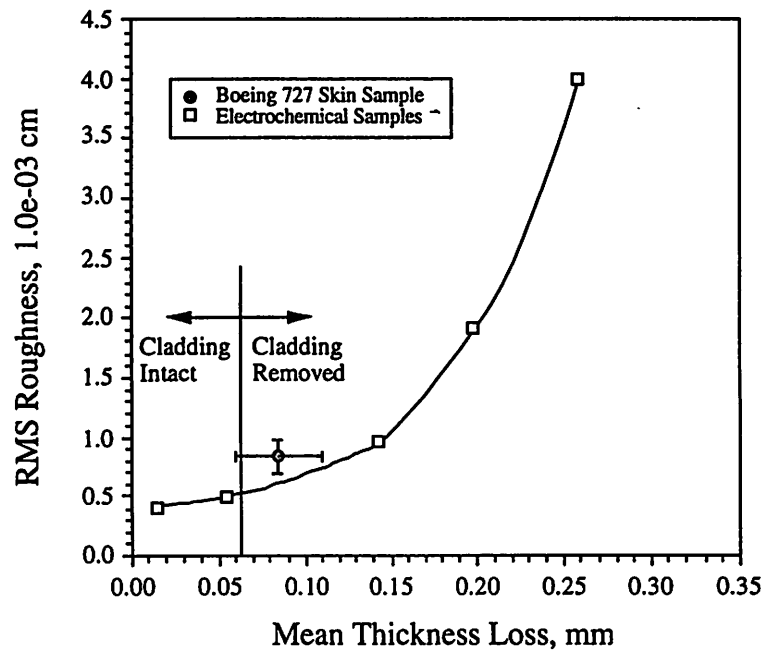


Figure 3.6: Comparisons of RMS roughness vs. mean thickness loss for samples corroded by an electrochemical process and a sample taken from the belly section of a Boeing 727. Taken from the data of Fig. 3.4.

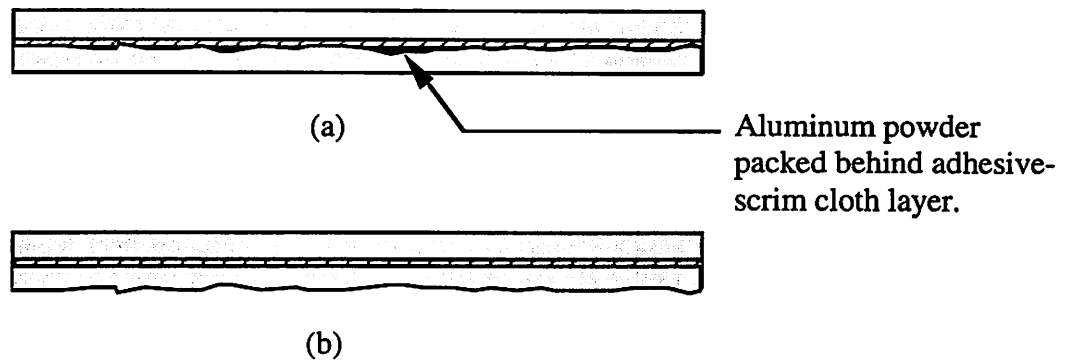


Figure 3.7: Aluminum/adhesive lap-splice assemblies with scrim cloth and second layer corrosion. (a) Corrosion behind the scrim cloth layer on the interior side of the second layer, voids filled with aluminum powder to allow ultrasonic energy transmission. (b) Corrosion on the exterior side of the second layer.

side down, corrosion can be simulated on both interior aluminum surfaces. The corrosion products resulting from the electrochemical corrosion process are left on the corroded aluminum surface and aluminum powder is packed into the corrosion pits to eliminate trapped air from within the bondline. It should be recognized that, despite these attempts to simulate corrosion at the bondline, there will be differences between a lap splice corroded first and then bonded and one that follows the natural sequence of bonding and then corrosion. Exterior corroded surfaces were bonded first, then corroded using the same process outlined above. The thickness of the corroded skin layer in each lap splice sample refers to the mean thickness of the skin sample shown in Fig. 3.4.

2. "Blow-out" samples

To simulate a localized "blow-out" corrosion pit in the aluminum skins, a platinum wire electrode was oriented perpendicular to the aluminum surface as shown in Fig. 3.8. For localized corrosion the configuration of the power supplies is identical to that shown in Fig. 3.3, with the positive lead from the programmed power supply attached to the platinum wire and the negative lead attached to the aluminum skin. The separation distance and voltage level for corroding aluminum skins to produce a localized "blow-out" was chosen to give the deepest pit formation with the least amount of surrounding cladding loss. Consistency between samples corroded in a localized "blow-out" manner was monitored by weight loss, deepest pit formation and the diameter of the cladding removed from the area surrounding the pit.

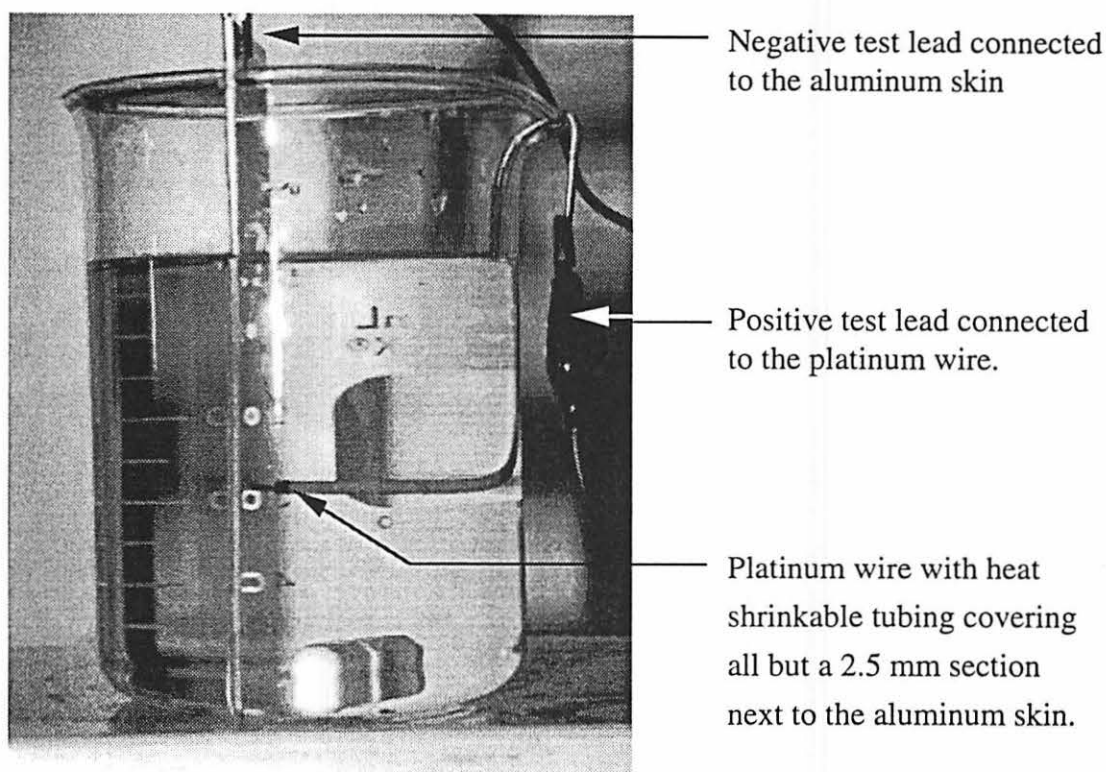


Figure 3.8: Experimental setup - Aluminum skin and platinum wire in a glass beaker, configured to produce a localized "blow-out" corrosion pit.

The micrographs of Fig. 3.9 compares the localized corrosion produced electrochemically using the setup shown in Fig. 3.8 with naturally occurring "blow-out" pits. The corrosion pit shown in Fig. 3.9.b was one of the largest "blow-out" pits sites found on the Boeing 727 skin sample. A comparison of the two micrographs in Fig. 3.9 shows that the naturally occurring corrosion pit is more compact horizontally than the laboratory produced corrosion pit. Another difference between the two cases is the "pillowing" of the naturally occurring corrosion pit. This seems to be caused by the corrosion by-products pushing a layered section of aluminum skin outward. This pillow effect can not be duplicated using the electrochemical corrosion process, as the corrosion reaction is one-sided while the naturally occurring corrosion pit appears to have started internally to the aluminum skin.

The aluminum skin containing the blow-out pit shown in Fig. 3.9a was assembled into a lap splice with the corrosion located exterior to the surface. Its detection by PE ultrasound is compared in Fig. 3.10. Figure 3.10a was scanned using the overall amplitude of a 1 MHz pulse; while Fig. 3.10b was scanned using the first BSE of the bottom skin with a 15 MHz

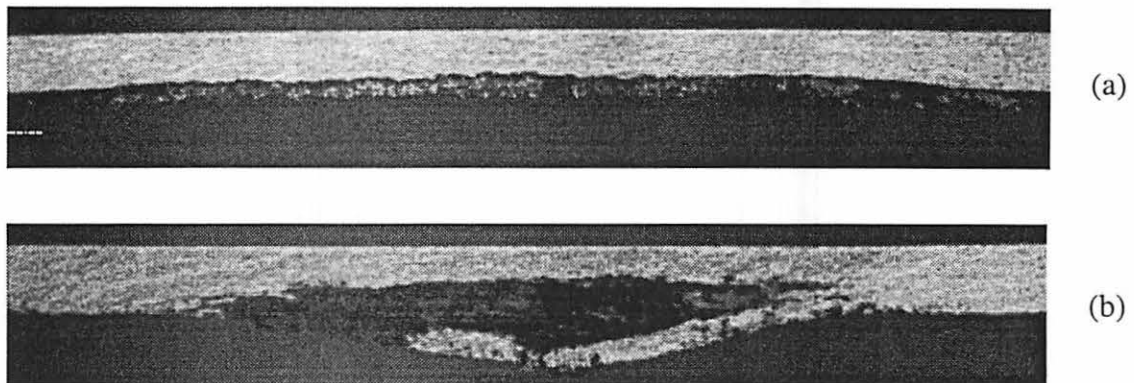


Figure 3.9: Cross-sectional micrograph of localized “blow-out” corrosion pits. (a) Corrosion pit produced electrochemically. (b) Large corrosion pit taken from a Boeing 727 skin sample. Images area: 0.71 x 0.10 in (1.8 x 0.26 cm).

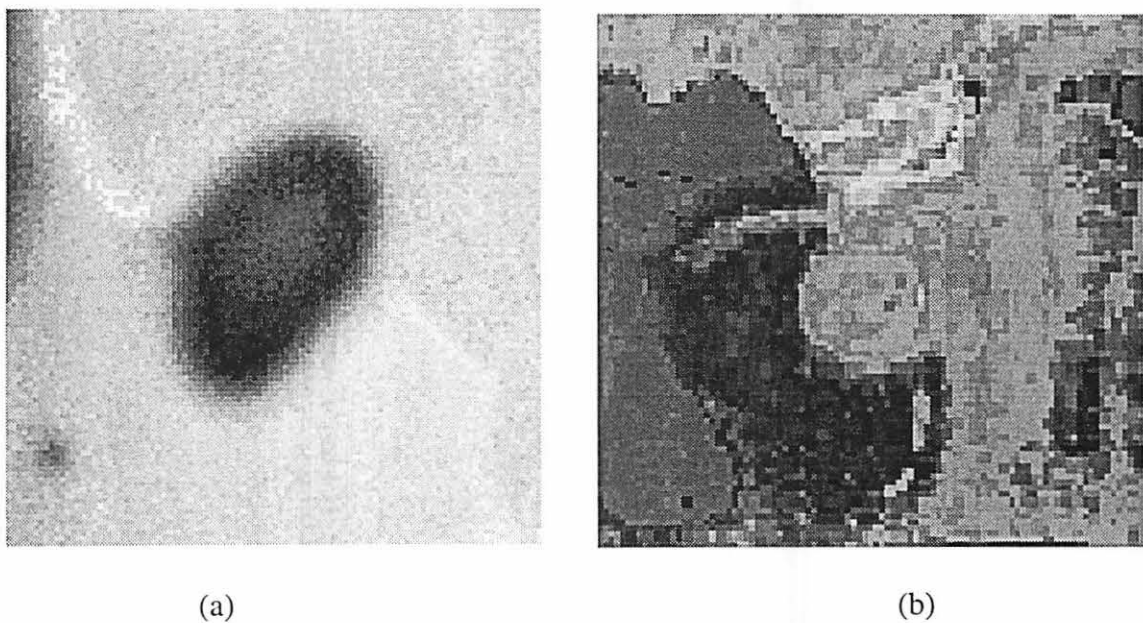


Figure 3.10: C-scans of a localized corrosion pit on the second layer of an aluminum/adhesive lap splice. (a) Image of the overall RF signal amplitude with 1 MHz. (b) Image of the first BSE amplitude from the bottom skin with a 15 MHz pulse. Scan area: 2.0 x 2.0 in (5.08 x 5.08 cm); step size: 10 mils (0.25 mm).

pulse. As seen, the low frequency inspection technique easily detects the corrosion pit through the top aluminum skin and the adhesive/scrim cloth layer. The pit can be detected in the high frequency image; however it is partially hidden by other features of the lap splice. If the corrosion pit weren't so large in diameter, it is doubtful that a high frequency pulse could detect the pit's presence.

F. Low Frequency Parameter Study

The purpose of this section is to define the ultrasonic parameters used with the low frequency inspection technique. The parameters of the technique are compared using C-scan images as a visual guide. The inspection parameters can be lumped into two principal categories, those affecting the transducer focal spot size and those dealing with the motor step size. Parameters affecting the transducer's focal spot size include: broadband frequency parameters such as center frequency and bandwidth, and transducer geometry parameters such as the focal length in water and element diameter. The motor step size is defined through the C-scan image density. The number of A-scan traces per area needed to produce a C-scan image with sufficient resolution, loosely defines the image density.

A series of C-scan images made on a lap splice with a fatigue-induced disbond provided insight into the technique's center frequency dependence. C-scan images made using two different types of broadband immersion transducers, on several different lap splice samples, provided insight into the technique's dependence on frequency bandwidth. The immersion transducers offered by Panametrics for general broadband focused-beam immersion testing come in two classifications, Videoscan and Acuscan. The design of the Videoscan immersion transducers provides maximum resolution in scattering and/or attenuating materials by heavily damping the transducer for a fast "ringdown". The lightly damped Acuscan "S" series transducers (High Sensitivity) provide sensitivity in material penetration through their narrow bandwidth, but suffer from poor near surface resolution [51]. Representative Videoscan and Acuscan radio frequency (RF) waveforms and their Fourier magnitudes of a pulse reflected from a flat titanium block are shown in Fig. 3.11 and Fig. 3.12 respectively. Figure 3.12 verifies that the bandwidth of the Acuscan transducer is indeed narrower when compared to the bandwidth of the Videoscan transducer. Also seen in Fig 3.12a, the broadband center frequency is not centered at 1 MHz, but rather slightly lower than 1 MHz for the Videoscan transducer. Such discrepancy is not unusual for ultrasonic broadband transducers and does not pose a concern for our comparisons.

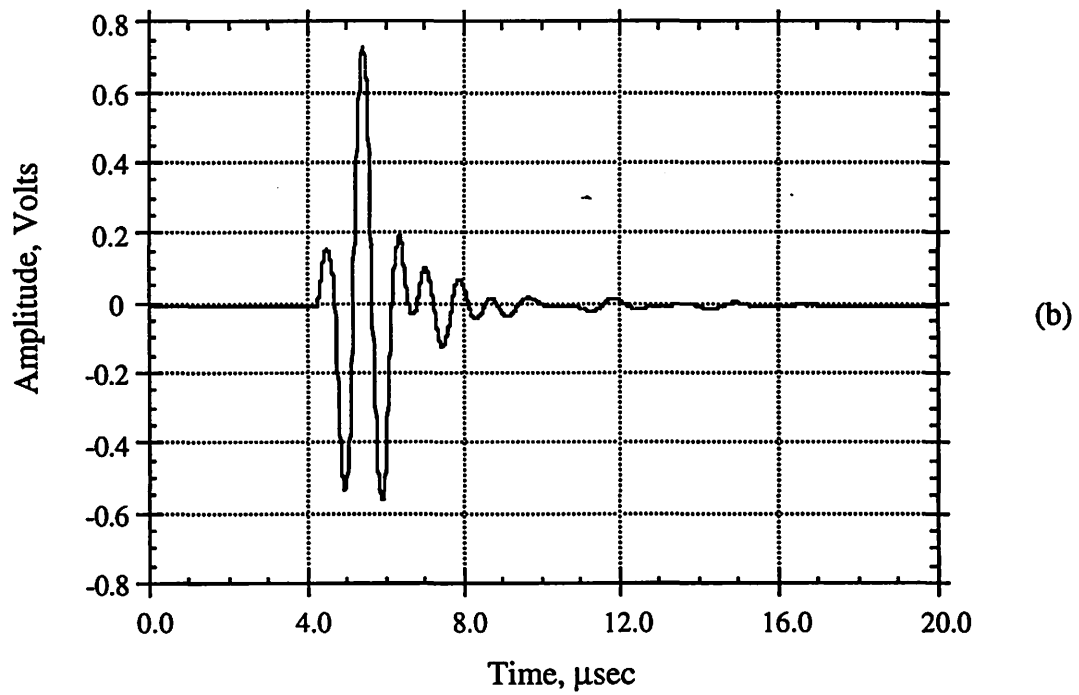
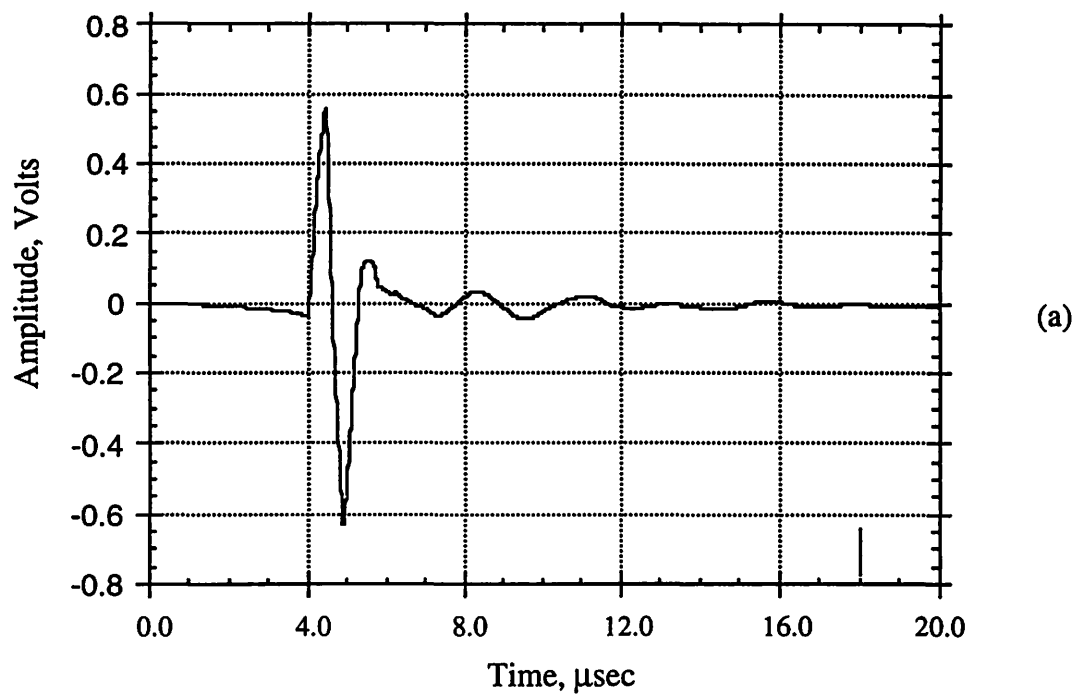


Figure 3.11: 1 MHz RF waveforms as reflected from a Ti block at their maximum peak-to-peak amplitude. (a) Videoscan transducer. (b) Acuscan "S" series transducer.

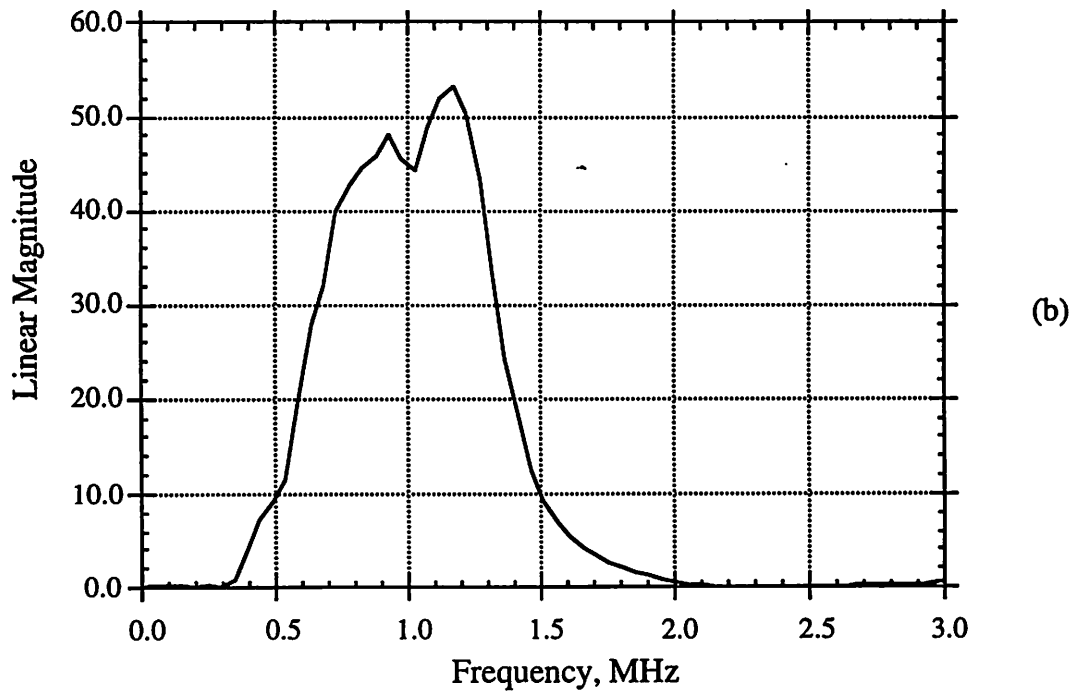
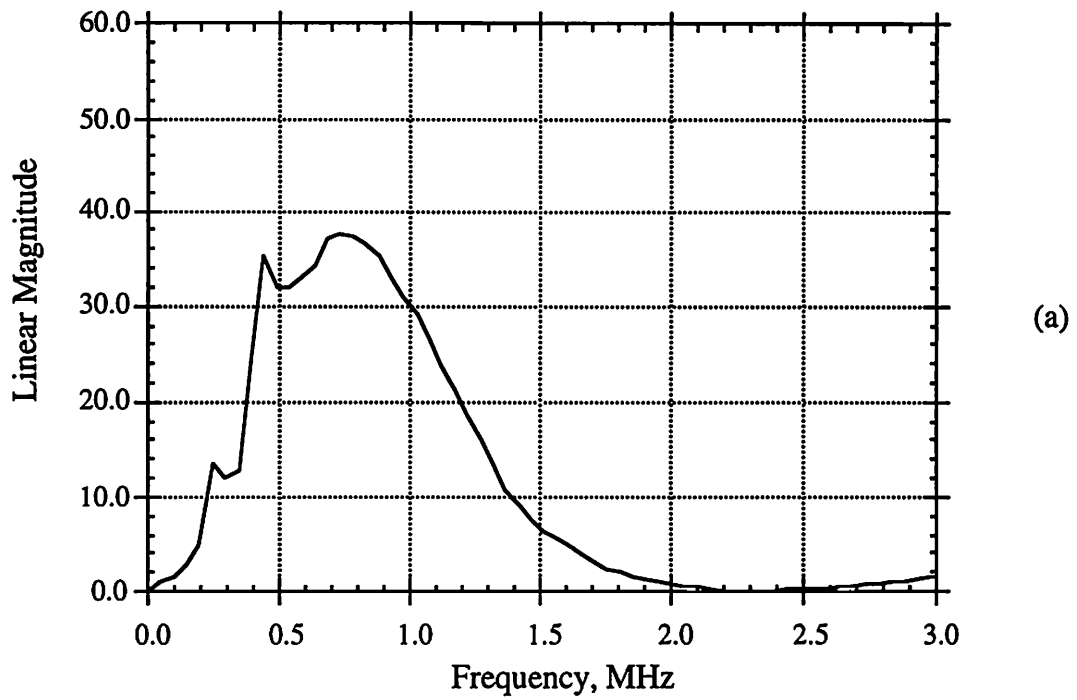


Figure 3.12: Fourier Magnitude of the RF waveforms shown in Fig. 3.11. (a) Videoscan transducer. (b) Acuscan "S" series transducer.

Each transducer's focal length in water was individually determined by maximizing the peak-to-peak (PP) amplitude of the RF signal when reflected from a reference titanium (Ti) block. Comparisons between the transducers were made at approximately the same peak-peak voltage when read from a digital oscilloscope. This was accomplished by adjusting the settings on the spiked voltage pulser/receiver as the transducer was focused onto the reference Ti block.

1. Influence of focal spot size parameters on disbond detection

In ultrasonics, focused beams are used because of the increased signal/noise ratio that they provide over flat piston immersion transducers. The focal spot size of an immersion transducer is dependent upon the transducer geometric focal length and element diameter, wavelength in the material, and broadband frequency. On the basis of a Gaussian beam model, the beam half-width at the $1/e$ point of the peak amplitude is given by Eq. (3.1) [51]. This focal location, Eq. (3.2), is referred to as the true focal point of the beam.

$$BW = \frac{W_o \beta}{\sqrt{1 + \beta^2}} \quad (3.1)$$

$$Z = \frac{F_o}{(1 + \beta^2)} \quad (3.2)$$

where:

$$\beta = \frac{\lambda F_o}{\pi W_o^2} \quad (3.3)$$

a. Influence of center frequency

Ultrasonic C-scan images produced using a set of five Videoscan focused-beam immersion transducers were compared on an aluminum/adhesive lap splice with a fatigue induced disbond condition. Although not identically the same, the water path focal length and element diameter of the transducers are comparable.

The peak amplitude C-scan images and their corresponding histograms are shown in Figs. 3.13 and 3.14 respectively. None of the transducers listed in Table 3.2 produces a resolved echo in a 40 mil (1.02 mm) aluminum skin; and thus the images created in Fig. 3.13 are made using a front surface (unresolved) reflection from the lap splice. The disbond area

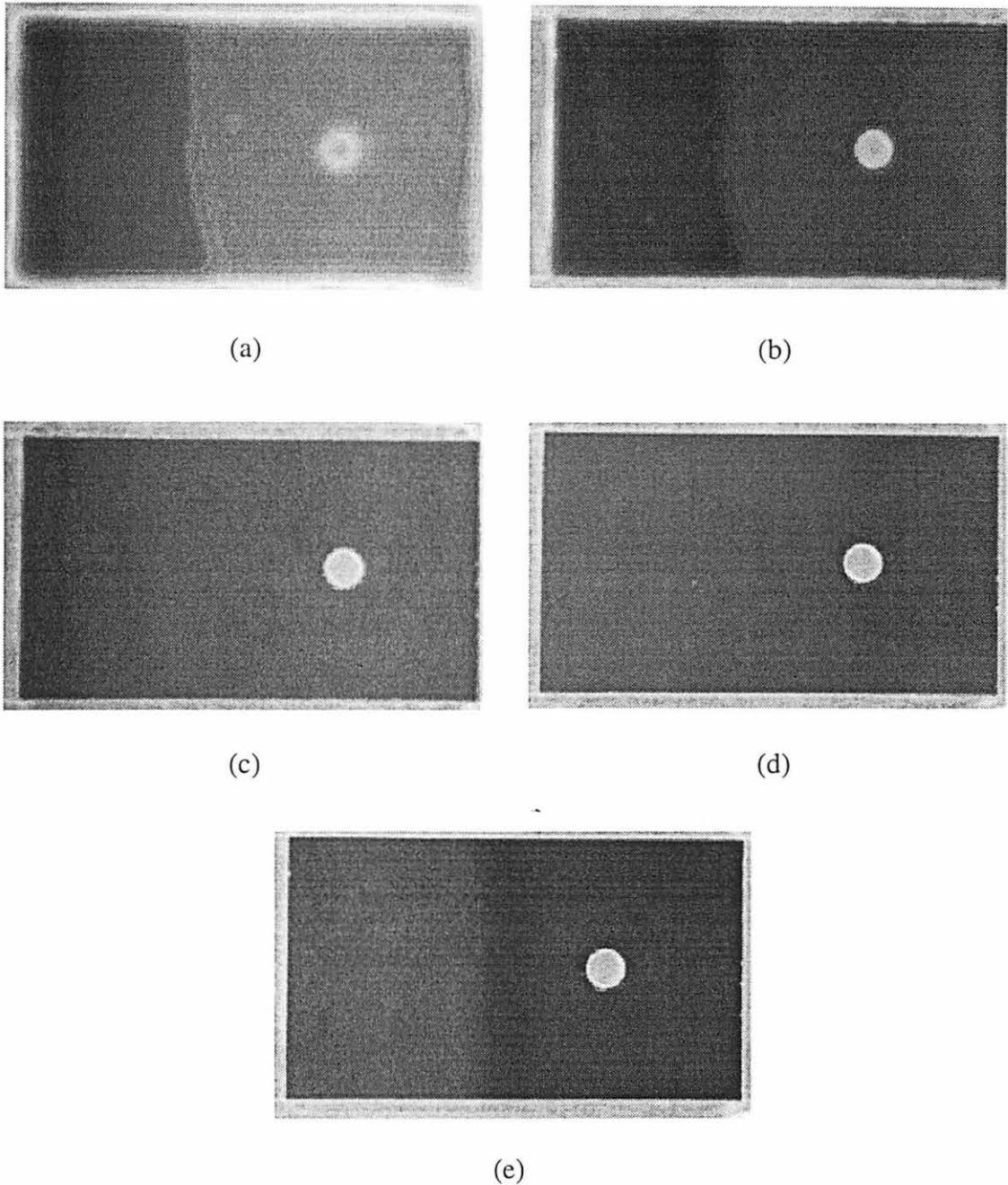


Figure 3.13: Peak amplitude C-scans showing the fatigue-induced disbond area located along the left side of the aluminum/adhesive lap splice at different transducer broadband center frequencies. The images are shown in their original gray scale form, without the aid of any contrast enhancements. (a) 0.5 MHz. (b) 1.0 MHz. (c) 2.25 MHz. (d) 3.5 MHz. (e) 5.0 MHz. Scan area: 3.0 x 5.0 in (7.62 x 12.7 cm); step size: 25 mils (0.64 mm).

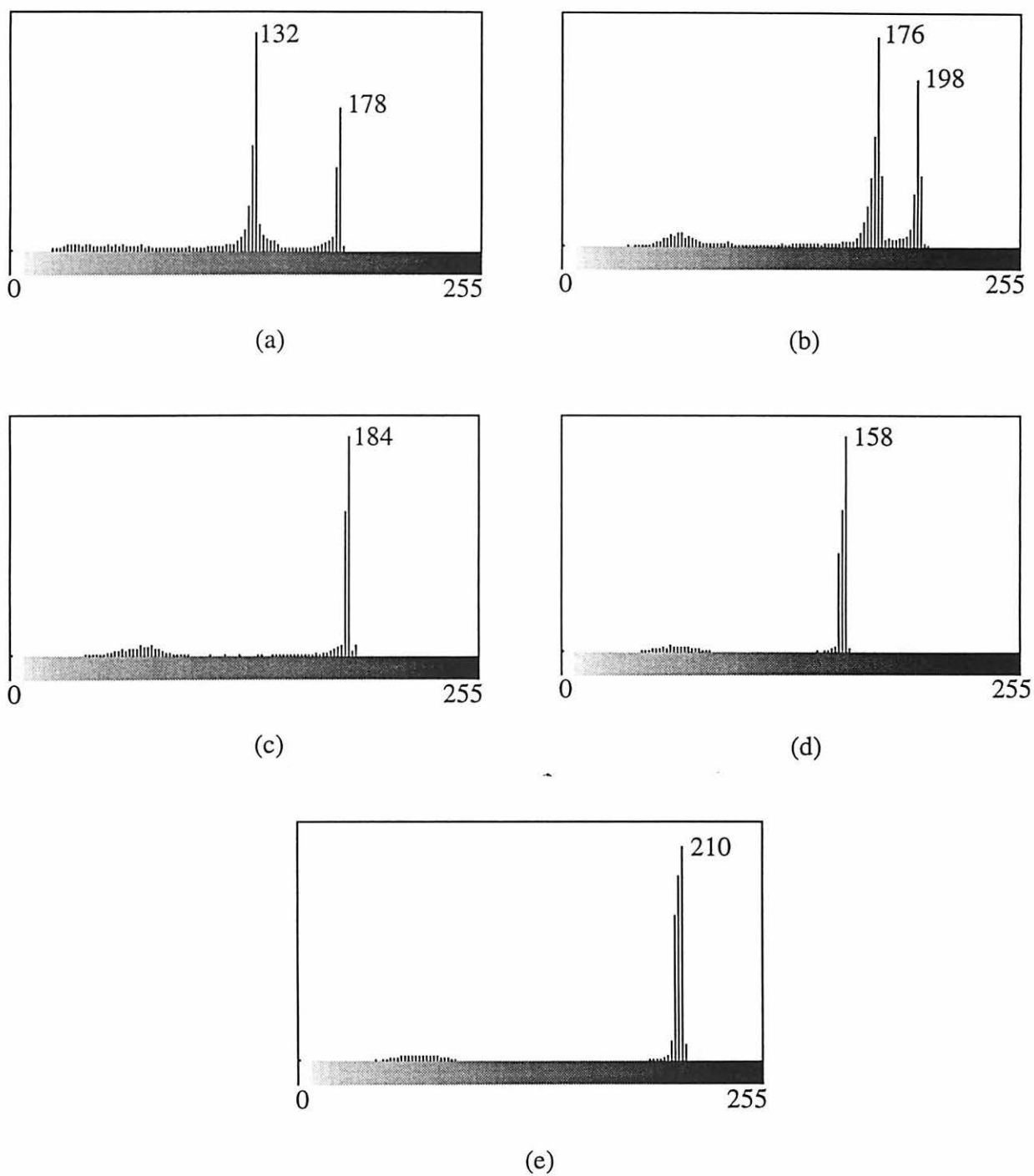


Figure 3.14: Color histograms of the images shown in Fig. 3.13. (a) 0.5 MHz. (b) 1.0 MHz. (c) 2.25 MHz. (d) 3.5 MHz. (e) 5.0 MHz.

Table 3.2: Parameters of Videoscan focused-beam immersion transducers used for detection of a fatigue induced disbond in an aluminum/adhesive lap splice

Videoscan Transducer Part Number	Center Frequency (MHz)	Element Diameter (inch)	Focal Length in Water (inch)	True Beam Width (mils)	Serial Number
V389	0.5	1.5	2.5	310	164577
V302	1.0	1.0	2.0	190	11560
V304	2.3	1.0	2.0	88	172293
V380	3.5	1.0	2.0	57	172292
V307	5.0	1.0	2.5	50	67639

shown in Fig. 3.13 is seen as the darker colored region on the left hand side of the images. The white circle on the right hand side of the images is a 0.375 in (9.53 mm) hole drilled through the sample (used during the fatigue-induced disbond process). In the histogram plots, the disbond is indicated by the higher color number, while the bond is indicated by the lower number. The images are shown in their original color scaling without the aid of any contrast enhancements, in order to show a direct comparison between the images and not the influence of image enhancements.

It is apparent from these two figures that a lower broadband center frequency transducer provides greater contrast between bonded and disbond areas in an adhesive lap splice using the low frequency inspection technique. For images that contain essentially two distinct color regions, the color histogram can be used to provide a simple contrast coefficient. Two distinct color regions in the image translate into two distinct peaks in the image's color histogram. A contrast coefficient is found by a ratio of the difference between the histogram peak numbers divided by the total color scale range as shown by Eq. (3.4). The contrast coefficient has been calculated for each transducer's image and listed in Table 3.3

$$\text{Contrast Coefficient} = \frac{\text{Higher Number} - \text{Lower Number}}{256} \quad (3.4)$$

From Table 3.3, the 0.5 MHz transducer provides almost twice the contrast than the 1 MHz transducer in detecting disbond areas. The remaining transducers, with center frequencies higher than 1 MHz, do not provide any obvious discrimination without the aid of contrast enhancements. However, other considerations such as spatial resolution also influence the optimization of the scan parameters.

Table 3.3: Contrast coefficients between bonded and disbonded areas in an aluminum/adhesive lap splice at different broadband center frequencies, taken from the color histograms of Fig. 3.14

Transducer Videoscan Part Number	Center Frequency (MHz)	Contrast Coefficient
V389	0.5	0.18
V302	1.0	0.09
V304	2.25	0.0
V380	3.5	0.0
V307	5.0	0.0

b. Influence of frequency bandwidth

Ultrasonic C-scan images produced using Videoscan and Acuscan “S” series focused-beam immersion transducers were compared on an aluminum/adhesive lap splice with a fatigue induced disbond condition. Both immersion transducers had element diameters of 1.0 in (2.54 cm) and focal length in water of 2.0 in (5.08 cm) as listed in Table 3.4. The comparison process is identical to that made for broadband center frequency dependence; but instead of comparing the effects of transducers with similar geometric features at different center frequencies the comparison is made between transducers of different frequency bandwidths. The frequency bandwidth is calculated using the full width at half magnitude of Fig. 3.12.

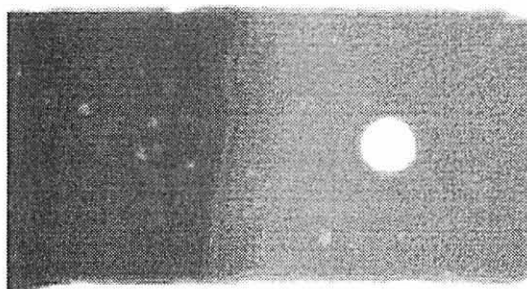
The C-scan results obtained with the Videoscan and Acuscan transducers are shown in Fig. 3.15, with their corresponding color histograms shown in Fig. 3.16. Again, the disbond area in the lap splice is indicated by the darker color region occupying the left half of the images. Both images shown in Fig. 3.15 revealed the disbond condition that exists in the lap splice; but the C-scan image made with the Videoscan transducer gives almost three times the contrast coefficient between bonded and disbonded areas than the Acuscan “S” series transducer does as shown in Table 3.5.

2. Influence of focal spot size parameters on corrosion detection

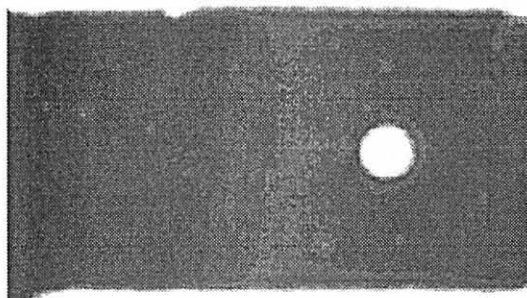
The Boeing Company Commercial Airplane Group fabricated a simulated first layer corrosion lap splice sample by riveting a naturally corroded aluminum skin (corrosion side interior) together with a second uncorroded aluminum skin. After assembly, top skin was painted with an enamel paint as illustrated in Fig. 3.17a. This sample contains no adhesive

Table 3.4: Parameters of Videoscan and Acuscan focused-beam immersion transducers used for detection of a fatigue induced disbond in an aluminum/adhesive lap splice at different frequency bandwidths

Transducer Identification	Center Frequency (MHz)	Frequency Bandwidth (% of Center Frequency)	Element Diameter (inch)	Water Path Focal Length (inch)	Serial Number
Videoscan V302	1.0	85	1.0	2.0	11560
Acuscan A302S	1.0	72	1.0	2.0	9675



(a)



(b)

Figure 3.15: Peak amplitude C-scans showing the fatigue-induced disbond area occupying the left half side of the aluminum/adhesive lap splice as obtained with different frequency bandwidths. (a) Videoscan transducer. (b) Acuscan "S" series transducer. Scan area: 3.0 x 5.0 in (7.62 x 12.7 cm); step size: 25 mils (0.64 mm).

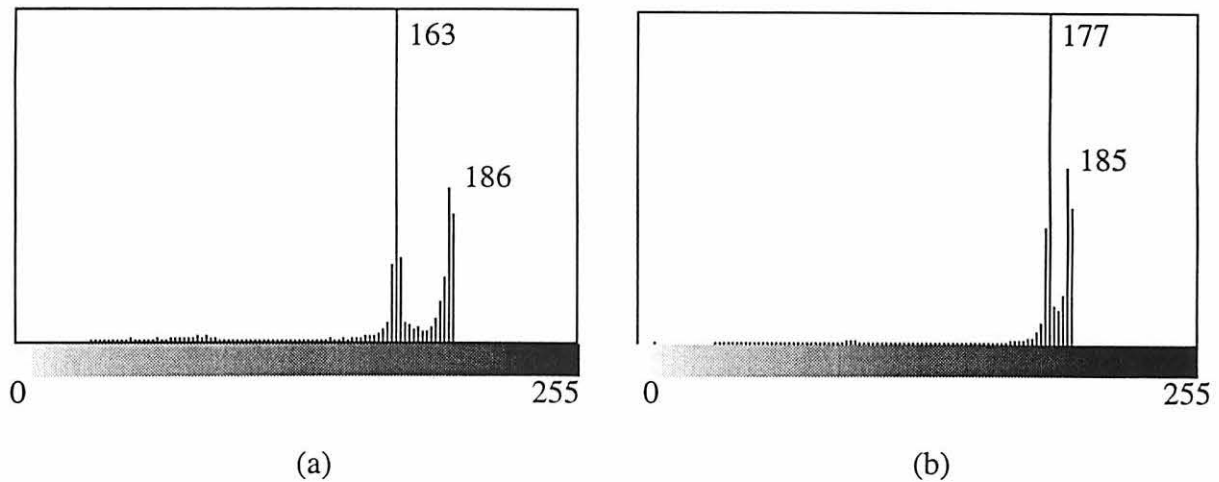


Figure 3.16: Color histogram of the images shown in Fig. 3.15. (a) Videoscan transducer. (b) Acuscan "S" series transducer.

Table 3.5: Contrast coefficients between bonded and disbonded areas in an aluminum/adhesive lap splice, at different broadband frequency bandwidths, taken from the color histograms of Fig. 3.16

Transducer Identification	Center Frequency (MHz)	Contrast Coefficient
Videoscan V302	1.0	0.090
Acuscan A302S	1.0	0.031

between the two aluminum skins and is representative of first layer corrosion over disbond areas as shown in Fig. 3.17b. With the interior air gap located in the lap splice, ultrasonic inspections made from the top skin can not distinguish between any of the configurations shown in Fig. 3.17. In all three cases the acoustic energy from pulse-echo ultrasonics is completely reflected from the bottom corroded surface of the top skin. The corroded aluminum skin in this sample was originally 71 mils (1.80 mm) thick. High frequency ultrasonics and eddy current measurements on the corroded skin determined that some of the corrosion pit areas have suffered as much as 45 percent metal loss.

The lap splice sample used for detection of second layer corrosion defects is similar to the samples used for disbond detection in all regards, except for the adhesive bondline material. In this sample the cold-bond adhesive contains 150 μm diameter glass beads instead of

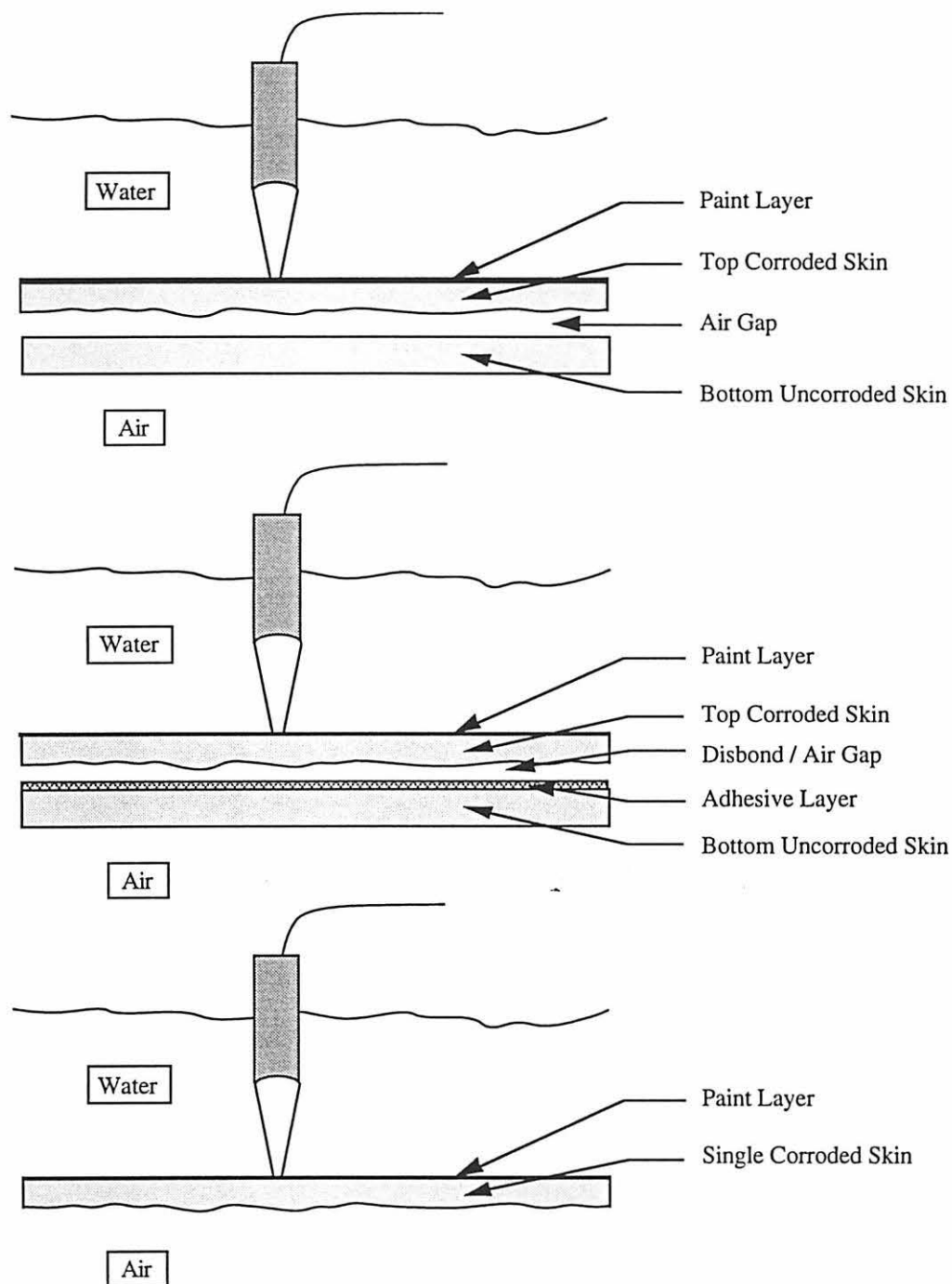


Figure 3.17: Side view of three samples containing first layer corrosion defects that give similar ultrasonic signatures. (a) Two aluminum skins fastened together with corrosion located interior to the splice and no adhesive bond. (b) Two aluminum skins fastened together with a disbond located between adhesive layer and the top corroded aluminum surface. (c) Single corroded aluminum skin.

scrim cloth. The glass beads provide for a uniform bondline thickness during sample fabrication. The disbond condition that exists in this sample was not fabricated intentionally, but rather the result of happenstance. Four hemispherical cavities ground into the bottom aluminum skin create the artificial second layer corrosion pits. Drops of hydrochloric acid (HCl) placed in and around the perimeter of the drilled cavities produced rough surface areas, typical of corrosion pits. Initial inspection of this lap splice sample, before the introduction of the corrosion pits, indicates that the adhesive in the disbond area is attached onto the top aluminum skin. A schematic of the second layer corrosion sample is shown in Fig. 3.18, and the dimensions of the artificial corrosion pits are listed in Table 3.6. As shown in Fig. 3.18, pit #4 is located under a disbond.

By the same argument given earlier concerning Fig. 3.17, second layer corrosion defects can be shadowed from pulse-echo inspection if a disbond condition exists in the lap splice. If corrosion is present in the bondline, a disbond condition probably exists in the lap splice, which makes the detection of second layer corrosion that much more difficult.

The detection of corrosion pits requires a high spatial resolution that is obtained with a compact focal spot size. The focal spot size can be decreased by shortening the transducer's focal length and/or decreasing the element diameter. The 0.5 MHz transducer is included in Table 3.7 for comparison because of its deeper material penetration compared to the 1 MHz transducers.

a. First layer corrosion detection

The lap splice orientation shown in Fig. 3.17a was used to compare the inspection sensitivity between the Videoscan and Acuscan transducers in detecting first layer corrosion using the low frequency inspection technique at 1 MHz center frequency. The comparison process is the same as described earlier for detecting disbond. Two time gates of the low frequency unresolved echoes are used in this comparison. Both the overall amplitude and the trailing portion of the unresolved RF signal can be used to detect uniform metal thinning due to corrosion. The amplitude of the trailing portion of the RF signal was found to be more useful than the overall signal amplitude in detecting aluminum skin thinning. The disadvantages associated with using the trailing signal portion of the RF waveform to detect metal thinning in the lap splice layers are the same ones associated with time-gating a higher frequency resolved signal. In higher frequency resolved echoes, the RF signal is complicated and great

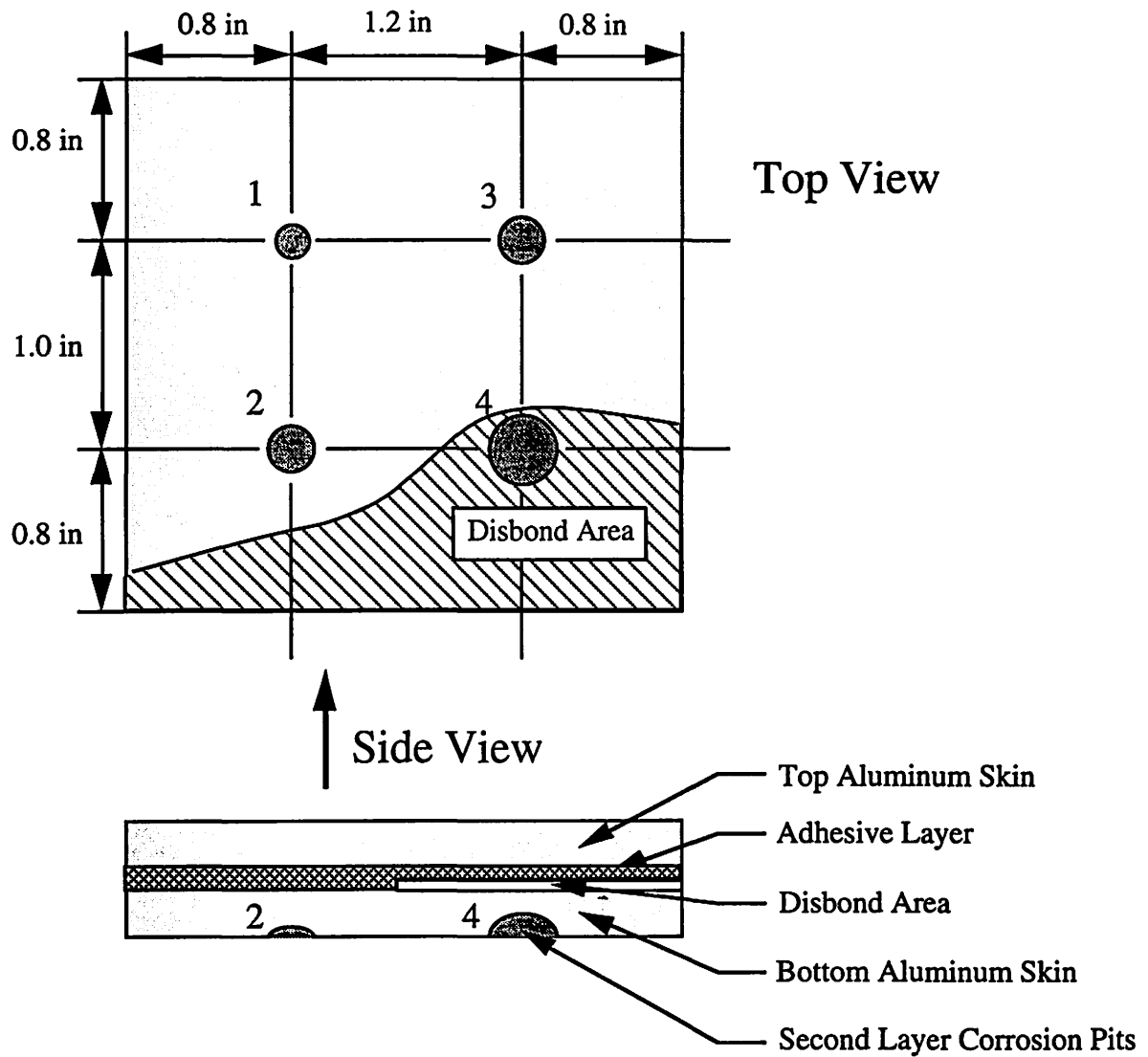


Figure 3.18: Lap splice with artificial second layer corrosion pits and disbond, shown in top and side views.

Table 3.6: Dimensions of artificial second layer corrosion pits

Hole Number	Pit Diameter, mils (mm)	Pit Depth, mils (mm)
1	190 (4.7)	5.0 (0.13)
2	200 (5.1)	14 (0.36)
3	170 (4.5)	10 (0.25)
4	280 (7.0)	24 (0.61)

Table 3.7: Parameters of Videoscan and Acuscan focused-beam immersion transducers used for detection of a first and second layer corrosion in an aluminum/adhesive lap splice

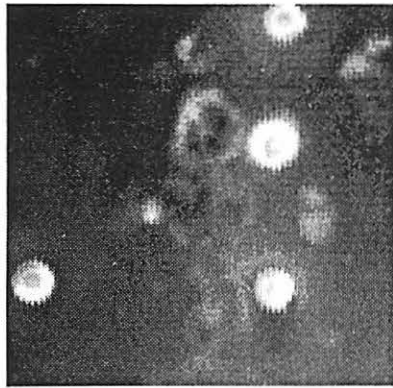
Transducer Identification	Center Frequency (MHz)	Element Diameter (inch)	Focal Length in Water (inch)	Serial Number
Videoscan V389	0.5	1.5	2.5	164577
Videoscan V302	1.0	0.75	1.0	172294
Videoscan A302S	1.0	0.75	1.0	178606

care must be exercised in placement of time gates associated with specific features of the lap splice. As the lap splice becomes corroded or disbonded, the placement of the time gates becomes more of an art than a science. However, for the purpose of *detecting* corrosion defects in lap splices, the advantages outweigh the disadvantages.

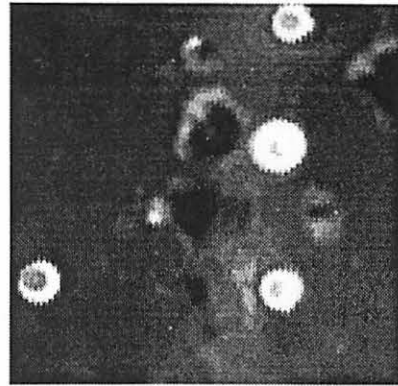
The results of the C-scan images using the 1 MHz transducers listed in Table 3.7 to detect first layer corrosion is shown in Figs. 3.19 and 3.20. Both transducers performed equally well in detecting first layer corrosion for both time gates. There is not an observable difference between the peak amplitude images shown together in Fig. 3.19 or the images shown together in Fig. 20. Comparing the images shown in Fig. 3.19 with those shown in Fig. 3.20, it can be seen that the images based on the amplitude of the trailing signal reveal more corrosion pit detail than images made with the peak amplitude of the overall RF signal. The Acuscan transducers hold the advantage over the Videoscan transducer when it comes to placement of trailing signal time gate. The narrowband characteristic of the Acuscan transducer is provided through lightly damping the transducer. Consequently, the RF signal contains several ringing peaks after the tripolar pulse, all of which can be time-gated to provide trailing signal peak amplitude information. Time-gating the trailing signal using the Videoscan transducer, on the other hand, involves capturing the peak amplitude changes of the third tripolar pulse, which can be more difficult.

b. Second layer corrosion detection

Detection of second layer corrosion pits in aluminum/adhesive lap splices is an area where the low frequency technique demonstrates its real benefit. Corrosion that occurs on the second layer of a lap splice is by far the most difficult to detect and likewise to character-

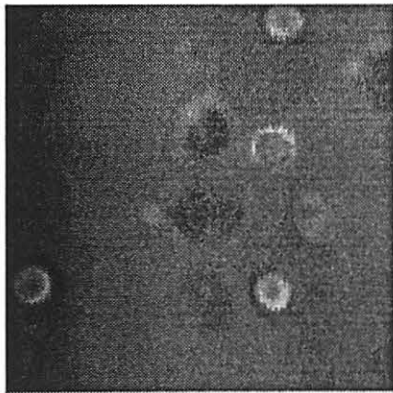


(a)

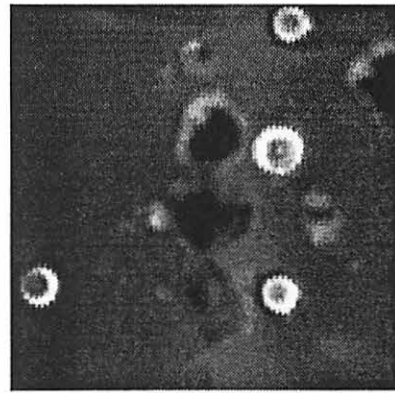


(b)

Figure 3.19: Peak amplitude C-scans of a lap splice sample with first layer corrosion and no adhesive. (a) Videoscan transducer. (b) Acuscan "S" series transducer. Scan area: 3.5 x 3.5 in (8.9 x 8.9 cm); step size: 25 mils (0.64 mm).



(a)



(b)

Figure 3.20: Trailing signal peak amplitude C-scans of a lap splice sample with first layer corrosion and no adhesive. (a) Videoscan transducer. (b) Acuscan "S" series transducer. Scan area: 3.5 x 3.5 in (8.9 x 8.9 cm); step size: 25 mils (0.64 mm)

ize. Its detection by ultrasound is hampered by the layered nature of the lap splice and the possibility that a disbond condition can shadow any corrosion defects that exist in the second layer. The effects of broadband center frequency and motor step size were investigated using the lap splice illustrated in Fig. 3.18 and the two Videoscan transducers listed in Table 3.7. The results of the broadband frequency comparisons are shown in Figs. 3.21 and 3.22.

In this section the comparisons made between the images are made without the aid of image contrast enhancement. This allows for a direct comparison between the original color scaled images and the inspection parameters. The images are shown contrast enhanced only for the purposes of publication and photo duplication.

Time gates placed to capture the overall RF signal amplitude, Figs. 3.21a and 3.22a, do not show any obvious indications of second layer corrosion pit formations. In comparison, the images produced using time gates placed to capture the amplitude of the trailing signal, shown in Figs. 3.21b and 3.22b, both show indications that there is defect in the lap splice. The fourth corrosion pit, located under the disbond area, is not visible. The hidden corrosion pit illustrates how a disbond can shadow the detectability of second layer corrosion defects in an adhesive lap splice.

3. Influence of motor step size on corrosion detection

Computer generated C-scan images are produced by color (gray) scaling a feature of the ultrasonic RF waveform as motor step controllers traverse the transducer over the sample in an x-y spatial grid. In creating a C-scan image, a fine step size (in length measurement)

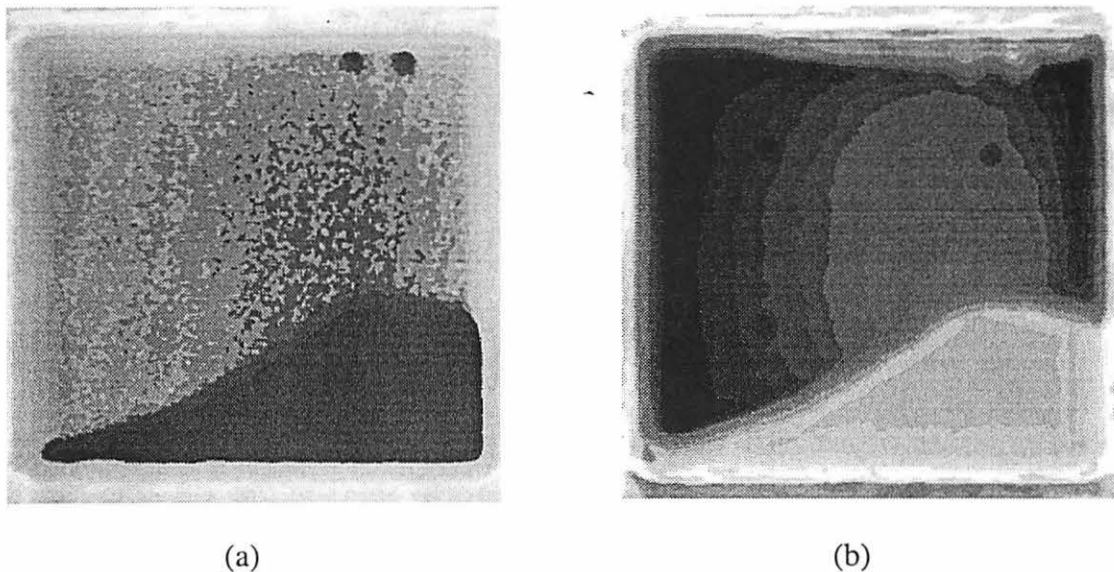


Figure 3.21: Peak amplitude C-scans of a bonded lap splice sample with second layer corrosion taken at 1.0 MHz broadband center frequency. (a) Overall amplitude signal @ 1.0 MHz. (b) Trailing signal @ 1.0 MHz. Scan area: 2.8 x 2.8 in (7.1 x 7.1 cm); step size: 10 mils (0.25 mm).

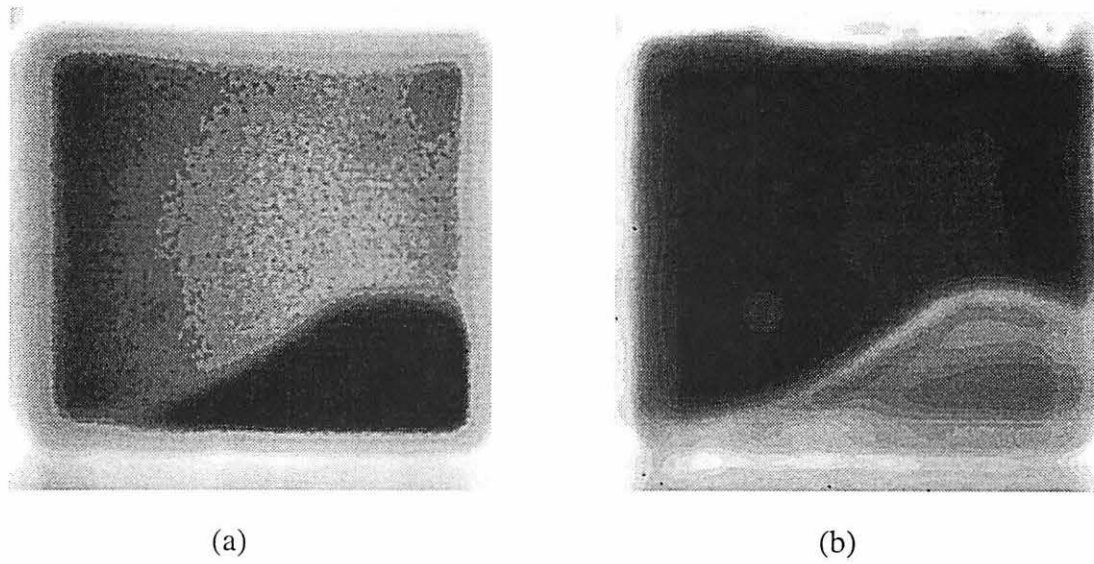


Figure 3.22: Peak amplitude C-scans of a bonded lap splice sample with second layer corrosion taken at 0.5 MHz broadband center frequency. (a) Overall amplitude signal @ 0.5 MHz. (b) Trailing signal @ 0.5 MHz. Scan area: 2.8 x 2.8 in (7.1 x 7.1 cm); step size: 10 mils (0.25 mm).

between each A-scan measurement location is critical for detecting small size defects in lap splice samples. A fine step size is beneficial, but too fine a step size, in comparison to the transducer's focal point size, results in an over sampled condition and does not provide any additional information at the expense of increasing the time necessary for inspection.

The determination of the best motor step size for defect detection is dictated by the resolution necessary to achieve the desired inspection. Lap splice samples manufactured in a laboratory typically contain only pristine defects such as well-defined bonded and disbonded areas (gross disbond). The lap splice samples manufactured at ISU fall into the gross disbond category. A few A-scan inspection points can determine whether a gross disbond exists, and a few more inspection points can map out the disbond edge. Considering the age of aircraft we are dealing with and the number of maintenance cycles performed on them, gross disbond sections may not exist. For the detection of gross disbonds in laboratory lap splice samples, a step size slightly less than diameter of the focal spot was found to be sufficient for mapping out the edge of the disbond. This is illustrated in Fig. 3.23 by reproducing the peak amplitude image shown in Fig. 3.13b at a step size of 0.16 in (4.1 mm). Again, the comparison between the images is made on pristine laboratory samples and may not be representative of actual aircraft bonding conditions.

The motor step size was increased until the three recognizable defects in the second layer corrosion pit sample became difficult to detect without the aid of image enhancements. The motor step size used to create the image of Fig. 3.21b was increased by 100 percent, and of Fig. 3.22b by 200 percent as shown in Fig. 3.24. A motor step size coarser than those indicated in Fig. 14 can detect pit #2; however a significant amount of image enhancement must

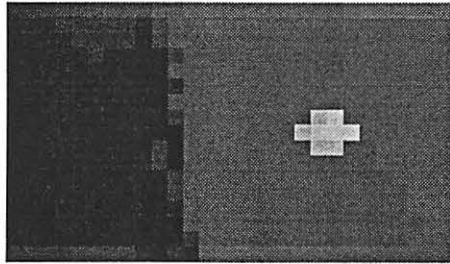


Figure 3.23: A 1 MHz peak amplitude C-scan showing the fatigue-induced disbond area located along the left side of the aluminum/adhesive lap splice. Reproduction of Fig. 3.13b at a larger step size. Scan area: 3.0 x 5.0 in (7.62 x 12.7 cm); step size: 0.16 in (4.1 mm).

be performed on the image to detect the pits #1 and #3. The true beam widths given in Table 3.1 for the 0.5 and 1.0 MHz transducer are approximately equal to or larger than the diameter of the second layer corrosion defects. A motor step size 1/10 the beam width at the true focal point appears to provide sufficient resolution for the detection of second layer corrosion pits with diameters comparable to the beam width at the true focal point.

4. Parameter Study Conclusions

The best overall results were obtained using a 0.5 MHz center frequency Videoscan transducer with a 1.5 in (3.8 cm) element diameter and a 2.5 in (6.4 cm) focal length (in water). The 0.5 MHz, Videoscan transducer provided the greatest contrast between bond and disbond areas in adhesively bonded lap splices; moreover it provided the best results detecting second layer corrosion pits using the overall RF signal amplitude and the trailing portion of the RF signal as time gates. The 1.0 MHz center frequency Videoscan transducer with a 0.75 in (1.9 cm) element diameter and a 1.0 in (2.54 cm) focal length (in water) also performed well in all categories. Because of its smaller size, the 1MHz transducer holds an advantage over the 0.5 MHz transducer when the transducers are incorporated into a portable ultrasonic scanning system.

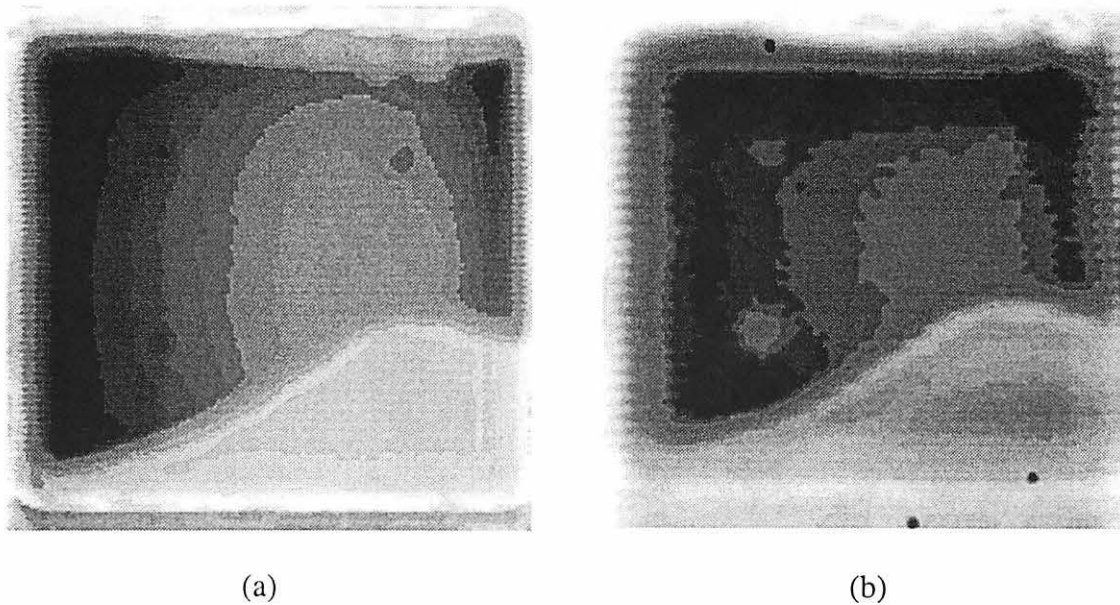


Figure 3.24: Peak amplitude C-scans of a bonded lap splice sample with second layer corrosion and a coarse motor step size. Scan area: 2.8 x 2.8 in (7.1 x 7.1 cm). (a) Trailing signal @ 1.0 MHz. Reproduction of Fig. 3.21b with a 20 mil (5.1 mm) motor step size. (b) Trailing signal @ 0.5 MHz. Reproduction of Fig. 3.22b with a 40 mil (1.0 mm) motor step size.

On laboratory lap splice samples with gross defects, a motor step size approximately equally to the focal beam width was found to be sufficient. The motor step size for detecting second layer corrosion pits was found to be 1/10 the focal beam size in large laboratory corrosion pits samples.

G. RF Waveform Modeling

The purpose of the ultrasonic model is to predict the RF waveform reflected from a layered structure given a reference RF waveform and knowledge of the material properties of each layer. The low frequency inspection technique, which relies primarily upon the amplitude of an ultrasonic pulse reflected from a layered lap splice can be modeled using a simple, linear, one-dimensional wave propagation model [53]. The computer code written in FORTRAN is included in the Appendix.

The ultrasonic model computes a linear transfer function and uses an input reference RF waveform to predict an output RF waveform based on the material properties of each layer.

With the aid of Fig. 3.25, the model steps are as follows: (a) a reference waveform is reflected from a suitable half-space and digitized; (b) this waveform is Fourier transformed into the frequency domain; (c) the reflection coefficient as a function of frequency, thickness, density and longitudinal velocity is recursively calculated for the layered system; (d) assuming linearity, the frequency components of the input reference waveform and the reflection coefficient calculations are multiplied together to produce a frequency spectrum representative of the RF waveform reflected by the layered system; (e) the resulting frequency spectrum is then inverse Fourier transformed back into the time domain where it is (f) compared to experimental time domain results.

In this research, the layer properties of the lap splices are not exactly known. This is a realistic situation as the material parameters for a lap splice assembly found on any aircraft will also be unknown. The low frequency inspection technique does not directly provide information about the lap splice's layer properties. The properties of each layer must be determined through other means. Some of the unknown parameters were determined through experimental investigations, and some are taken as textbook values, however they are all used as approximations in the model nonetheless.

1. Complex amplitude reflection coefficient derivation

The reflection coefficient at normal incidence is derived with the aid of Fig. 3.26. A pulse of unit amplitude is reflected from a one-dimensional single layer structure. The layered structure is assumed to have perfectly planar interfaces that allow for a continuity of stress and displacement. With an incident pulse of unit amplitude, the reflected pulses are assumed to be a superposition of waves reflecting and transmitting within the layer as

$$R = r_{10} + t_{01}r_{21}t_{10}e^{i\delta_1} + t_{01}r_{21}r_{01}r_{21}t_{10}e^{i2\delta_1} + t_{01}r_{21}r_{01}r_{21}r_{01}r_{21}t_{10}e^{i3\delta_1} + \dots \quad (3.4)$$

where:

$$\begin{aligned} r_{ba} &= \frac{z_b - z_a}{z_b + z_a} \\ t_{ab} &= \frac{2z_b}{z_b + z_a} \\ z_a &= \rho_a c_{L_a} \\ \delta_1 &= 2 \frac{2\pi d_1}{\lambda} \end{aligned} \quad (3.5)$$

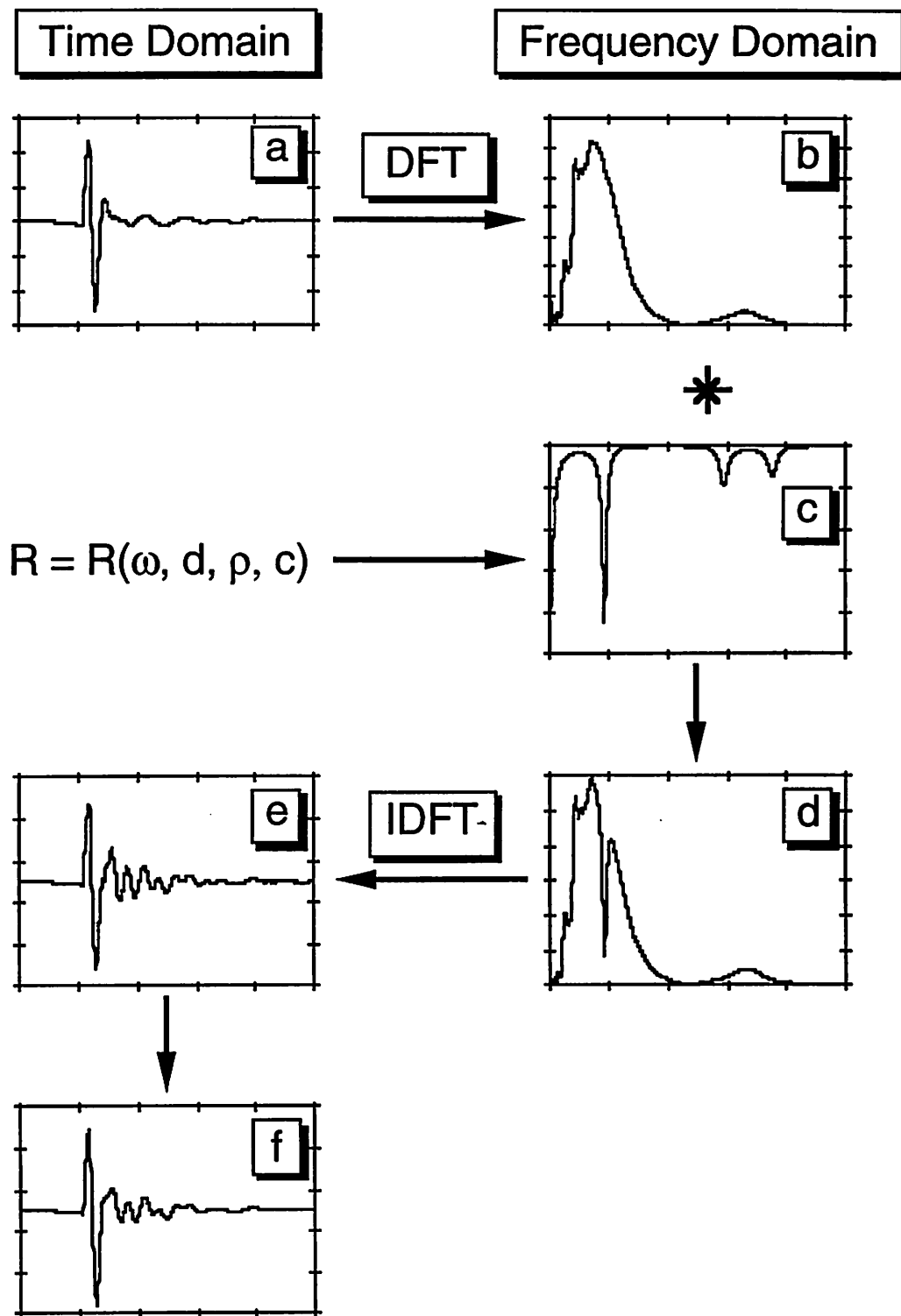


Figure 3.25: Procedural steps involved with the RF waveform model.

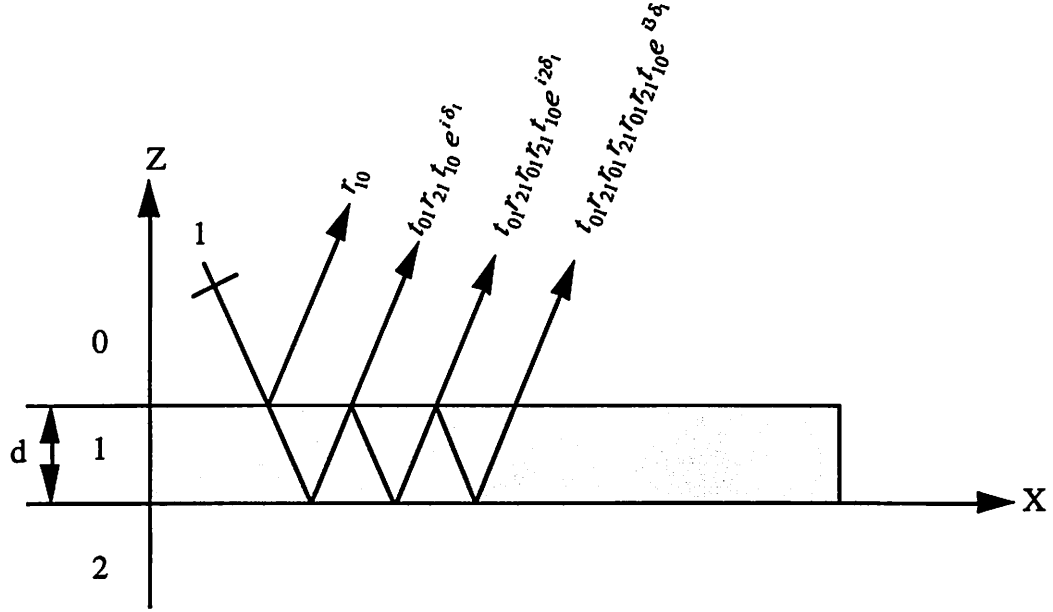


Figure 3.26: Complex amplitude reflections from a single layer.

The reflected waves in Eq. (3.4) can be written as an infinite series

$$R = r_{10} + t_{01} t_{10} r_{21} e^{i\delta} \sum_{n=0}^{\infty} [r_{01} r_{21} e^{i\delta_1}]^n. \quad (3.6)$$

The infinite series of Eq. (3.6) can be rewritten as

$$R = r_{10} + \frac{t_{01} t_{10} r_{21} e^{i\delta_1}}{1 - r_{01} r_{21} e^{i\delta_1}}. \quad (3.7)$$

The transmission terms in Eq. (3.7) can be transformed into reflection terms with the energy conserving relationships shown in Eq. (3.8) to give Eq. (3.9).

$$\begin{aligned} r_{10} &= -r_{01} \\ t_{01} &= 1 + r_{10} \\ t_{10} &= 1 - r_{10} \end{aligned} \quad (3.8)$$

$$R = \frac{r_{10} + r_{21} e^{i\delta_1}}{1 + r_{10} r_{21} e^{i\delta_1}}. \quad (3.9)$$

The reflection coefficient from a multi-layered structure can be obtained through succes-

sive application of Eq. (3.9) in each layer as shown in Fig. 3.27. Starting with Fig. 3.27b, the complex amplitude reflection coefficient, r^I for layer 3 is calculated using Eq. (3.9) and the real reflection coefficients, r_{43} and r_{32}

$$r^I = \frac{r_{32} + r_{43}e^{i\delta_3}}{1 + r_{32}r_{43}e^{i\delta_3}}. \quad (3.10)$$

Layer 3 has now been reduced to an effective solid. The complex reflection coefficient, r^II for layer 2 (Fig. 3.27c) is calculated using Eq. 3.10 and the real reflection coefficient, r_{21}

$$r^II = \frac{r_{21} + r^I e^{i\delta_2}}{1 + r_{21}r^I e^{i\delta_2}}. \quad (3.11)$$

Layers 2 and 3 are now an effective solid. The complex reflection coefficient, R for the entire structure (Fig. 3.27d) is calculated using Eq. 3.11 and the real reflection coefficient, r_{10}

$$R = \frac{r_{10} + r^II e^{i\delta_1}}{1 + r_{10}r^II e^{i\delta_1}}. \quad (3.12)$$

This recursive procedure can be used for any number of layers.

2. Modeling uniformly thinned lap splices

The relative changes in PP amplitude caused by metal thinning in one of the aluminum layers was calculated by decreasing the thickness of one aluminum layer while keeping all remaining material property parameters constant. Figure 3.28 is a representative comparison between several experimental A-scan traces and the model predictions. The samples contain uniform metal thinning in the second aluminum layer as illustrated in Fig. 3.7b. Agreement between experiment and theory was accomplished by minimizing an objective function (correlation coefficient) between the two RF traces. Because of the significant amount of computational effort and aprori knowledge required, the model's usefulness is limited to parameter studies where the effects of one or two parameters are investigated, leaving all other parameters constant.

The normalized PP amplitude predictions shown in Fig. 3.29 were obtained by dividing the calculated PP amplitudes (time gate positions shown in Fig. 2.12) of a thinned sample by

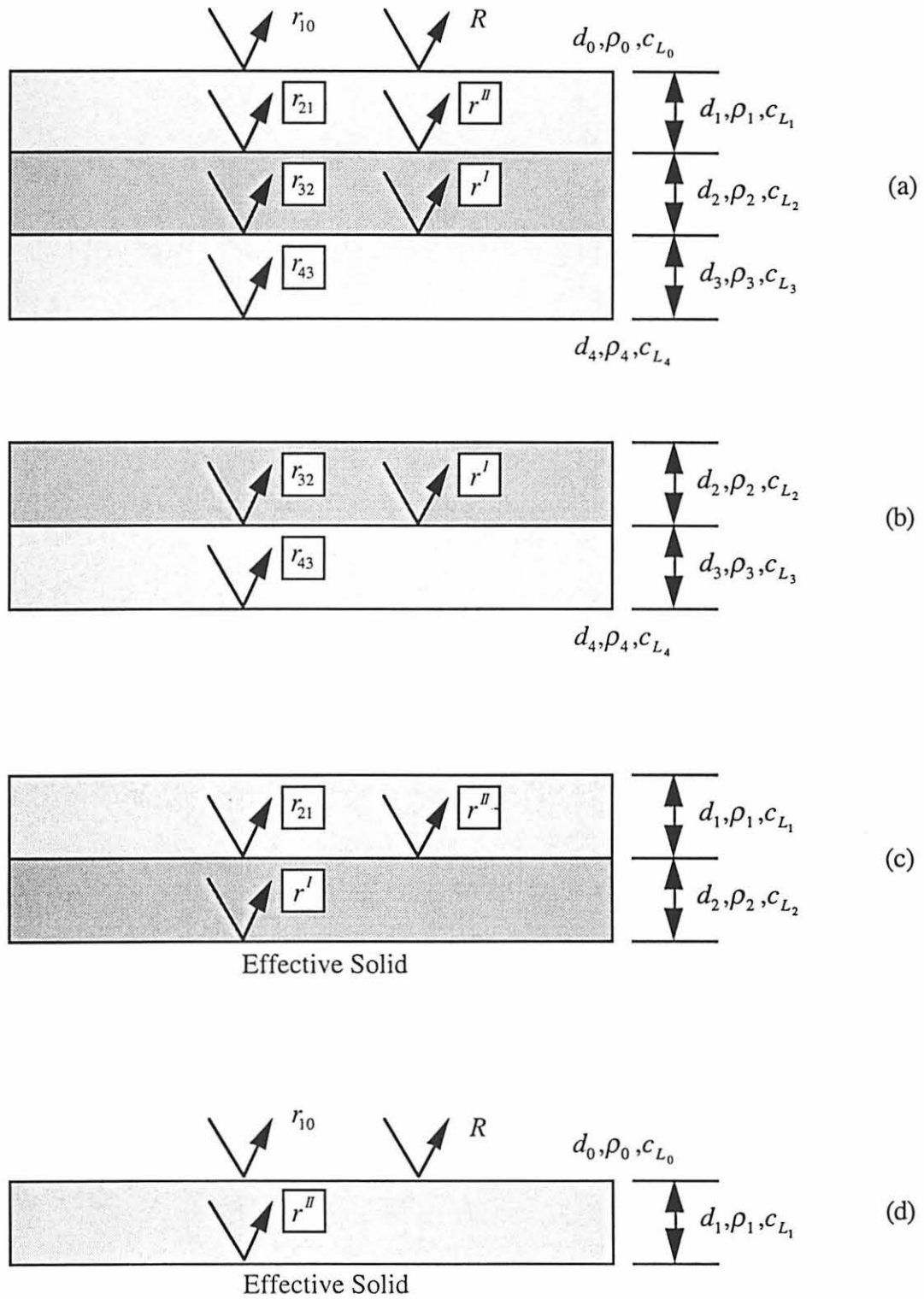


Figure 3.27: Application of Eq. (3.9) to obtain the reflection coefficient from a three layered structure.

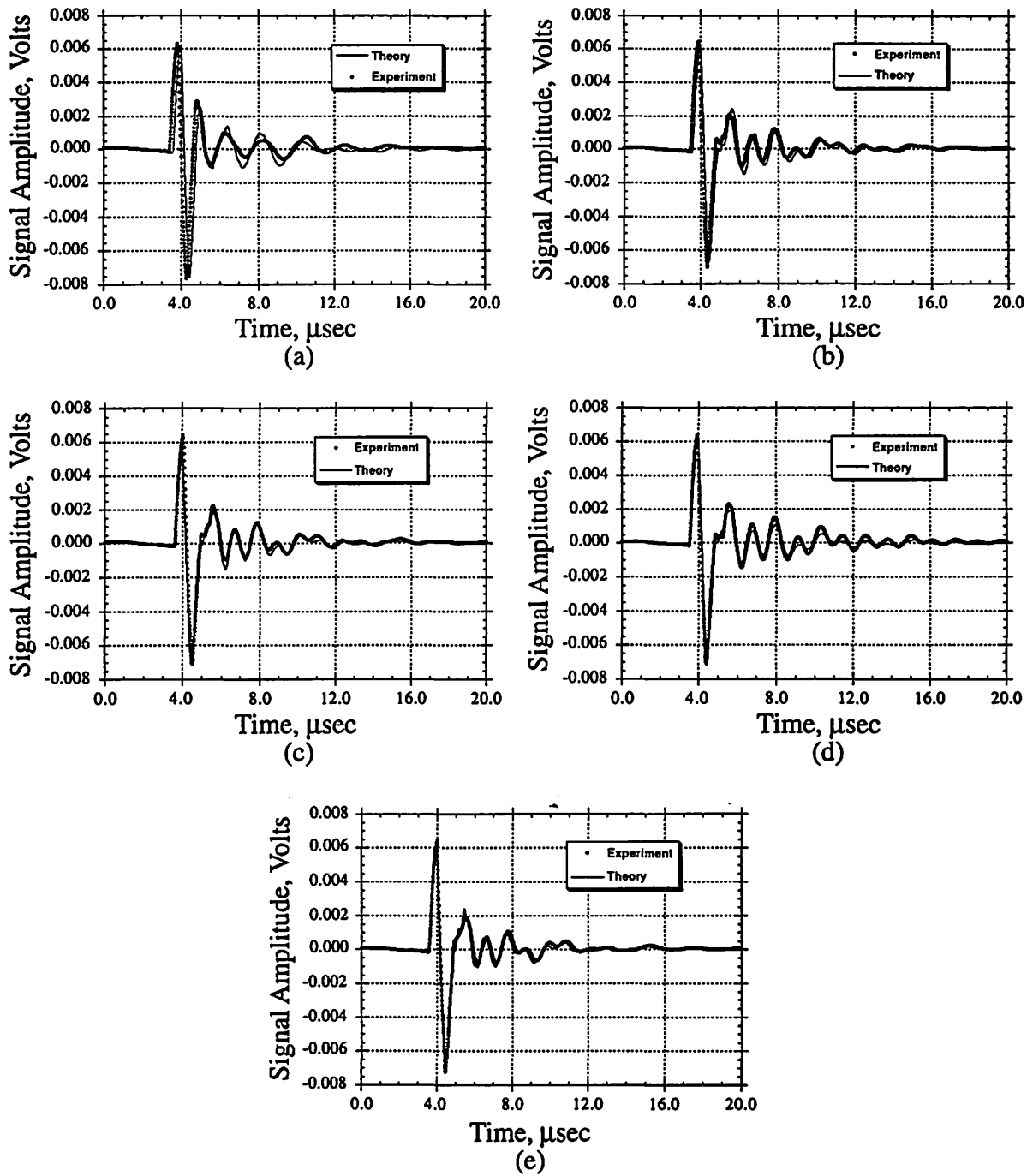


Figure 3.28: 1 MHz RF A-scan comparisons between experimental results and model predictions of aluminum/adhesive lap splices with uniform metal thinning in the second aluminum layer. (a) No thinning. (b) 1 % metal thinning. (c) 5 % metal thinning. (d) 20 % metal thinning. (e) 25 % metal thinning.

the respective PP amplitudes calculated for an unthinned reference sample. The reference sample used for the calculations has no metal thinning in either aluminum skin.

Excluding the Boeing 727 sample, the mean thickness of the skin samples shown in Fig. 3.4 were used in the predictions of Fig. 3.29. Each figure represents aluminum skin thinning, with all other parameters remaining constant. In the model it is assumed that a continuity of stresses and displacements exists across the planar boundaries; thus the mean thickness of the corroded layer is used, and more detailed calculations involving ultrasonic scattering from irregular boundaries can be ignored. The reduced thickness of the aluminum skin is used in the calculations and the model ignores whether the metal thinning takes places on the top or bottom surface of the aluminum skin layer. The experimental C-scan results taken with a 1 MHz pulse, on lap splices with first and second layer corrosion using skin samples 1, 2, 4 and 5 are shown in Figs. 3.30a-c. Skin sample 3 was made later and is not shown here in the C-scan results. Each image in Fig. 3.30 was individually equalized to enhance contrast.

a. First layer metal thinning

The theory predicts, in Fig. 3.29a, that a 25 percent reduction in first layer aluminum skin thickness will cause about a 3 percent decrease in the PP signal amplitude for the overall waveform, while at the same time increase the PP amplitude of the trailing signal by about the same amount. Comparing the theoretical predictions with the experimental results shown in Fig. 3.30a, it can be seen that with the same 25 percent reduction in first layer aluminum skin thickness, the overall waveform PP amplitude decreases while the trailing signal increases (white to black color corresponds to low to high PP amplitude). Theory and experiment exhibited the same trend that the PP amplitude of the overall waveform remains fairly constant in the range of mean thickness changes between skin samples 2 and 4. Any discrimination of first layer aluminum skin thickness between these samples should be made using the trailing signal.

b. Second layer metal thinning

Comparing Fig. 3.29b with Fig. 3.29a, it is seen that the roles of the overall waveform and trailing signal reverse. For second layer metal thinning in an adhesive lap splice the theory predicts that the overall waveform's PP amplitude will increase, while trailing signal's PP amplitude will decrease. This result is opposite to that predicted for first layer metal thinning in Fig. 3.29a. The theory also suggests that the greatest discrimination between the

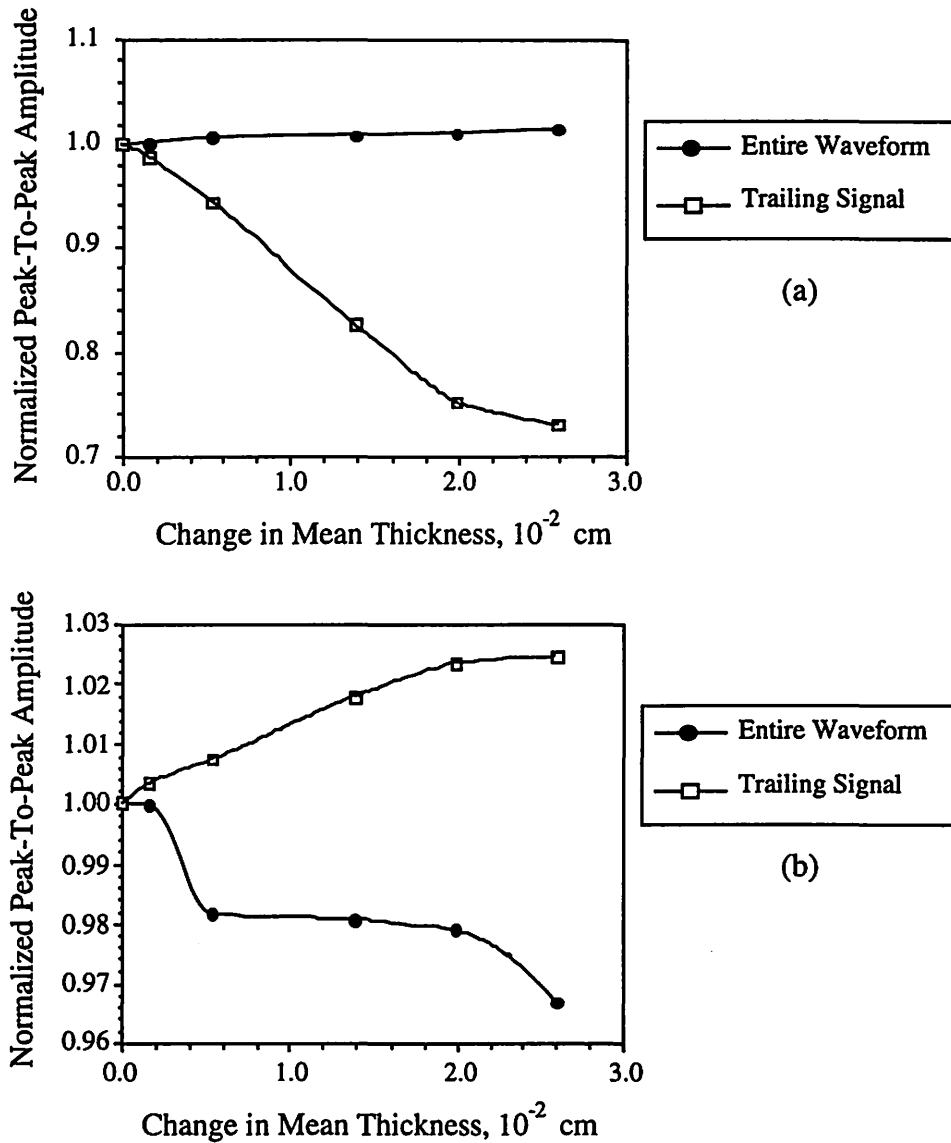


Figure 3.29: Theoretical peak-to-peak signal amplitudes for an aluminum/adhesive lap splice assembly normalized to an uncorroded “reference” sample. (a) Corrosion thinning in the first layer. (b) Corrosion thinning in the second layer.

samples should be made using the trailing signal. As the second aluminum layer becomes thinner, the change in the trailing signal’s PP amplitude is greater than 25 percent, while the PP amplitude of the overall waveform changes less than 2 percent. Experimentally we see, in Fig. 3.30b and Fig. 3.30c, that the signal amplitude reverses as discussed above; and the trailing signal does provide a greater discrimination between the samples.

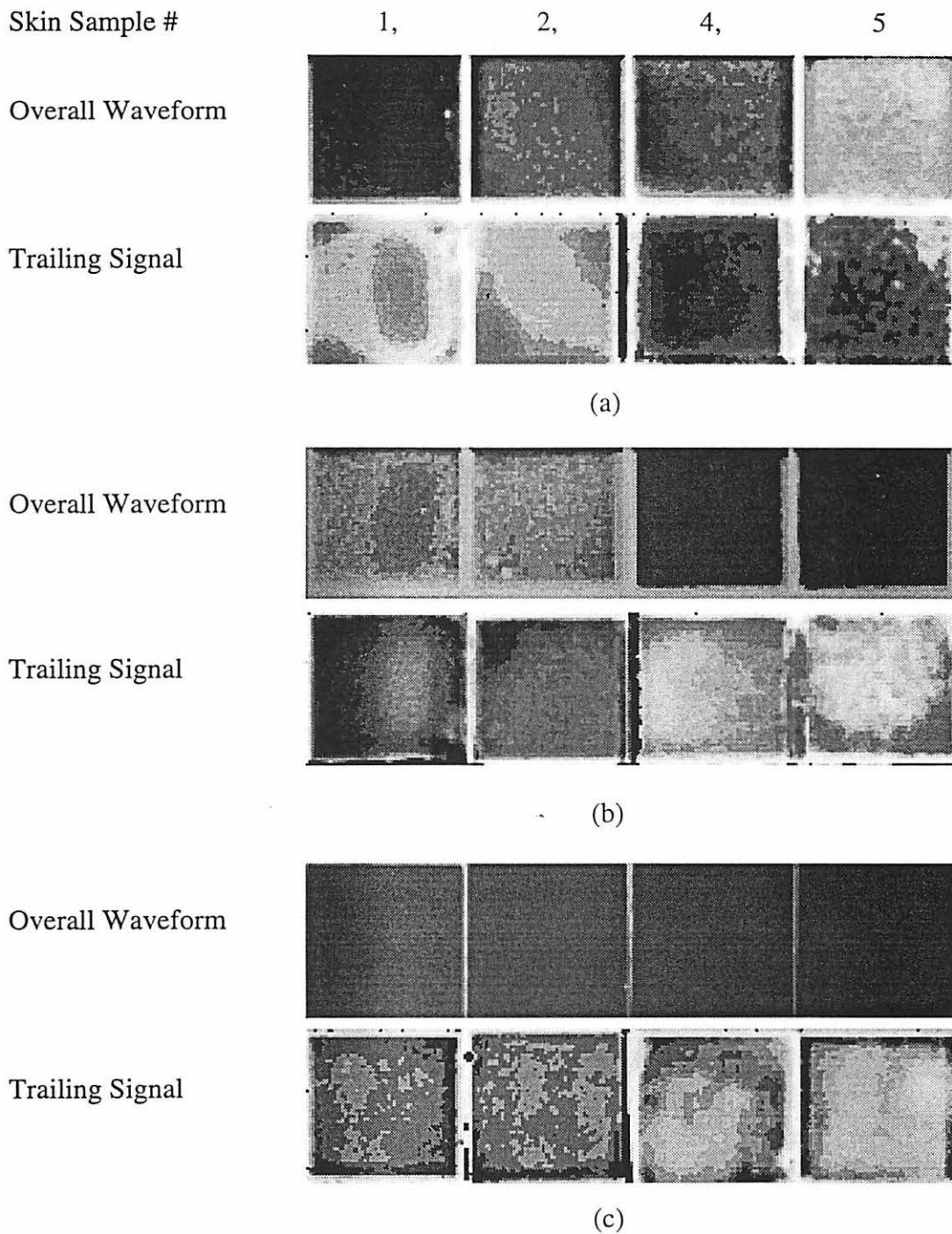


Figure 3.30: Experimental pulse-echo C-scan images of corroded aluminum/adhesive lap splices taken with a 1 MHz pulse. Each image was individually contrast enhanced. (a) Corrosion interior to the first layer. (b) Corrosion interior to the second layer. c) Corrosion exterior to the second layer. Scan area: 12.0 x 3.0 in (30.5 x 7.62 cm); step size: 10 mils (0.25 mm).

CHAPTER IV. THE DRIPLESS BUBBLER

In order for the low frequency technique to become a realizable technique for inspecting aircraft fuselage lap splices, there must exist a means to transfer it out of the immersion tank and onto the aircraft. The low frequency inspection technique performs well as a laboratory tool, but if it can not be applied to an aircraft fuselage in a cost effective manner, it has failed in one of its objectives.

It was shown earlier that the low frequency inspection technique could be applied for the detection of disbond and corrosion defects in aluminum/adhesive lap splices. It was also shown that C-scan images made in immersion and with the aid of an ultrasonic water squirter gave nearly identical results. This section details the design, development and testing of a prototype, called the Dripless Bubbler. The Dripless Bubbler was designed to allow for an ultrasonic C-scan inspection of the exterior of an aircraft fuselage while the aircraft is in a maintenance hangar environment. The main merits of the device are: (1) it permits a water-coupled, focused-beam, ultrasonic inspection of the aircraft fuselage without the problem of uncontained water; (2) it can be attached to a portable scanning device and used in any scanning orientation, even on vertical and overhead surfaces; and (3) it allows the scanning of areas with surface protrusions, such as buttonhead rivets.

A. Comparisons with Other Techniques

The Dripless Bubbler offers several advantages over other, currently available, noncontact ultrasonic inspection methods such as water squirters and “bubblers”; and contact methods such as direct contact, captured water columns, and “leakers”. Squirters are widely used by aircraft manufacturers to inspect parts for manufacturing flaws, but are not routinely used by air carriers as an ultrasonic inspection tool. The high costs of high quality (laminar flow) water squirter systems have prevented many air carriers from purchasing water squirter systems [54]. There are other disadvantages besides cost associated with using a water squirter to inspect an aircraft fuselage. With a water squirter the sound beam is focused at the exit of the housing, approximately near the location where the water is collimated for spraying. On the sample surface the beam is not truly focused, but rather collimated; and some of the signal-to-noise ratio benefits associated with focused-beam inspection are lost. Because of their uncontained water jets, a water squirter inspection is incompatible with an airline maintenance hangar environment. To cost-effectively inspect an aircraft fuselage, many squirters operating in parallel are needed. A water flow rate of 4 to 6 liters/min out of each

squirter is common. Multiplying the water flow rate by the number of squirters necessary and it becomes clear that a large quantity of uncontained water is involved.

Bubblers alleviate some of the disadvantages associated with squirter inspection. A bubbler can be loosely classified as a water squirter with a very low water flow rate, and a leaker is analogous to direct contact. Bubblers operate close to the sample surface and rely on the surface tension of the water to provide a constant water path for the sound beam. Leakers use a water-permeable membrane with a water flow such that a thin film of water couplant is maintained between the sample surface and the face of the transducer [55].

Contact methods are by far the least expensive means available to ultrasonically inspect single point locations on the fuselage. Some of these methods utilize focused beam transducers and some do not. A direct contact inspection has difficulty resolving near surface defects in lap splices without the aid of a buffer rod. The addition of the buffer rod improves the inspection capability at the expense of a very large front surface echo.

The main disadvantage associated with using a bubbler, leaker or any other contact technique to inspect an aircraft fuselage comes from their inability to scan over raised surface features found on an aircraft fuselage, such as buttonhead rivets and lap splice edges. Line scans between the rivet rows are possible with contact methods, but a water squirter is the only device that can effectively be used to make surface scans over the many raised surface features found on an aircraft fuselage. What is needed is a device that is cost effective, incorporates a focused beam transducer, and can scan over the raised surface features found on a lap splice, without any associated uncontained couplant problems.

B. Development of the Dripless Bubbler

At first glance, the requirements of an ultrasonic inspection tool that is cost effective, uses a focused beam, and can scan over raised surface features without any associated uncontained couplant problems seems rather prohibitive. The development of the Dripless Bubbler came out of the desire to minimize the flow rate of a water squirter. This task would have been simple had it not been for the need to include the low frequency inspection technique as one of the constraints. Because of the inclusion of the low frequency inspection technique as part of the design, the opening of the water squirter must be large enough to accommodate the diameter of the rather large focal spot size.

1. Modified water squirter

A modified ultrasonic water squirter, manufactured at ISU, provided a starting point for the design. The water squirter accommodated a 1 MHz focused immersion transducer with a 1.0 in (2.54 cm) element diameter and a 2.0 in (5.08 cm) focal length. It was designed using geometrical considerations and the transducer's assumed focal path and beam spread. The exit diameter of the squirter was 0.25 in (6.4 mm). No problems were encountered maintaining laminar flow out of the squirter exit with a low flow rate.

The water squirter was initially used with the water column oriented vertically and the water was gravity fed onto a surface at various heights. The reflected RF signal was recorded and the PP amplitude measured at 0.1 in (2.5 mm) heights from 0.0 to 1.0 in (0.0 to 2.54 cm). At a height of 0.12 in (3 mm) a majority of standard size button head rivets installed on a fuselage lap splice can be cleared. The flow rate out of the water squirter using gravity feed in this orientation was 0.2 gal/min (0.76 l/min), less than that typically used for a water squirter inspection. No problems were encountered using the water squirter in this orientation and water flow rate. When the water squirter was used with its water column oriented horizontally, it was noted that the exit water did not remain collimated and interference of the RF signal was observed. To collimate the water beam in a horizontal orientation, a jet of water was needed, which required a water pump, which in the end resulted in a typical water squirter with a water flow rate of 0.8 gal/min (3.0 l/min). The introduction of the water pump also brought up another problem not present in the gravity feed experiment. The pumping action aerated the water and small bubbles formed inside the water squirter housing and on the face of the transducer. The design of the squirter did not allow for a means to clear these bubbles away once they formed on the transducer face. Once present, the bubbles interfered with the sound beam and rendered the squirter useless. Debubbled water (water that has remained still for an extended period of time) helped to slow the growth of the bubble formations; however the bubbles always came back eventually. From this came the realization that two things must be done to reliably use the low frequency technique with a water delivery system. First and most importantly, bubbles must not be allowed to accumulate on the transducer face and second, the water flow rate should be reduced. The simplest manner to accomplish the first objective is to enclose the transducer, much like a captured water column. Enclosing the transducer prevents bubbles from forming on the transducer face but at the same time it adds a reflection echo in the path of the sound beam. Captured water col-

umns are typically used in contact style inspections; however for our purposes the captured water column remains elevated above the sample surface to allowing it the captured water column to transverse over buttonhead rivets in a surface scan. If the captured water column is to remain elevated, then a pool of water must be maintained between the bottom of the captured water column and the sample surface. Maintaining a bubble free pool of water between the captured water column and the sample surface is relatively easy and does not require a great deal of water, hence the second objective of reducing the water flow was met.

The water squirter was modified to become a captured water column. The nozzle exit of the squirter was removed and covered with a thin layer of 3M Scotch™ tape. The surface of the tape layer, being flat, allows for removal of any air bubbles that might form on its surface during the scan. At this time the position of the interface echo and the focal location of the transducer coincided and a great deal of interference between the two was seen. With the addition of the tape layer in the beam path the overall amplitude of the RF signal was reduced by about 7 percent. The tape interface echo was 9 percent of the total signal amplitude when reflected from a reference Ti block. The interference effects were minimized by focusing the transducer past the membrane. It should be noted that some reduction in the overall signal amplitude will always remain. A plastic ring fashioned out of a 35 mm film container lid was attached around the squirter housing to maintain a pool of water between the captured water column and the sample surface. Water was gravity fed into the pool area using a 0.125 in (3.2 mm) diameter plastic tubing. The water flow rate was not measured, but it significantly reduced the amount of water needed to maintain a water path from the transducer to the sample surface compared to a squirter with a 0.25 in (6.4 mm) diameter opening. A gravity fed system worked well for both horizontal and vertical orientations; however a low pressure centrifugal force pump worked better and it did not require a reservoir of water to be maintained.

Although the water flow rate into the water pool was small, it was still great enough that all the excess water could not be mopped up by hand as a scan progressed. A vacuum attachment was devised which encircled the plastic ring that retained the water pool. The idea was that the plastic ring would keep the water pool intact and any excess water that leaked out of the water pool area would be removed by the surrounding vacuum ring. To achieve a retained water pool at the exit of the transducer, the flow into the water pool area had to be increased by around 20 percent.

2. Surface scans over flush mount riveted lap splices

With the addition of the vacuum attachment, all but one of the original objectives had been met and the first generation design of the Dripless Bubbler was complete. The Dripless Bubbler could now be used to scan over a flush mount riveted lap splices using a focused beam without uncontained water. The design was inexpensive and did not require a large amount of set up time. The system was thoroughly tested on a flush mount riveted lap splice in both vertical and up-side-down horizontal orientations. In Figure 4.1, the lap splice is oriented vertical and the Dripless Bubbler is oriented perpendicular to the sample surface. The C-scan image obtained with the setup shown in Fig. 4.1 using the overall amplitude of a 1 MHz pulse, is shown in Fig. 4.2a. Figure 4.2b shows a scan made of the same area made with the lap splice in an up-side-down horizontal orientation. The up-side-down horizontal orientation is characteristic of a scan made on the belly section of the aircraft. The lap splice sample was cut from an unserviceable Boeing 707. Although there are no known defects in this sample, it can be seen that the same details are revealed by both images regardless of the scanning orientation. The most important feature observed in Fig. 4.1 are the dry areas located above and below the damp contact strip along the current scan line. All water used for coupling the ultrasonic beam is retained within the plastic ring and no excess water exists during the scan. However, a problem was encountered at scanning locations near the lap edges. Along these locations a gap would form between the aluminum skins and the water retaining ring. When a gap formed, the water vacuum system would remove all the water from the retained water pool. This problem was eliminated by using a larger capacity adjustable output centrifugal pump and 3 additional water inlet tubes. At scan locations where the plastic ring was flush against the sample surface the output of the pump was decreased to the least amount needed to maintain a water pool at the sample surface. At locations where gaps could form between the water retaining ring and the sample surface, the output from the pump was adjusted to flood the water pool area faster than the vacuum return system could remove it away from the beam path. This arrangement required constant operator supervision and added an undesired complexity to the assembly. It was assumed at this time that this problem would be solved when the system was modified to allow for scanning over button head rivets.

3. Surface scans over raised surface features

Along with optimization of the captured water column housing and the membrane material selection (to be discussed later), one main objective remained — the ability to surface scan over raised surface features such as buttonhead rivets. The design became a trade off between sealing the water inside the water pool and/or controlling the suction action of the vacuum system. Efforts to control the vacuum suction always resulted with large amounts of

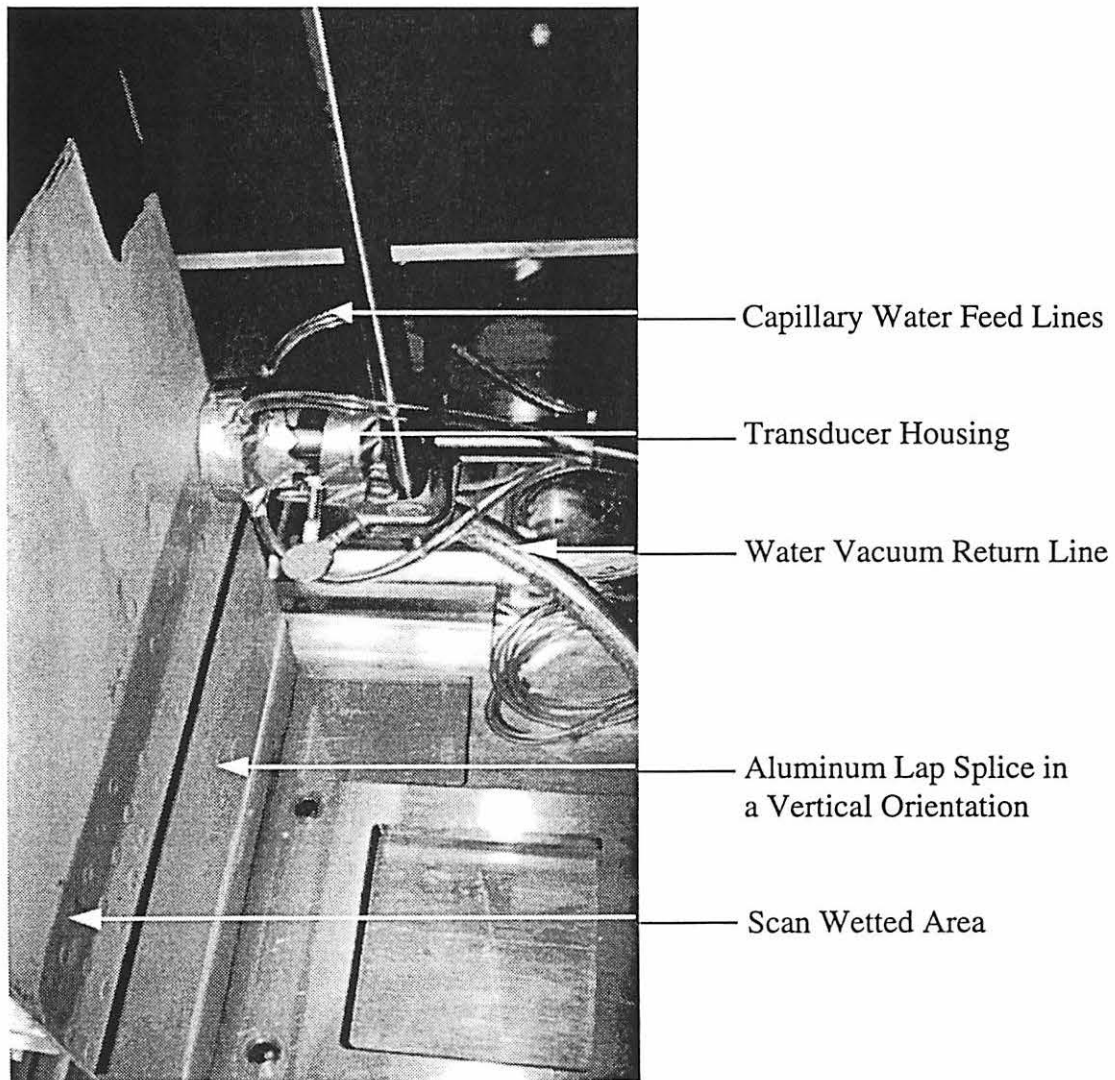
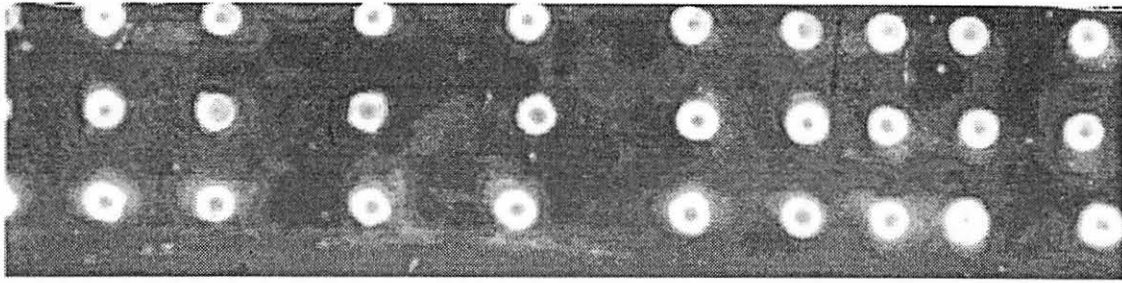
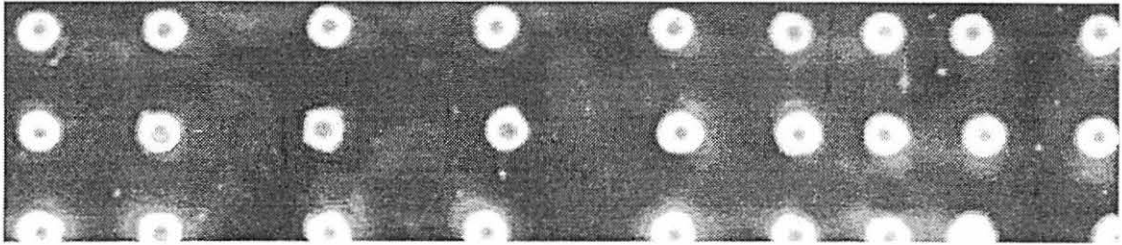


Figure 4.1: The first generation Dripless Bubbler scanning a flush-mount riveted aluminum lap splice in a vertical orientation. Shown are the water feed lines, the vacuum return line, and the scan wetted area.



(a)



(b)

Figure 4.2: C-scan images of a Boeing 707 lap splice sample with flush-mount rivets using the overall amplitude of a 1 MHz pulse with the Dripless Bubbler. (a) Scan made in a vertical orientation as depicted in Fig. 4.1. Scan area: 10.5 x 2.6 in (26.7 x 6.6 cm); step size: 10 mils (0.25 mm). (b) Scan made in an up-side-down orientation characteristic of an inspection made on the the belly section of an aircraft. Scan area: 9.7 x 2.1 in (24.6 x 5.3 cm); step size: 10 mils (0.25 mm).

water exiting the vacuum housing and running down the lap splice, so attention was directed toward sealing the water inside the water pool. The means to seal water in any orientation while being traversed over a surface with protrusions and indentations proved to be a formidable task. It was anticipated that scans over surface protrusions would gradually wear out any seal mechanism devised, thus the seal should be inexpensive and easy to replace. Several different seal mechanisms were formulated and tried; each worked in at least one scanning orientation or rivet configuration, but failing miserably in others. Through this early work two important points about the seal were noticed. First, the seal must be surface-conforming and be able to surround the surface protrusions and depressions at the same time. An example of a surface protrusion and depression combination are found where buttonhead rivets are installed along the lap splice edge. The second point noticed during the initial work is that the inlet to the pool of water must be sufficient to force out any air bubbles that may

enter into the water pool. Foam being both surface conforming and inexpensive, offered the greatest promise to both of these points. A 1.0 in (2.54 cm) thick, 20 density, oil resistant, polyurethane foam ring was attached to the bottom of the Dripless Bubbler and compressed slightly. As the foam ring was slid over buttonhead rivets it would conform around the rivets and fill out gaps along the lap splice edges. The disadvantage associated with foam as a water retaining mechanism is its porous nature. The vacuum sucked the water right through the cells of the foam. Closed cell foam would have prevented the vacuum from removing the water through the foam; however closed cell foam is generally more stiff and less surface-conforming compared to open cell foam. The simplest solution to this problem was to coat the inside of the foam ring with a silicone sealant, providing a barrier against the vacuum suction through the foam wall. The sealed foam ring was thoroughly tested on several rivet configurations and lap splice orientations and found to perform satisfactorily in all cases. At this time, all original design objectives had been met. The prototype Dripless Bubbler was inexpensive, allowed for focused beam inspection, and surface scans over buttonhead rivets on aircraft fuselage lap splices in any orientation. A schematic of the Dripless Bubbler prototype is shown in Fig. 4.3.

C. Dripless Bubbler Membrane Material

The membrane material, at the exit of the captured water column, serves two purposes. First, the membrane allows ultrasonic energy to pass through it. It should be as acoustically transparent as possible to minimize any reflection echoes from it. Second, the membrane should allow for a repeatable, water-tight seal and be durable enough for continued use. Three low density membrane materials were tested as a possible exit membrane: polyvinylidenechloride (plastic food wrap), polyvinylfluoride (window heat shrink) and latex rubber (latex condom). These three materials were readily available, easy to use, and obtain, but more importantly, inexpensive to replace. The effectiveness of the membranes were tested using the same 1 MHz transducer originally designed with the Dripless Bubbler. All three membranes satisfactorily sealed the captured water column.

Acoustic transparency of the membrane material was examined by considering the ratio of the membrane reflection echo amplitude and the overall 1 MHz pulse RF signal amplitude with a membrane material in the beam's path to the overall RF signal amplitude in immersion without a membrane in the beam's path. The results of which are shown in Table 4.1 and Fig. 4.4.

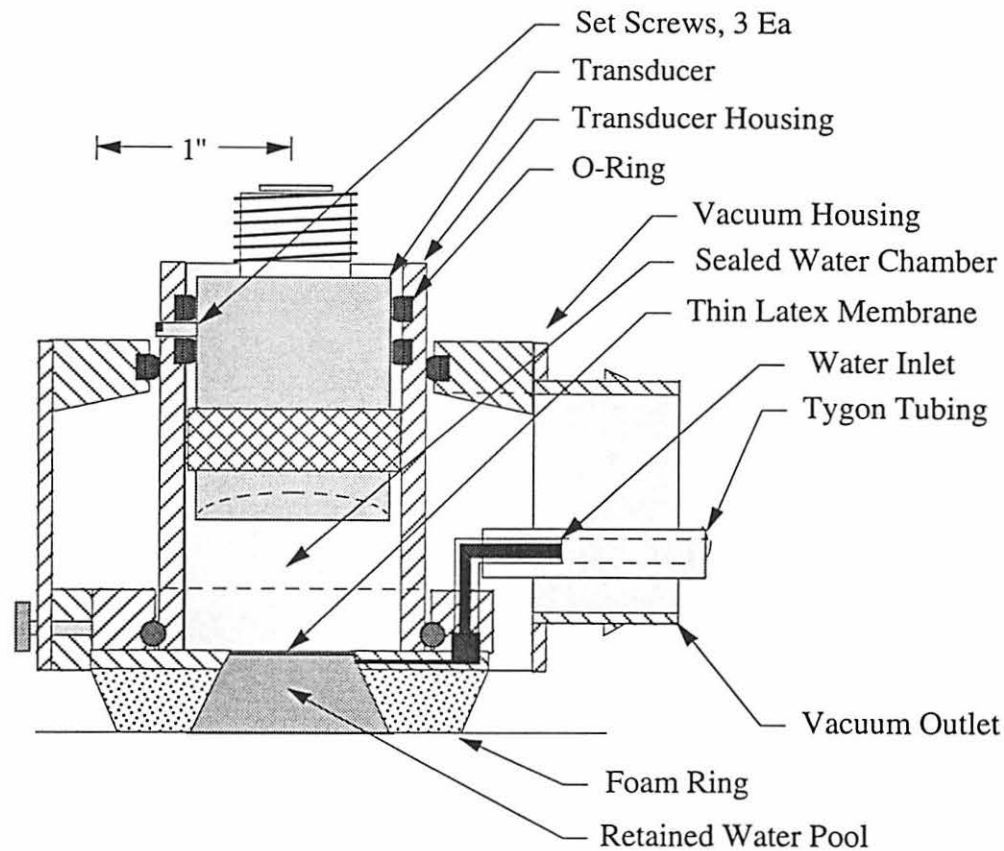


Figure 4.3: Schematic view of the Dripless Bubbler.

The plastic food wrap results are a little misleading. The plastic food wrap was stretched over the transducer housing in the usual fashion. The interference caused by the plastic food wrap became a function of how tight the film was stretched. It was extremely difficult to obtain a repeatable tension in the plastic food wrap. The plastic food wrap could not maintain its tension over a period of two days and hence its reflection echo amplitude changed with time.

The plastic heat shrink always maintained a uniform tension using a heat gun at the same temperature, heating time, and separation distance. Wrinkles in the plastic film did form around the edges of the heat shrink and often times trapped air in the wrinkles would be released into the captured water column during the Dripless Bubbler's use. The heat shrink material did sag (stretch) after four days of use, but the plastic heat shrink could be retightened with the captured water in place. A consistent tension upon retightening could not be obtained and it was often times easier to reinstall a new membrane.

Table 4.1: Acoustic transparency of three membranes using a 1MHz broadband RF pulse

Membrane Material	Reflection Echo Amplitude (% Immersion)	Overall Signal Amplitude (% Immersion)
Plastic Food Wrap	3 ± 2	4 ± 2
Plastic Heat Shrink	7 ± 2	3 ± 2
Latex Condom	3 ± 1	1 ± 1

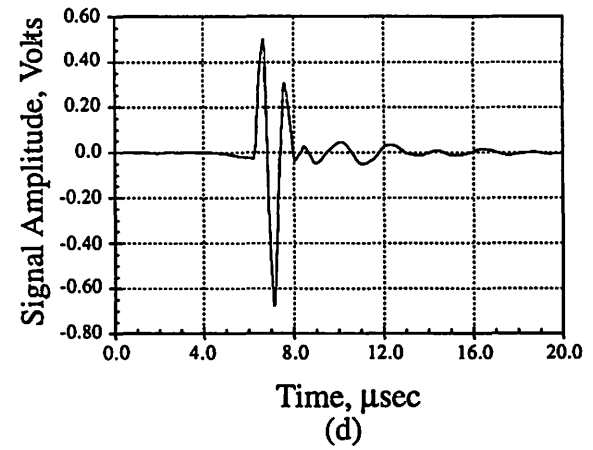
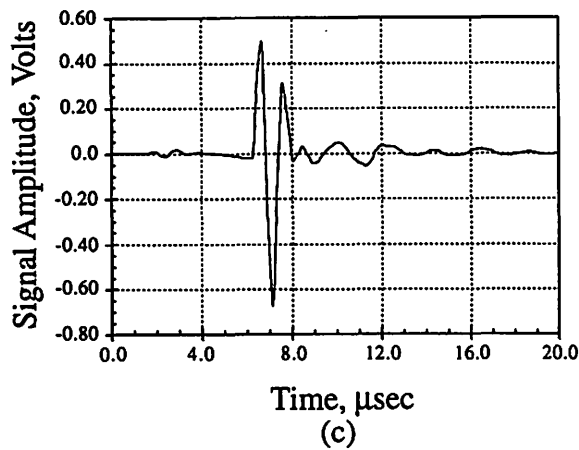
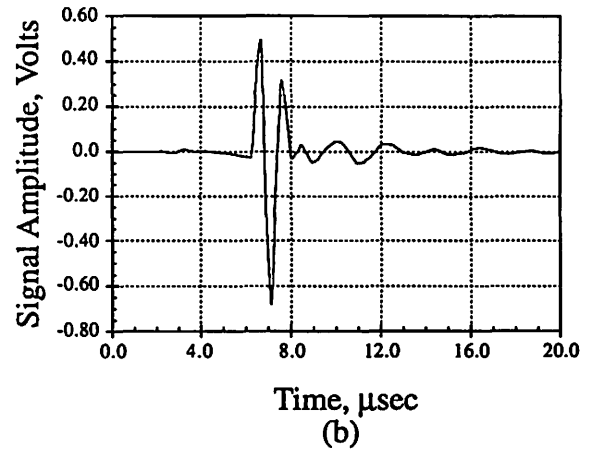
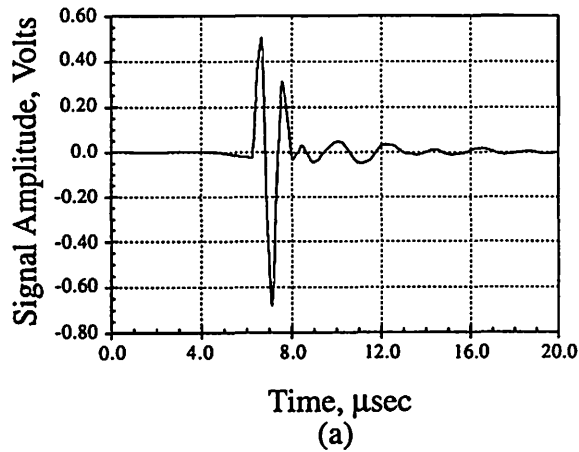


Figure 4.4: 1 MHz RF pulses reflected from a reference titanium block. Membranes positioned in the beam path, located 3 mm above the surface of the titanium block. (a) No membrane. (b) Plastic food wrap. (c) Plastic heat shrink. (d) Latex condom.

The latex condom did not require any maintenance, even four weeks after installation. The Dripless Bubbler is designed to be operated over buttonhead rivets. If the Dripless Bubbler is placed over a single button rivet so that the rivet head presses against the exit membrane, only the latex condom could recover from pressure applied against it. The plastic food wrap always broke and the heat shrink material required retightening. The best overall performance as an exit membrane was obtained with the latex condom. Lubricated condoms did not fare as well as unlubricated condoms and the talcum powder must be removed from the condom before installation to ensure a repeatable acoustic transparency.

D. Using the Dripless Bubbler

After the initial success of scanning the small Boeing 707 panel samples in different orientations, the Dripless Bubbler design was improved and then tried on a more realistic sample. Scans were made on a 10 x 6 ft (3.0 x 1.8 m) Foster-Miller test panel with the Dripless Bubbler attached to a computer controlled portable handscanner [56,57]. The Foster-Miller panel is designed to simulate a fuselage section of a Boeing 727 or 737 and is complete with all support ribs and stringers. Shown in Fig. 4.5 is the Dripless Bubbler attached onto the Foster-Miller panel mounted on the end of a x-y hand scan position en-

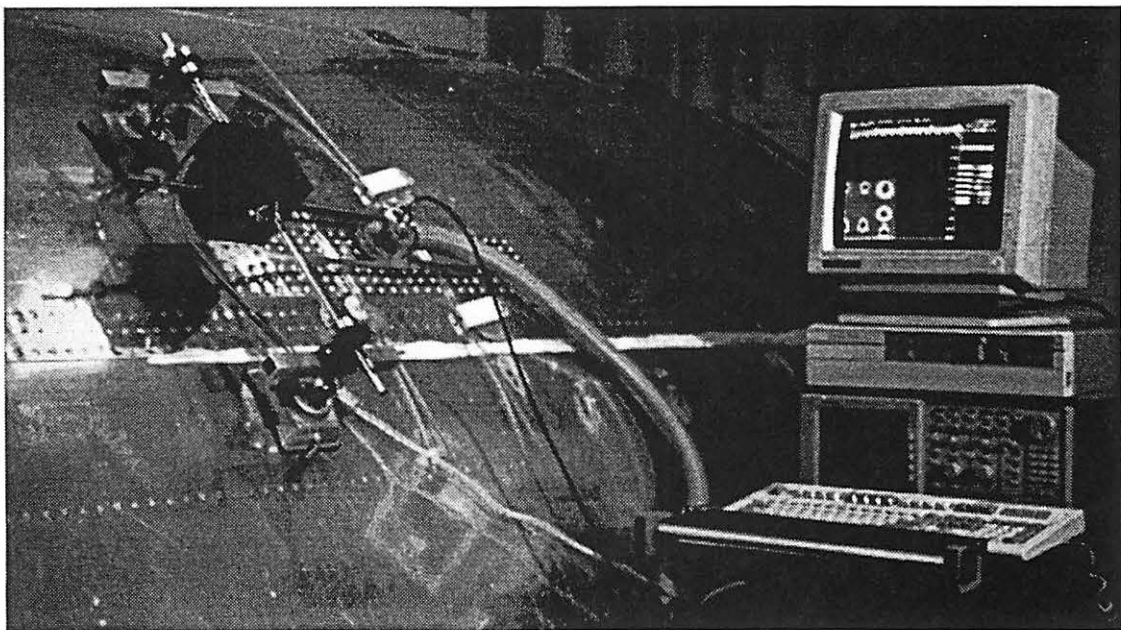


Figure 4.5: The Dripless Bubbler mounted at the end of an x-y handscanner and attached to the Foster-Miller panel.

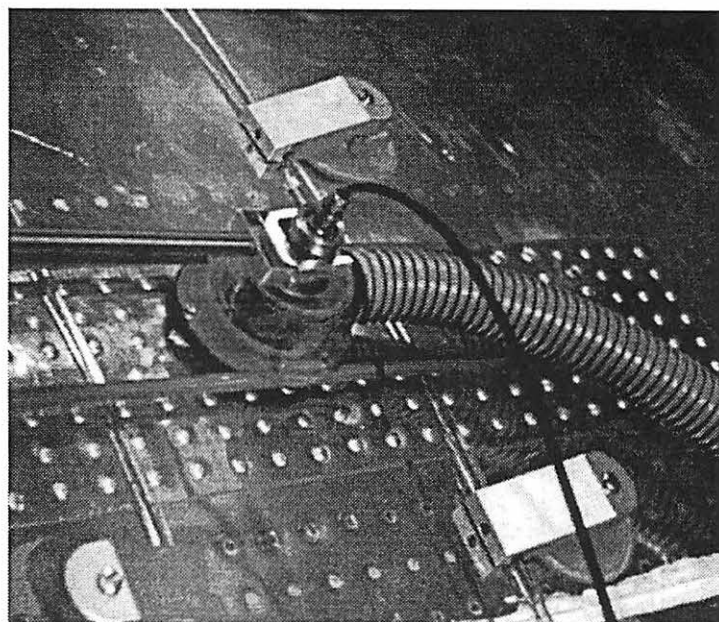


Figure 4.6: Close-up view of the Dripless Bubbler mounted at the end of an x-y handscanner. Seen are the guide rails used to provide a smooth scan motion and maintain a constant height above the sample surface.

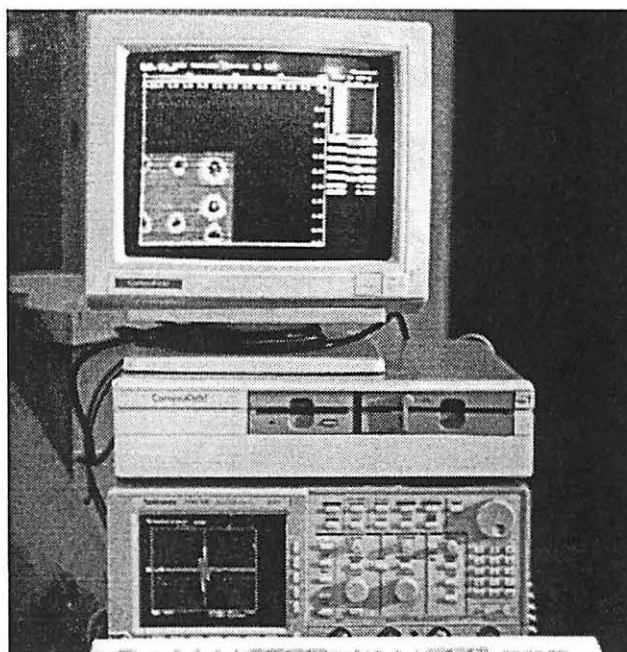


Figure 4.7: Close-up view of a hand scan image displayed on the portable computer and a RF signal displayed on an oscilloscope.

coder. Figures 4.6 and 4.7 are close-up views of the Dripless Bubbler and the computer setup respectively. To facilitate a smooth scan motion and to prevent side-to-side tilting of the Dripless Bubbler, two guide rails were attached to the Foster-Miller panel and two cross members were attached to the Dripless Bubbler. This arrangement maintains a perpendicular orientation with respect to the lap splice, and more importantly, it maintains a constant height of the transducer above the skin panel.

C-scan images made with the arrangement shown in Fig. 4.5 on flush mount and button head rivets are shown in Figs. 4.8 and 4.9 respectively. Figure 4.8 is a 8.0 x 4.0 in (20.3 x 10.2 cm) C-scan image of a lap splice with flush mount rivets. The scan took 10 minutes using a position encoder step size of 50 mils (1.3 mm). The C-scan image shown in Fig. 4.9 is a 4.5 x 6.5 in (11.4 x 16.5 cm) button head repair patch. The button head rivet scan took 25 minutes using the same position encoder step size as that used for the flush mount rivets. Any surface features other than smooth aluminum skin does slow down the scanning motion. The scanned sections are not known to contain artificial flaws, but the scan images did show some mechanical features of the panel. The horizontal strip located in the center row of rivets in Fig. 4.8 is the support stringer located behind the second aluminum skin.

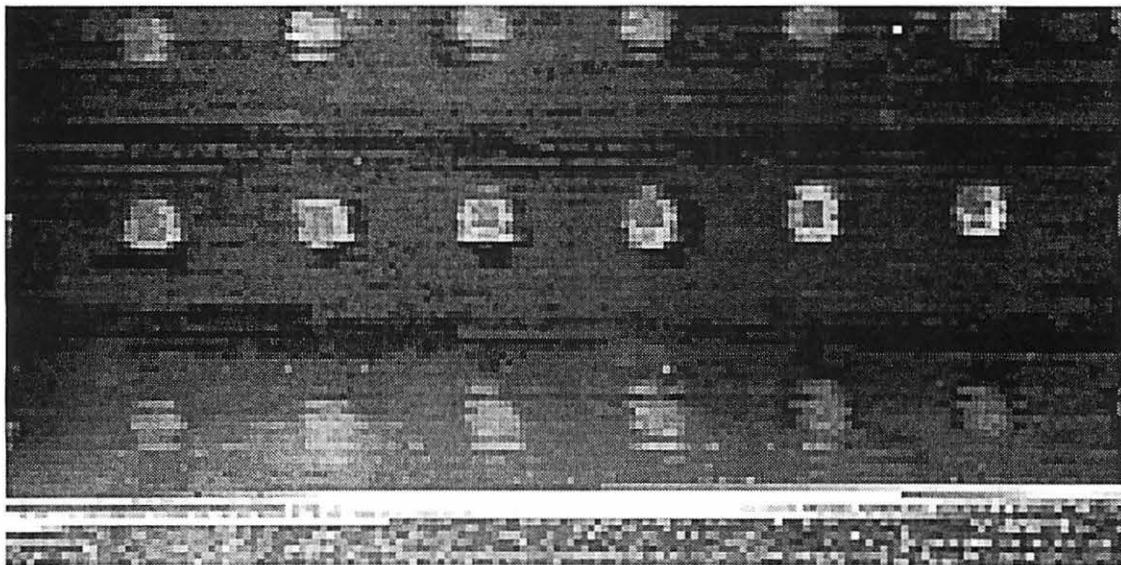


Figure 4.8: Hand scanned C-scan image of a lap splice with flush mount rivets using the overall amplitude of a 1 MHz pulse. Scan area: 8.0 in x 4.0 in (20.3 x 10.2 cm); step size: 50 mils (1.3 mm); scan time: 10 minutes.

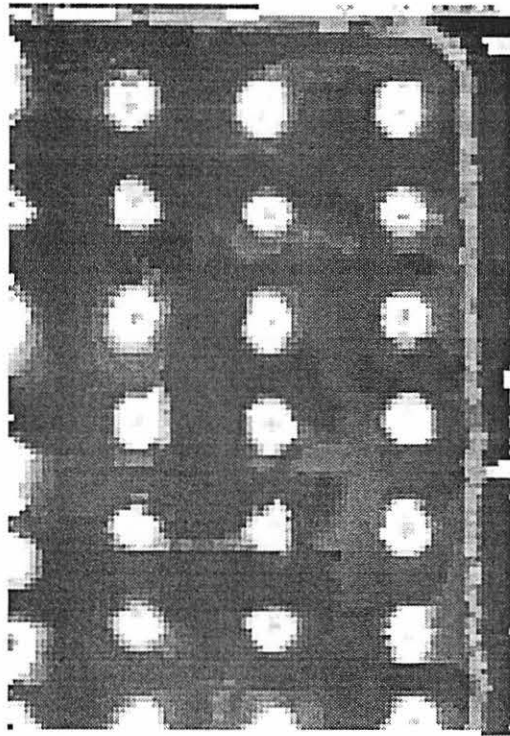


Figure 4.9: Hand scanned C-scan image of a repair patch with button head rivets using the overall amplitude of a 1 MHz pulse. Scan area: 4.5 x 6.5 in (11.4 x 16.5 cm); step size: 50 mils (1.3 mm); scan time: 25 minutes.

CHAPTER V. CONCLUSIONS

The advantages of the low frequency inspection technique are its ability to detect disbond and second layer corrosion defects in adhesive lap splices using only the peak amplitude of the reflected RF signal. The technique lends itself to fast area scanning of aircraft fuselage lap splices. Images acquired using a low frequency broadband transducer are relatively free of misleading information and hence they are easier to interpret than images produced using a higher frequency broadband transducer. The disadvantages of the method are its lack of depth information and the lower image contrast. However, the low image contrast is improved with simple image enhancement methods.

It has been successfully demonstrated, with the aid of a Dripless Bubbler, that the low frequency inspection technique can be applied for the inspection of aircraft fuselage lap splices. The Dripless Bubbler is a self-contained, water-coupled device that allows for ultrasonic, focused-beam immersion inspection in areas where uncontained water is not desirable. Being a self-contained unit, it can therefore be used in any inspection orientation, including upside-down. The Dripless Bubbler itself can accommodate standard commercial focused beam immersion transducers, of any center frequency, with element diameters of 0.5 in (1.27 cm) and 0.75 in (1.91 cm) and focal lengths from 0.75 to 3.0 in (1.91 to 7.62 cm). C-scan images of the fuselage are possible with the Dripless Bubbler attached to a portable hand scan system.

Together, the low frequency inspection technique and the Dripless Bubbler provide the airline maintenance community with a simple and reliable ultrasonic inspection system that can be applied for the inspection of aircraft fuselage lap splices. Additional experience with the low frequency inspection technique and the modifications to the Dripless Bubbler will allow for a more reliable ultrasonic inspection method.

A. The Low Frequency Inspection Technique

The low frequency inspection technique, as a technique itself, can be improved through continued experience with realistic fuselage lap splices. It is anticipated that further research will offer the ability to distinguish unresolved ultrasonic echoes that are reflected from a disbond and/or corroded surface. The ability to discriminate between RF signals reflected from disbond and corroded surfaces will involve more elaborate analysis of the reflecting RF signal. Additional analysis of the reflecting RF signal must be balanced against the benefits

associated with the low frequency inspection technique, namely its acquisition speed. The trailing portion of the RF signal, though unresolved, does contain information regarding the entire lap splice. This was shown by the low frequency inspection technique's ability to detect second layer metal thinning due to corrosion. Additional work should be directed at determining if the trailing portion of the reflected RF signal can discriminate between disbond and/or corroded surfaces.

B. The Dripless Bubbler

Up to this point, the design of the Dripless Bubbler has been oriented toward producing one working prototype to allow for a focused beam, ultrasonic inspection of the exterior surface of an aircraft fuselage. The Dripless Bubbler is *not* an optimized design. It was designed to serve a single purpose using available materials and support services. The Dripless Bubbler was machined out of Lexan plastic. Lexan is durable, and it allows one to observe the operation of the Dripless Bubbler. The Dripless Bubbler can be fabricated out of any light weight plastic material. It is conceivable that the Dripless Bubbler can be manufactured in two subassemblies using a plastic injection molding process. Such a process is unavailable at ISU.

The hardware store quality wet/dry vacuum cleaner attached to the Dripless Bubbler was the least expensive available. Even though the vacuum was inexpensive, its suction power was found to be sufficient. The purpose of the wooden box that surrounds the vacuum cleaner is to reduce the noise exposure to the operator. In a maintenance hanger environment the wooden box surrounding the vacuum cleaner may not be necessary, however in small laboratory rooms, where the Dripless Bubbler was developed, it is a necessity. The wooden enclosure reduces the average exposure noise, at the 3 ft (0.91 m) away from the vacuum, from 90 dB to 70 dB.

There are two centrifugal water pumps that supply water to the Dripless Bubbler. One pump is submersible, located inside the wet/dry vacuum cleaner. The other pump is attached to the exterior of the wooden box. Neither pump performs perfectly; however both were available at no cost. The submersible pump can not vertically pump water through a 0.125 in (3.2 mm) ID hose any higher than 4 ft (1.2 m), while the exterior pump can vertically pump water through a 0.125 in (3.2 mm) ID tube up to 15 ft (4.6 m). The exterior pump is ideal for operations where the Dripless Bubbler is positioned on a maintenance platform and the

vacuum/pump assembly is located on the ground. The submersible pump is used to prime the exterior pump.

The vacuum/pump assembly can be combined in a configuration similar to that found in ordinary wet/dry carpet cleaners. The noise can be reduced by insulating the vacuum electric motor, or operating the vacuum with compressed air. A design study should be conducted to determine the optimum mix of inlet water into the contained water pool and the vacuum suction required to remove the excess water exiting the contained water pool, versus different surface conditions and inspection heights.

Images produced with the low frequency inspection technique and the Dripless Bubbler are made with a manual hand scan system. It is unrealistic to assume that ultrasonics will be used to inspect the entire fuselage for lap splice defects. Preliminary inspections should be made using another NDI technique such as thermal wave and electronic speckle pattern interferometry. These techniques can inspect large areas of the fuselage at once, but suffer from poor defect resolution. After questionable areas of the fuselage are located, they can be scanned again using ultrasonics. If an inspection procedure such as this is followed, it is unnecessary to automate the scan action of the Dripless Bubbler. It is very tedious to scan large areas with a hand scanner, but not impossible. The benefits of a hand scanner are two fold. First, the operator has more control over the scan process should an air bubble become trapped in the retained water pool. A motorized scanner would continue following an x-y grid regardless of the ultrasonic signal and the scan would have to be restarted from scratch. With a hand scan system, the operator simply scans over the area again with minimal loss of inspection time. Furthermore, attaching a motorized unit onto the Dripless Bubbler increases the weight, complexity, and cost of the assembly and does not guarantee a higher quality inspection. As of today, the Dripless Bubbler uses guide rails attached to the fuselage with suction cups. If a motorized unit was attached to the Dripless Bubbler, vacuum suction cups would be required to compensate for the additional weight. As far as the scanning method is concerned, it is the opinion of the author that a hand scan system should be used and the guide rails should be replaced with a linear bearing mechanism that can traverse over slightly curved surfaces.

REFERENCES

- [1] C. Seher, and A. L. Broz, "National research program for nondestructive inspection of aging aircraft." Materials Evaluation, December 1991, pp. 1547-1550.
- [2] Advertising brochure: Federal Aviation Administration -- Center for Aviation Systems Reliability, Institute for Physical Research and Technology, Iowa State University, Ames, IA, 1991.
- [3] A. S. Brown, "Seeing beneath the surface with NDE: new non-invasive testing techniques hold key to future aging aircraft." Aerospace American, May 1992, pp. 26-30, 40.
- [4] Aircraft accident report: NTSB/AAR-90/01, National Transportation Safety Board, Washington, D. C., 1990.
- [5] N. D. Kristoff, "Jet crashes in China, killing 141; 5th serious accident in 4 months. (China southern airlines Boeing 737 crash highlights maintenance and air-traffic control inadequacies)." The New York Times, November 25, 1992, v. 142, pp. A6.
- [6] S. N. Bobo, "The aging aircraft fleet: A challenge for nondestructive inspection." Review of progress in quantitative nondestructive evaluation, v. 9, ed. by D. O. Thompson and D. E. Chimenti, Plenum Press, New York, NY, 1990, pp. 2097-2109.
- [7] W. F. Harrington, "The seven deadly sins of adhesive bonding." Adhesive Age, May 31, 1992, v. 35, pp. 6-7.
- [8] T. J. Reinhart, "Structural bonding needs for aerospace vehicles." Adhesive Age, January 31, 1989, v. 32, pp. 26-28.
- [9] H. Holmquist, Boeing Company Commercial Airplane Group: Boeing Customer Support NDI Group, Seattle, WA, private correspondence, August 22, 1991.
- [10] "This is the FAA: mission, organization, and activity." United States: Federal Aviation Administration, Washington, D. C., July 1992.
- [11] D. C. Dilworth, "Airlines won't disclose safety problems voluntarily." Trial, September 1992, pp. 106.
- [12] J. Doetkott, Northwest Airlines, Minneapolis, MN, private correspondence, January 23, 1992.
- [13] C. Gifford, Boeing Company Commercial Airplane Group: Boeing Customer Support NDI Group, Seattle, WA, private correspondence, February 11, 1991.

- [14] F. Gott, "Bondtester applications: using the MIA-2500 bondtester." Staveley Instruments, Inc., Kennewick, WA, February, 1991.
- [15] D. J. Hagemaiier, "Nondestructive testing developments in the aircraft industry." Materials Evaluation, December 1991, pp. 1470-1478.
- [16] S. Mitra, P. S. Urali, E. Uzal, J. H. Rose, and J. C. Moulder, "Eddy-current measurements of corrosion-related thinning in aluminum lap splices." Review of progress in quantitative nondestructive evaluation, v. 12, ed. by. D. O. Thompson and D. E. Chimenti, Plenum Press, New York, NY, 1993, pp. 2003-2010.
- [17] G. M. Light and H. Kwun, "Nondestructive evaluation of adhesive bond quality: state of the art review." SwRI Project 17-7958, Southwest Research Institute, San Antonio, TX, June 1989.
- [18] C. C. H. Guyott, P. Cawley, and R. D. Adams, "The nondestructive testing of adhesively bonded structures: a review." Journal of Adhesion, v. 20, 1986, pp. 129-159.
- [19] G. P. Anderson, J. S. Bennett, and L. K. DeVries, Analysis and testing of adhesive bonds. Academic Press, New York, NY, 1977.
- [20] Transcripts of the proceedings of the "Workshop on NDE of adhesive bond strength." organized by the Nondestructive Testing Information Center, San Antonio, TX, April 13-14, 1988.
- [21] E. A. Llyod and A. F. Brown, "Recent developments in nondestructive testing of adhesive-bonded joints." Adhesion II, ed. by K. W. Allen, Applied Science Publishers Ltd., London, England, 1978, pp. 133-144.
- [22] G. Schmitz and L. Frank, "NDT evaluation of the strength of bonded materials." NASA contractor report CR-67983, September 1966.
- [23] E. Segal and J. L. Rose, "Nondestructive testing techniques for adhesive bond joints." Research techniques in nondestructive testing, v. 4, ed. by R. S. Sharpe, Academic Press, New York, NY, 1980, pp. 275-316.
- [24] D. J. Hagemaiier, "Bonded joints and non-destructive testing: bonded honeycomb structures - 1." Nondestructive Testing, v. 4, 1971, pp. 401.
- [25] "Nondestructive testing of adhesive bonds: special issue." Journal of Adhesion Science and Technology, v. 5, (8), ed. by K. L. Mittal and W. J. van Ooij, 1991, pp. 579-690.

- [26] "AGARD: Impact of emerging NDE-NDI methods on aircraft design, manufacture and maintenance." papers presented at the 69th meeting of the Structural and Materials Panel in Brussels, Belgium, October 1-6, 1989.
- [27] Military standardization handbook: adhesive bonding: MIL-HDBK-691B, U. S. Department of Defense, Washington, D. C., 1987.
- [28] H. Koski and G. L. Schneberger, "Testing adhesives: thoroughness helps make sound decisions." Adhesive Age, May 31, 1984, pp. 8-12.
- [29] G. Alers, P. L. Flynn, and J. J. Buckley, "Ultrasonic techniques for measuring the strength of adhesive bonds." Materials Evaluation, April 1977, pp. 77-84.
- [30] P. A. Dickstein, J. K. Spelt, and A. N. Sinclair, "Investigation of nondestructive monitoring of the environmental degradation of structural adhesive joints." Materials Evaluation, December 1991, pp. 1498-1505.
- [31] R. Prakash, V. K. Srivastava, and G. S. R. Gupta, "Behavior of adhesive joints in corrosive environment." Experimental Mechanics, v. 27, December 1987, pp. 346-351.
- [32] P. A. Meyer and J. L. Rose, "Ultrasonic determination of bond strength due to surface preparation variations in aluminum to aluminum adhesive bond system." Journal of Adhesion, August 1976, pp. 145-153.
- [33] G. A. Alers and R. K. Elsley, "Measurement of metal to adhesive bond quality using digital signal analysis." 1977 Ultrasonic symposium proceedings, IEEE catalogue No. 77CH1264-1SU, New York, NY, 1977.
- [34] J. L. Rose and G. H. Thomas, "The Fisher linear discriminant function for adhesive bond strength prediction." British Journal of Nondestructive testing, v. 21, (3), May 1979, pp. 135-139.
- [35] J. H. Gieske, "Manual scanning with automated data acquisition and display of eddy current and ultrasonic signals for aging aircraft NDI applications." AANC project proposal, Sandia National Laboratories, Albuquerque, NM, November 1992.
- [36] NDI Department: Northwest Airlines, United Airlines, American Airlines, USAir, Delta Airlines, private correspondence, December 27, 1991.
- [37] A. S. Birks, R. E. Green Jr., and P. McIntire, Ultrasonic testing: nondestructive testing handbook, 2nd ed., v. 7, American Society for Nondestructive Testing publication, Columbus, OH, 1991.
- [38] J. Krautkrämer and H. Krautkrämer, Ultrasonic testing of materials, 4th ed., Springer-Verlag, Berlin, 1990.

- [39] W. Niblack, An introduction to digital image processing, Prentice-Hall International, Englewood Cliffs, NJ, 1986.
- [40] D. K. Hsu and V. Dayal, "Ultrasonic Newton's Rings." *Applied Physics Letter*, v. 60 (11), 1992, pp. 1169-1171.
- [41] M. N. Abedin, P. H. Johnston, and D. R. Prabhu, "Disbond detection using peak amplitude of pulse-echo signals for various thicknesses and transducer frequencies." Review of progress in quantitative nondestructive evaluation, v. 12, ed. by D. O. Thompson and D. E. Chimenti, Plenum Press, New York, NY, 1993, pp. 1539-1546.
- [42] D. K. Hsu, M. S. Hughes, and T. C. Patton, "Ultrasonic scans using low frequency unresolved echoes." Review of progress in quantitative nondestructive evaluation, v. 12, ed. by D. O. Thompson and D. E. Chimenti, Plenum Press, New York, NY, 1993, pp. 1595-1602.
- [43] Progress report: Federal Aviation Administration - Center for Aviation Systems Reliability, project 1, task 1, subtask B, Ames, IA, March 1992, pp. 5-10.
- [44] Boeing Company Commercial Airplane Group: BAC - 5514, Seattle, WA, revised November 1985, pp. 14-16.
- [45] "Standard methods of analysis of sulfochromate etch solution used in surface preparation of aluminum." ASTM D 2674 -72, Annual book of ASTM standards, Philadelphia, PA, 1984.
- [46] T. C. Patton and D. K. Hsu, "Fabrication procedures for aluminum/adhesive lap splices containing simulated second layer corrosion defects." FAA Technote, December 1992.
- [47] H. Aglan, L. Kennebrew, D. K. Hsu, and T. C. Patton, "Correlation of NDE parameters with lifetime of aircraft adhesive bonds." Review of progress in quantitative nondestructive evaluation, v. 12, ed. by D. O. Thompson and D. E. Chimenti, Plenum Press, New York, NY, 1993, pp. 1611-1618.
- [48] D. J. Hagemmaier and A. H. Wendelbo Jr., and Y. Bar-Cohen, "Aircraft corrosion and detection methods." Douglas paper 7510, presented to QUALTEST-3 Cincinnati, OH, Oct. 1984.
- [49] H. Leidheiser, Jr. and W. Wang, "Corrosion control by organic coatings." National Association of Corrosion Engineers publication, Houston, TX, 1981.
- [50] Corrosion aluminum skin samples provided courtesy of Northwest Airlines, Minneapolis, MN.

- [51] "Ultrasonic transducers for nondestructive testing." Panametrics product catalog, P393, Waltham, PA, April 93, pp. 2-3.
- [52] B. P. Newberry, "Experimental evaluation of Gaussian and Gaussian-Hermite beam theories as tools for modeling scanned ultrasonic measurements." M. S. Thesis, Iowa State University, 1985.
- [53] L. M. Brekhovskikh, Waves in layered media, Academic Press, New York, 1960., pp. 45-70.
- [54] G. M. Light, R. A. Cervantes, and D. P. Harvey, "Development of a pulse-echo ultrasonic squirter for detection of first layer delamination in composite structures." Review of progress in quantitative nondestructive evaluation, v. 7, ed. by D. O. Thompson and D. E. Chimenti, Plenum Press, New York, NY, 1988, pp. 929-936.
- [55] C. F. Buynak and R. L. Crane, "A novel acoustic coupling device using permeable membrane." Materials Evaluation, June 1987, pp. 743-746.
- [56] SONIX Inc.: FlexSCAN-H ultrasonic hand scan system.
- [57] Infometrics: TestPro imaging system, Transonic Inc.: hand scan system.

ACKNOWLEDGMENTS

I would like to acknowledge the support of several individuals that made this research possible. From Northwest Airlines in Minneapolis, MN, I would like to thank Mr. Jeff Register and Mr. Jerry Doetkott for providing several corroded aluminum skin samples, and the "fist-hand" tour of their maintenance operations. From the Boeing Company Commercial Airplane Customer Support NDI Group in Seattle, WA, I would like to thank Mr. Michael Hutchinson for the two "blind" first layer corrosion samples he provided. I would like to thank Dr. Heshmat Aglan and his students from Tuskegee University in Tuskegee, AL for their contributions in mechanical testing. I would like to thank my Major Professor, Dr. David K. Hsu, and the other members of the examining committee for their guidance, encouragement and patience shown by them during this research. I would also like to thank the research and support staff at the Center for Nondestructive Evaluation and the Center for Aviation Systems Reliability who each in their own way made this research enjoyable. Lastly, I would like to thank my wife Brenda and my son Jesse for their support and understanding during my undergraduate and graduate study at Iowa State University.

This work was sponsored by the FAA-Center for Aviation Systems Reliability, operated by Iowa State University for the Federal Aviation Administration under Grant No. 93-G-018, and operated by the Ames Laboratory, U. S. Department of Energy, for the Federal Aviation Administration under Contract No. W-7405-eng-82 with Iowa State University. The United States government has assigned the DOE report number IS-T-1681 to this thesis.

APPENDIX

Reflection Coefficient -- FORTRAN code

```

c234567890....+....2....+....3....+....4....+....5....+....6....+....7..
c
c Written for FAA Adhesive Bond Project by Thadd C. Patton
c
c Last modified 8/10/93 by Thadd C. Patton
c
c-----
c  Subroutines:
c
c input      Input Parameters
c fft        Power of 2, Fast Fourier Transform
c reflct     Calculates reflection coefficient vs frequency
c spear      Performs time domain correlation
c-----
c  Output Files:
c
c Time header: Index, Time, Real, Imaginary
c Frequency header: Index, Frequency, Real, Imaginary, Magnitude
c
c Out/ref_t.dat      Input RF waveform vs time
c Out/ref_f.dat      FFT of Input RF waveform vs frequency
c Out/rcoef_f.dat     Reflection coefficient vs frequency
c Out/rcoef_t.dat     Reflection coefficient vs time
c Out/conv_f.dat      Convolution results vs frequency
c Out/conv_t.dat      Convolution results vs time
c-----
c  Nomenclature:
c
c Integers:
c
c mxlay      maximum number of layers
c mxpts      maximum number of data points for zero padding
c npts       number of input points
c nlayer     number of layers
c itmp       output control of 2**14 points
c istep      step size necessary to control output to 2**14
c iref       input cosine function waveform flag
c ihead      head output flag
c iout       data file output flag
c igate      time gate peak analysis flag
c irf        compare RF waveform flag
c istart     index start
c iend       index end
c i,j        index counters
c-----
c Reals:

```

```

c
c twopi      2 * pi
c tpoint     time per sample point
c fstart     center frequency of generated RF waveform
c dfreq      frequency per point
c time       time index in usec
c f          frequency index in MHz
c r_mag      magnitude
c r_real     real component
c r_imag     imaginary component
c dir        FFT / IFFT flag
c tconv      single precision time domain convolution results
c tsmpl      single precision sample RF waveform
c ds         sum squared of ranks
c rs         correlation coefficient
c zd         standard deviations
c probd      significance of deviations
c probrs     significance of coefficient
c tsrt       time start
c tend       time end
c pkmax      temporary max peak
c pkmin      temporary min peak
c peak       peak to peak
c pmax       max peak
c-----
c Real Arrays:
c
c d          layer thickness
c rho        layer mass density
c c          layer longitudinal velocity
c z          layer impedance ( c(i) * rho(i))
c r          interface reflection coefficient
c atn        layer attenuation coefficient
c treal      real component of RF waveform
c timag      imaginary component of RF waveform
c tsmpl      real component of sample RF waveform
c freal      real component of RF waveform FFT
c fimag      imaginary component of RF waveform FFT
c rfreal     real component of reflection coefficient
c rfimag     imaginary component of reflection coefficient
c greal      real component of reflection coefficient & FFT convolution
c gimag      imaginary component of reflection coefficient & FFT convolution
c tmp1,2     temporary arrays
c-----
c Complex Arrays:
c
c rcoef      complex array of calculated reflection coefficient vs frequency
c-----
c Others:
c
c title      character input title

```

```

c ctab          character Mac tab output format
c-----
c
  program main5
  implicit real*8(a-h, o-z)
  implicit integer(i-n)
  complex*8 rcoef
  real tsmpl, tconv, tmp1, tmp2, rs, ds, zd, probd, probrs
  character*80 title
  parameter(mxlay=5, mxpts=2**18)
  dimension d(0:mxlay), rho(0:mxlay), c(0:mxlay), z(0:mxlay),
&          r(0:mxlay), atn(0:mxlay), treal(mxpts),
&          timag(mxpts), freal(mxpts), fimag(mxpts),
&          rcoef(mxpts), rfreal(mxpts), rfimag(mxpts),
&          greal(mxpts), gimag(mxpts), tsmpl(mxpts),
&          tconv(mxpts), tmp1(mxpts), tmp2(mxpts), iout(6)
  common/picon/twopi
  common/para/tpoint, fstart, npts, nptsf, dfreq, nlayer
  common/iflag/iref, ihead, iout, igate, irf
  common/char/title
c
c... Mac tab output character
c
  ctab = char(9)
c
c... calculate pi constants
c
  twopi = 8.0d0 * datan(1.0d0)
c
c... input material properties and reference wave
c
  call input(treal, timag, tsmpl, d, rho, c, z, atn,
&          mxpts, mxlay)
c
c... output control up to 2**14 points by varying the step size
c
  itmp = nptsf / 16384
  istep = max(1,itmp)
c
c... output original reference waveform
c
  if(iout(1) .eq. 1) then
    open(9, file = 'Out/ref_t.dat', status = 'unknown')
    if(ihead .eq. 1) then
      write(9,9000) 'Index', ctab, 'Time', ctab, 'Real'
    end if
    do 10 j = 1, npts
      time = dble(j-1) * tpoint
      write(9,9010) j, ctab, time, ctab, treal(j)
10  continue
    close(9)

```

```

    end if
c
c... pad time domain input with zeros
c
    do 20 j = npts+1, nptsf
        treal(j) = 0.0d0
        timag(j) = 0.0d0
20 continue
c
c... calculate the frequency components of the reference wave form
c
    dir = -1.0d0
    call fft(treal, timag, freal, fimag, nptsf, dir)
c
c... reference waveform frequency parameters
c
    dfreq = 1.0d0 / (dble(nptsf) * tpoint)
    if(iout(2) .eq. 1) then
        open(10, file = 'Out/ref_f.dat', status = 'unknown')
        if(ihead .eq. 1) then
            write(10,9000) 'Index', ctab, 'Freq', ctab, 'Real',
&                ctab, 'Imag', ctab, 'Magnitude'
        end if
        do 40 j = 1, nptsf/2+1, istep
            f = dble(j-1) * dfreq
            r_mag = dsqrt(freal(j)*freal(j) + fimag(j)*fimag(j))
            write(10,9010) j, ctab, f, ctab, freal(j), ctab,
&                fimag(j), ctab, r_mag
40 continue
        close(10)
    end if
c
c... calculate R-coef
c
    call reflct(d, rho, c, z, atn, r, rcoef, mxpts, mxlay)
c
c... R-Coef frequency data
c
    if(iout(3) .eq. 1) then
        open(12, file = 'Out/rcoef_f.dat', status = 'unknown')
        if(ihead .eq. 1) then
            write(12,9000) 'Index', ctab, 'Freq', ctab, 'Real',
&                ctab, 'Imag', ctab, 'Magnitude'
        end if
        do 50 j = 1, nptsf/2+1, istep
            f = dble(j-1) * dfreq
            r_real = real(rcoef(j))
            r_imag = aimag(rcoef(j))
            r_mag = cabs(rcoef(j))
            write(12,9010) j, ctab, f, ctab, r_real, ctab, r_imag,
&                ctab, r_mag
50 continue
        close(12)
    end if

```

```

50  continue
    close(12)
  end if
c
c... convolution F(w) and R(w) to obtain G(w)
c
  do 60 j = 1, nptsf
    rfreal(j) = real(rcoef(j))
    rfimag(j) = aimag(rcoef(j))
    greal(j) = rfreal(j) * freal(j) - rfimag(j) * fimag(j)
    gimag(j) = rfreal(j) * fimag(j) + rfimag(j) * freal(j)
60  continue
c
c... inverse Fourier transform R-Coef back to the time domain, r(t)
c
  dir = 1.0d0
  call fft(rfreal, rfimag, treal, timag, nptsf, dir)
  if(iout(4) .eq. 1) then
    open(14, file = 'Out/rcoef_t.dat', status = 'unknown')
    if(ihead .eq. 1) then
      write(14,9000) 'Index', ctab, 'Time', ctab, 'Real',
&                  ctab, 'Imag'
    end if
    do 70 j = 1, npts
      time = dble(j-1) * tpoint
      write(14,9010) j, ctab, time, ctab, treal(j) ,ctab,
&                  timag(j)
70  continue
    close(14)
  end if
c
c... frequency components of G(w)
c
  if(iout(5) .eq. 1) then
    open(16, file = 'Out/conv_f.dat', status = 'unknown')
    if(ihead .eq. 1) then
      write(16,9000) 'Index', ctab, 'Freq', ctab, 'Real',
&                  ctab, 'Imag', ctab, 'Magnitude'
    end if
    do 90 j = 1, nptsf/2+1, istep
      f = dble(j-1) * dfreq
      r_mag = dsqrt(greal(j)*greal(j) + gimag(j)*gimag(j))
      write(16,9010) j, ctab, f, ctab, greal(j) ,ctab,
&                  gimag(j), ctab, r_mag
90  continue
    close(16)
  end if
c
c... inverse convolution G(w) results back to the time domain, g(t)
c
  dir = 1.0d0

```

```

call fft(greal, gimag, treal, timag, nptsf, dir)
if(iout(6) .eq. 1) then
  open(18, file = 'Out/conv_t.dat', status = 'unknown')
  if(ihead .eq. 1) then
    write(18,9000) 'Index', ctab, 'Time', ctab, 'Real',
    &          ctab, 'Imag'
  end if
  do 100 j = 1, npts
    time = dble(j-1) * tpoint
    write(18,9010) j, ctab, time, ctab, treal(j), ctab,
    &          timag(j)
100  continue
  close(18)
end if
if(irf .eq. 1) then
c
c... Time domain correlation analysis
c
  do 105 j = 1, npts
    tconv(j) = real(treal(j))
105  continue
  call spear(tconv, tsmpl, tmp1, tmp2, rs, zd, ds, probd,
  &          probrs, npts)
  write(6,9020) 'Correlation Coefficient.....'
  &..', rs
  write(6,9020) 'Standard Deviations.....'
  &..', zd
  write(6,9020) 'Sum Squared Difference of Ranks.....'
  &..', ds
  write(6,9020) 'Significance Level of Deviation.....'
  &..', probd
  write(6,9020) 'Significance Level Coefficient.....'
  &..', probrs
  write(6,9000)
end if
if(igate .eq. 1) then
c
c... time gate analysis
c
110  write(6,9000) 'Enter the [stating, ending] gate index'
  write(6,9000) 'To quit enter start gate *****>[-99,anynumber]'
  write(6,9000)
  read(5,*) istart, iend
  if(istart .lt. 0) goto 130
  if(iend .lt. istart) then
    write(6,9000) 'Start gate index [<=] End gate index'
    write(6,9000)
    goto 110
  end if
  if(istart .eq. 0) then
    istart = 1

```

```

        write(6,9000) 'Start gate index changed --> 1'
    end if
    if(iend .gt. npts) then
        iend = npts
        write(6,9030) 'End gate index changed --> ', npts
    end if
    tstart = istart * tpoint
    tend = iend * tpoint
    pkmax = -1.0d+04
    pkmin = 1.0d+04
c
c... Max amplitude calculations
c
    do 120 j = istart, iend
        trial = treal(j)
        pkmin = dmin1(pkmin,trial)
        pkmax = dmax1(pkmax,trial)
120    continue
        peak = pkmax - pkmin
        pmax = dmax1(pkmax, dabs(pkmin))
        write(6,9000)
        write(6,9020) 'Time Gates [usec]:' , tstart, ' ---> ', tend
        write(6,9020) 'Max Peak Signal Amplitude .....
&..', pkmax
        write(6,9020) 'Min Peak Signal Amplitude .....
&..', pkmin
        write(6,9020) 'Peak-to-Peak Signal Amplitude .....
&..', peak
        write(6,9020) 'Peak Signal Amplitude .....
&..', pmax
        write(6,9000)
        goto 110
    end if
c-----
9000  format(a,4(a1,a))
9010  format(i9,4(a1,e13.6))
9020  format(5x,2(a,1pe12.5))
9030  format(a,i5)
c-----
130  stop
    end
c234567890....+....2....+....3....+....4....+....5....+....6....+....7..
c
c Copied from W. H. Press, et al, "Numerical recipe's:
c the art of scientific computing." Cambridge University
c Press, New York, NY, 1988, pp.488-491
c
    FUNCTION BETACF(A,B,X)
    PARAMETER (ITMAX=100,EPS=3.E-7)
    AM=1.
    BM=1.

```

```

AZ=1.
QAB=A+B
QAP=A+1.
QAM=A-1.
BZ=1.-QAB*X/QAP
DO 11 M=1,ITMAX
  EM=M
  TEM=EM+EM
  D=EM*(B-M)*X/((QAM+TEM)*(A+TEM))
  AP=AZ+D*AM
  BP=BZ+D*BM
  D=-(A+EM)*(QAB+EM)*X/((A+TEM)*(QAP+TEM))
  APP=AP+D*AZ
  BPP=BP+D*BZ
  AOLD=AZ
  AM=AP/BPP
  BM=BP/BPP
  AZ=APP/BPP
  BZ=1.
  IF(ABS(AZ-AOLD).LT.EPS*ABS(AZ)) GO TO 1
11 CONTINUE
1  BETACF=AZ
  RETURN
END
c234567890....+....2....+....3....+....4....+....5....+....6....+....7..
c
c Copied from W. H. Press, et all, "Numerical recipe's:
c the art of scientific computing." Cambridge University
c Press, New York, NY, 1988, pp.488-491
c
FUNCTION BETAI(A,B,X)
IF(X.LT.0..OR.X.GT.1.)PAUSE 'bad argument X in BETAI'
IF(X.EQ.0..OR.X.EQ.1.)THEN
  BT=0.
ELSE
  BT=EXP(GAMMLN(A+B)-GAMMLN(A)-GAMMLN(B)
*   +A*ALOG(X)+B*ALOG(1.-X))
ENDIF
IF(X.LT.(A+1.)/(A+B+2.))THEN
  BETAI=BT*BETACF(A,B,X)/A
  RETURN
ELSE
  BETAI=1.-BT*BETACF(B,A,1.-X)/B
  RETURN
ENDIF
END
c234567890....+....2....+....3....+....4....+....5....+....6....+....7..
c
c Copied from W. H. Press, et all, "Numerical recipe's:
c the art of scientific computing." Cambridge University
c Press, New York, NY, 1988, pp.488-491

```


c234567890....+....2....+....3....+....4....+....5....+....6....+....7..

```

c Modified from a C program written by Dr. Michael Hughes
c Center for NDE, Ames, IA, 1991.
c
  subroutine fft(rein, xmin, reout, ximout, n, dir)
  implicit real*8(a-h, o-z)
  implicit integer(i-n)
  dimension rein(0:n-1), xmin(0:n-1), reout(0:n-1),
&          ximout(0:n-1), s(0:31), c(0:31)
  data (s(i), i = 0, 31)
& /0.00000000000000000000000000000040, 1.00000000000000000000000000000000,
&   0.70710678118654752400, 0.38268343236508977120,
&   0.19509032201612826700, 0.09801714032956060220,
&   0.04906767432741801440, 0.02454122852291228800,
&   0.01227153828571992610, 0.00613588464915447540,
&   0.00306795676296597630, 0.00153398018628476560,
&   0.00076699031874270450, 0.00038349518757139560,
&   0.00019174759731070330, 0.00009587379909597730,
&   0.00004793689960306690, 0.00002396844980841820,
&   0.00001198422490506970, 0.00000599211245264240,
&   0.00000299605622633470, 0.00000149802811316900,
&   0.00000074901405658470, 0.00000037450702829240,
&   0.00000018725351414620, 0.00000009362675707310,

```

```

& 0.000000004681337853650, 0.000000002340668926830,
& 0.000000001170334463410, 0.000000000585167231710,
& 0.000000000292583615850, 0.000000000146291807930/
data (c(i), i = 0, 31)
& /-1.00000000000000000000, 0.000000000000000000020,
& 0.70710678118654752480, 0.92387953251128675630,
& 0.98078528040323044930, 0.99518472667219688610,
& 0.99879545620517239290, 0.99969881869620421990,
& 0.99992470183914454090, 0.99998117528260114210,
& 0.99999529380957617150, 0.99999882345170190990,
& 0.99999970586288221910, 0.99999992646571785130,
& 0.99999998161642929390, 0.99999999540410731290,
& 0.99999999885102682750, 0.99999999971275670690,
& 0.99999999992818917670, 0.99999999998204729410,
& 0.9999999999551182350, 0.9999999999887795590,
& 0.9999999999971948890, 0.9999999999992987210,
& 0.9999999999998246810, 0.9999999999999561710,
& 0.99999999999999890430, 0.9999999999999972610,
& 0.9999999999999993150, 0.9999999999999998290,
& 0.999999999999999570, 0.999999999999999890/
c
ie = int(log(dble(n)) / log(2.0d0))
nby2 = n / 2
nmin1 = n - 1
j = 0
do 10 i = 0, n-1
  reout(i) = rein(i)
  ximout(i) = ximin(i)
10 continue
do 20 i = 0, nmin1-1
  if(i .lt. j) then
    retmp = reout(j)
    ximtmp = ximout(j)
    reout(j) = reout(i)
    ximout(j) = ximout(i)
    reout(i) = retmp
    ximout(i) = ximtmp
  end if
  k = nby2
  itmp = j - k
  if(itmp .lt. 0) goto 15
  do while(k .le. j)
    j = j - k
    k = k / 2
  end do
15  j = j + k
20 continue
do 60 l = 0, ie-1
  ib = 1
  do 30 j = 0, 1
    ib = ib * 2

```

```

30  continue
    ic = ib / 2
    u = 1.0d0
    d = 0.0d0
    y = c(l)
    f = -1.0 * dir * s(l)
    do 50 j = 0, ic-1
        do 40 i = j, n-2, ib
            ig = i + ic
            t = u * reout(ig) - d * ximout(ig)
            ds = d * reout(ig) + u * ximout(ig)
            reout(ig) = reout(i) - t
            ximout(ig) = ximout(i) - ds
            reout(i) = reout(i) + t
            ximout(i) = ximout(i) + ds
40  continue
    x = u * y - d * f
    w = u * f + d * y
    u = x
    d = w
50  continue
60  continue
    x = 1.0d0 / dsqrt(dble(n))
    do 70 i = 0, n-1
        reout(i) = reout(i) * x
        ximout(i) = ximout(i) * x
70  continue
    return
end
c234567890....+....2....+....3....+....4....+....5....+....6....+....7..
c
c Written for FAA Adhesive Bond Project by Thadd C. Patton
c
c Last modified 4/22/93 by Thadd C. Patton
c
c-----
c  Subroutines:
c
c refwav      Cosine generated input RF waveform
c-----
c  Sample Input File:
c
c Adhesive lap-splice with glass beads in Squirter mode
c 1           reference wave (actual=1,simulated=0)
c 11          number of points in reference wave form [2**m]
c 16          number of zero padded points [max = 2**18]
c 0.01        time per point [usec]
c 1.0         center frequency of simulated input wave [MHz]
c 0           time gate Peak-to-Peak analysis (1=yes,0=no)
c 4.500, 0.6040 reference halfspace [density, velocity]
c 0.0         reference halfspace data attenuation control [dB]

```

```

c 1          compare results with sample RF (1=yes,0=no)
c 3          total number of layers (not halfspaces)
c 7.6200, 1.000, 0.1490, 0.0000    top halfspace [d0] (water path)
c 0.2430, 2.320, 0.5790, 0.0000    top Glass layer, [d1]
c 0.0260, 1.100, 0.2000, 0.0000    adhesive layer [d2]
c 0.2430, 2.320, 0.5790, 0.0000    top Glass layer, [d3]
c 7.6200, 1.000, 0.1490, 0.0000    top halfspace [d0] (water)
c 1          output a column header (1=yes,0=no)
c 0          output f(t) in Mac-tab format (1=yes,0=no)
c 0          output F(w) in Mac-tab format (1=yes,0=no)
c 0          output R(w) in Mac-tab format (1=yes,0=no)
c 0          output r(t) in Mac-tab format (1=yes,0=no)
c 0          output G(W) in Mac-tab format (1=yes,0=no)
c 1          output g(t) in Mac-tab format (1=yes,0=no)
c-----
c  Nomenclature:
c
c Integers:
c
c mxlay      maximum number of layers
c mxpts      maximum number of data points for zero padding
c npts       number of input points
c nlayer     number of layers
c itmp       output control of 2**14 points
c istep      step size necessary to control output to 2**14
c iref       input cosine function waveform flag
c ihead      head output flag
c iout       data file output flag
c igate      time gate peak analysis flag
c irf        compare RF waveform flag
c lenb#      character length of base#
c m#         power of two exponent
c i,j        index counters
c-----
c Reals:
c
c twopi      2 * pi
c tpoint     time per sample point
c fstart     center frequency of generated RF waveform
c dfreq      frequency per point
c time       time index in usec
c zc         reference halfspace acoustic impedance
c rhalf      reference halfspace reflection coefficient
c rdb        input RF gain control waveform
c tsmpl      single precision sample RF waveform
c-----
c Real Arrays:
c
c d          layer thickness
c rho        layer mass density
c c          layer longitudinal velocity

```

```

c z          layer acoustic impedance ( c(i) * rho(i))
c r          interface reflection coefficient
c atn        layer attenuation coefficient
c treal      real component of RF waveform
c timag      imaginary component of RF waveform
c tsmpl      real component of sample RF waveform
c-----
c Others:
c
c title      character input title
c base#      character input file name
c lfile      logical flag
c-----
c
c      subroutine input(treal, timag, tsmpl, d, rho, c, z, atn,
&      mxpts, mxlay)
c      implicit real*8 (a-h, o-z)
c      implicit integer(i-n)
c      real tsmpl
c      character*80 title
c      character*30 base1, base2, base3
c      logical lfile
c      dimension d(0:mxlay), rho(0:mxlay), c(0:mxlay), z(0:mxlay),
&      atn(0:mxlay), treal(mxpts), timag(mxpts),
&      tsmpl(mxpts), iout(6)
c      common/picon/twopi
c      common/para/tpoint, fstart, npts, nptsf, dfreq, nlayer
c      common/iflag/iref, ihead, iout, igate, irf
c      common/char/title
c
c... read in material parameter data
c
5  write(6,9045) ' '
c      write(6,9045) 'Enter the material input file name
& [30 char max]'
c      read(5,9060) lenb1, base1(1:lenb1)
c      write(6,9045) ' '
c      inquire(file = base1(1:lenb1), exist = lfile)
c      if(.not. lfile) then
c          write(6,9045) ' '
c          write(6,9045) '*****> Notice <*****'
c          write(6,9045) 'Input file >',base1(1:lenb1),'< does NOT
& exist !!!'
c          write(6,9045) 'Try again'
c          goto 5
c      end if
c      open(10, file = base1(1:lenb1), status = 'old')
c
c... title
c
c      read(10,9000) title

```

```

c
c... reference wave (actual=1,simulated=0)
c
  read(10,*) iref
c
c... number of points in reference wave form [2**m]
c
  read(10,*) m1
c
c... number of zero padded points [max = 2**18]
c
  read(10,*) m2
c
c... time per point [usec]
c
  read(10,*) tpoint
c
c... center frequency of simulated input wave [MHz]
c
  read(10,*) fstart
c
c... time gate Peak-to-Peak analysis (1=yes,0=no)
c
  read(10,*) igate
c
c... reference halfspace density and velocity
c
  read(10,*) rrho, rc
  zc = rrho * rc
c
c... reference halfspace data attenuation control [dB]
c
  read(10,*) rdb
  if(rdb .eq. 0.0d0) then
    rdb = 1.0d0
  else
    rdb = dlog10(20.0d0 / rdb)
  end if
c
c... compare results with sample RF waveform
c
  read(10,*) irf
c
c... total number of layers (not halfspaces)
c
  read(10,*) nlayer
c
c... layer thickness[cm], density[gm/cm^3], velocity[cm/usec],
c... attenuation loss [1/cm]
c
  do 10 i = 0, nlayer+1

```

```

        read(10,*) d(i), rho(i), c(i), atn(i)
        z(i) = rho(i) * c(i)
10  continue
c
c... output a column header (1=yes,0=no)
c
    read(10,*) ihead
c
c... output files in Mac-tab format (1=yes,0=no)
c... f(t), F(w) R(w) r(t), G(W), g(t)
c
    do 15 i = 1, 6
        read(10,*) iout(i)
15  continue
    close(10)
c
c... number of points exponentials
c
    npts = 2**m1
    nptsf = 2**m2
c
c... read in generated reference data and RF waveform
c
    if (iref .eq. 0) then
        call refwav(treal, timag, mxpts)
    else
25  write(6,9045) ' '
        write(6,9045) 'Enter the reference halfspace input file name
& [30 char max]'
        read(5,9060) lenb2, base2(1:lenb2)
        write(6,9045) ' '
        inquire(file = base2(1:lenb2), exist = lfile)
        if(.not. lfile) then
            write(6,9045) ' '
            write(6,9045) '*****> Notice <*****'
            write(6,9045) 'Input file >',base2(1:lenb2),'< does NOT
& exist !!!'
            write(6,9045) 'Try again'
            goto 25
        end if
        open(11, file = base2(1:lenb2), status = 'old')
c
c... reference halfspace reflection coefficient
c
    rhalf = (zc -z(0)) / (zc + z(0))
c
c... input halfspace reference RF waveform
c
    read(11,9065)
    do 30 j = 1, npts
        read(11,*) tmp

```

```

        treal(j) = rdb * tmp / rhalf
        timag(j) = 0.0d0
30    continue
        close(11)
    end if
c
c... read in sample RF waveform
c
    if (irf .eq. 1) then
35    write(6,9045) ' '
        write(6,9045) 'Enter the sample RF waveform input file name
& [30 char max]'
        read(5,9060) lenb3, base3(1:lenb3)
        write(6,9045) ' '
        inquire(file = base3(1:lenb3), exist = lfile)
        if(.not. lfile) then
            write(6,9045) ' '
            write(6,9045) '*****> Notice <*****'
            write(6,9045) 'Input file >',base3(1:lenb3), '< does NOT
& exist !!!'
            write(6,9045) 'Try again'
            goto 35
        end if
        open(12, file = base3(1:lenb3), status = 'old')
c
c... input halfspace reference wave
c
        read(12,9065)
        do 40 j = 1, npts
            read(12,*) tsmpl(j)
40    continue
        close(12)
    end if
c
c... echo print input parameters
c
        write(6,9010) title
        if (iref .eq. 0) then
            write(6,9040) 'Reference Halfspace Parameters'
& , '(Generated Reference Wave)'
        else
            write(6,9040) 'Reference Halfspace Parameters'
& , '(Actual Experimental Wave)'
        endif
        write(6,9015) 'Transducer to Sample Distance [cm] ..... '
& , d(0)
        write(6,9015) 'Mass density [g/cm^3] ..... '
& , rho
        write(6,9015) 'Longitudinal velocity [cm/usec] ..... '
& , rc
        write(6,9015) 'Transducer Center Frequency [MHz] ..... '

```



```

&, fstart
write(6,9020) 'Input Time Domain Range'
write(6,9005) 'Number of sample points ..... '
&, npts
write(6,9005) 'Input sample points padded to ..... '
&, nptsf
write(6,9015) 'Time per point [usec] ..... '
&, tpoint
c
write(6,9030) 'Layered Media Parameters'
write(6,9045) '..... Top Halfspace'
write(6,9015) 'Mass density [g/cm^3] ..... '
&, rho(0)
write(6,9015) 'Longitudinal velocity [cm/usec] ..... '
&, c(0)
write(6,9015) 'Attenuation Coefficient [1/cm] ..... '
&, atn(0)
do 50 i = 1, nlayer
write(6,9005) '..... Layer #', i
write(6,9015) 'Thickness [cm] ..... '
&, d(i)
write(6,9015) 'Mass density [g/cm^3] ..... '
&, rho(i)
write(6,9015) 'Longitudinal velocity [cm/usec] ..... '
&, c(i)
write(6,9015) 'Attenuation Coefficient [1/cm] ..... '
&, atn(i)
50 continue
write(6,9045) '..... Bottom Halfspace'
write(6,9015) 'Mass density [g/cm^3] ..... '
&, rho(nlayer+1)
write(6,9015) 'Longitudinal velocity [cm/usec] ..... '
&, c(nlayer+1)
write(6,9015) 'Attenuation Coefficient [1/cm] ..... '
&, atn(nlayer+1)
write(6,9035) 'Program Generated Data Files [Mac-tab format]'
if(ihead .eq. 1) then
write(6,9045) ' ***> Output column header included. <***'
end if
write(6,9045) '....[Index...Increment...Real Part...Imag Part...
&Magnitude]....'
write(6,9045) ' '
if(iout(1) .eq. 1) then
write(6,9045) 'Input halfspace reference wave ..... '
&, ' Out/ref_t.dat'
end if
if(iout(2) .eq. 1) then
write(6,9045) 'FFT parameters of input reference wave ..... '
&, ' Out/ref_f.dat'
end if
if(iout(3) .eq. 1) then

```

```

        write(6,9045) 'Reflection coefficient parameters R=R(f,d) ....'
        &, ' Out/rcoef_f.dat'
        end if
        if(iout(4) .eq. 1) then
            write(6,9045) 'Reflection coefficient parameters R=R(t,d) ....'
            &, ' Out/rcoef_t.dat'
            end if
            if(iout(5) .eq. 1) then
                write(6,9045) 'Frequency domain convolution results .....'
                &, ' Out/conv_f.dat'
                end if
                if(iout(6) .eq. 1) then
                    write(6,9045) 'Time domain convolution results .....'
                    &, ' Out/conv_t.dat'
                    end if
                    write(6,9045) ' '
                    write(6,9045) 'Please wait ...'
                    write(6,9045) ' '
c
c-----
9000  format(a80)
9005  format(5x,a,i9)
9010  format(/,5x,a80)
9015  format(5x,a,1pe12.5)
9020  format(/,15x,a,/,15x,23('-'),/)
9030  format(/,15x,a,/,15x,24('-'),/)
9035  format(/,10x,a,/,10x,45('-'),/)
9040  format(/,15x,a,/,15x,a,/,15x,30('-'),/)
9045  format(5x,3(a))
9060  format(q,a)
9065  format(/)
c-----
        return
        end
c234567890....+....2....+....3....+....4....+....5....+....6....+....7..
c
c Written for FAA Adhesive Bond Project by Thadd C. Patton
c
c Last modified 10/22/93 by Thadd C. Patton
cc-----
c  Nomenclature:
c
c Integers:
c
c mxlay      maximum number of layers
c mxpts      maximum number of data points for zero padding
c npts       number of input points
c nlayer     number of layers
c ij         index counters
c-----
c Reals:

```

```

c
c twopi      2 * pi
c tpoint     time per sample point
c fstart     center frequency of generated RF waveform
c dfreq      frequency per point
c time       time index in usec
c delta      phase factor
c f          frequency index in MHz
c aloss      attenuation loss
c-----
c Real Arrays:
c
c d          layer thickness
c rho        layer mass density
c c          layer longitudinal velocity
c z          layer impedance ( c(i) * rho(i))
c r          interface reflection coefficient
c atn        layer attenuation coefficient
c-----
c Complex Arrays:
c
c rcoef      calculated reflection coefficient vs frequency
c ri         temporary
c e          exponential phase factor
c one        1.0
c-----
c
c
c      subroutine reflct(d, rho, c, z, atn, r, rcoef, mxpts, mxlay)
c      implicit real*8(a-h, o-z)
c      implicit integer(i-n)
c      complex*8 rcoef, ri, e, one
c      dimension d(0:mxlay), c(0:mxlay), z(0:mxlay), r(0:mxlay),
c      &          atn(0:mxlay), rcoef(mxpts)
c      common/picon/twopi
c      common/para/tpoint, fstart, npts, nptsf, dfreq, nlayer
c      one = cmplx(1.0d0,0.0d0)
c
c... individual layer reflection coefficients
c
c      do 5 i = 0, nlayer
c          r(i) = (z(i+1)-z(i)) / (z(i+1)+z(i))
c 5      continue
c
c... equivalent layer reflection coefficient method
c
c      do 15 j = 1, nptsf/2+1
c          f = dble(j-1) * dfreq
c
c... half space interfaces
c

```

```

        if(nlayer .eq. 0) then
            rcoef(j) = cmplx(r(0), 0.0d0)
        else
c
c... multiple layers
c
            rcoef(j) = cmplx(r(nlayer), 0.0d0)
            do 10 i = nlayer, 1, -1
                aloss = -1.0d0 * atn(i) * d(i) * dble(j) /
&                (tpoint * dble(nptsf))
                a = dexp(aloss)
                delta = 2.0d0 * d(i) * twopi * f / c(i)
                e = a * cmplx(dcos(delta), dsin(delta))
                ri = cmplx(r(i-1), 0.0d0)
                rcoef(j) = (ri + rcoef(j) * e) /
&                (one + ri * rcoef(j) * e)
10        continue
            end if
15 continue
c
c... symmetry about nptsf/2+1, (-1.0 * imaginary components)
c
            do 20 j = 1, nptsf/2
                rcoef(nptsf+1-j) = cmplx(real(rcoef(j+1)),
&                aimag(-1.0*rcoef(j+1)))
20 continue
c
c... set imaginary component of nptsf/2+1 = 0.0d0
c
            rcoef(nptsf/2+1) = cmplx(real(rcoef(nptsf/2+1)),0.0)
            return
        end
c234567890.....2.....3.....4.....5.....6.....7..
c
c Written for FAA Adhesive Bond Project by Thadd C. Patton
c
c Last modified 4/22/93 by Thadd C. Patton
c-----
c  Nomenclature:
c
c Integers:
c
c mxlay      maximum number of layers
c mxpts      maximum number of data points for zero padding
c npts       number of input points
c nlayer     number of layers
c i,j        index counters
c-----
c Reals:
c
c twopi      2 * pi

```

```

c tpoint      time per sample point
c fstart      center frequency of generated RF waveform
c dfreq       frequency per point
c time        time index in usec
c tdelay      time delay based upon input points
c temp        temporary
c-----
c Real Arrays:
c
c treal       real component of RF waveform
c timag       imaginary component of RF waveform
c-----
c
  subroutine refwav(treal, timag, mxpts)
    implicit real*8(a-h, o-z)
    implicit integer(i-n)
    dimension treal(mxpts), timag(mxpts)
    common/picon/twopi
    common/para/tpoint, fstart, npts, nptsf, dfreq, nlayer
c
c... generate a simulated input reference wave using a cosine function
c... frequency is MHz, time is in usec
c
    tdelay = dble(npts) / 1.0d+03
    do 10 j = 1, npts
      time = dble(j-1) * tpoint
      if(time .lt. tdelay) then
        treal(j) = 0.0d0
        timag(j) = 0.0d0
      else
        temp = twopi * fstart * (time-tdelay) / 3.0d0
        if (temp .le. twopi) then
          treal(j) = (1.0d0-dcos(temp))*dcos(temp*3.0d0)
          timag(j) = 0.0d0
        else
          treal(j) = 0.0d0
          timag(j) = 0.0d0
        end if
      end if
    10 continue
    return
    end
c234567890.....+....2....+....3....+....4....+....5....+....6....+....7..
c
c Copied from W. H. Press, et all, "Numerical recipe's:
c the art of scientific computing." Cambridge University
c Press, New York, NY, 1988, pp.488-491
c
  FUNCTION ERFCC(X)
    Z=ABS(X)
    T=1./(1.+0.5*Z)

```

```
ERFCC=T*EXP(-Z*Z-1.26551223+T*(1.00002368+T*(.37409196+
* T*(.09678418+T*(-.18628806+T*(.27886807+T*(-1.13520398+
* T*(1.48851587+T*(-.82215223+T*.17087277)))))))))
```

```
IF (X.LT.0.) ERFCC=2.-ERFCC
```

```
RETURN
```

```
END
```

```
c234567890.....2.....3.....4.....5.....6.....7..
```

c

c Copied from W. H. Press, et all, "Numerical recipe's:
c the art of scientific computing." Cambridge University
c Press, New York, NY, 1988, pp.488-491

c

```
FUNCTION GAMMLN(XX)
```

```
REAL COF(6),STP,HALF,ONE,FPF,X,TMP,SER
```

```
DATA COF,STP/76.18009173,-86.50532033,24.01409822,
```

```
* -1.231739516,.120858003E-2,-.536382E-5,2.50662827465/
```

```
DATA HALF,ONE,FPF/0.5,1.0,5.5/
```

```
X=XX-ONE
```

```
TMP=X+FPF
```

```
TMP=(X+HALF)*LOG(TMP)-TMP
```

```
SER=ONE
```

```
DO 11 J=1,6
```

```
  X=X+ONE
```

```
  SER=SER+COF(J)/X
```

```
11 CONTINUE
```

```
GAMMLN=TMP+LOG(STP*SER)
```

```
RETURN
```

```
END
```

```
c234567890.....2.....3.....4.....5.....6.....7..
```

c

c Copied from W. H. Press, et all, "Numerical recipe's:
c the art of scientific computing." Cambridge University
c Press, New York, NY, 1988, pp.488-491

c

```
SUBROUTINE SORT2(N,RA,RB)
```

```
DIMENSION RA(N),RB(N)
```

```
L=N/2+1
```

```
IR=N
```

```
10 CONTINUE
```

```
IF(L.GT.1)THEN
```

```
  L=L-1
```

```
  RRA=RA(L)
```

```
  RRB=RB(L)
```

```
ELSE
```

```
  RRA=RA(IR)
```

```
  RRB=RB(IR)
```

```
  RA(IR)=RA(1)
```

```
  RB(IR)=RB(1)
```

```
  IR=IR-1
```

```
  IF(IR.EQ.1)THEN
```

```
    RA(1)=RRA
```

```

        RB(1)=RRB
        RETURN
    ENDIF
ENDIF
I=L
J=L+L
20  IF(J.LE.IR)THEN
    IF(J.LT.IR)THEN
        IF(RA(J).LT.RA(J+1))J=J+1
    ENDIF
    IF(RRA.LT.RA(J))THEN
        RA(I)=RA(J)
        RB(I)=RB(J)
        I=J
        J=J+J
    ELSE
        J=IR+1
    ENDIF
    GO TO 20
ENDIF
RA(I)=RRA
RB(I)=RRB
GO TO 10
END

```

c234567890....+....2....+....3....+....4....+....5....+....6....+....7..

c

c Copied from W. H. Press, et all, "Numerical recipe's:
c the art of scientific computing." Cambridge University
c Press, New York, NY, 1988, pp.488-491

c

```

SUBROUTINE SPEAR(DATA1,DATA2,WKSP1,WKSP2,RS,ZD,D,
! PROBD,PROBRS,N)
DIMENSION DATA1(N),DATA2(N),WKSP1(N),WKSP2(N)
PARAMETER(TINY=1.0E-20)
DO 11 J=1,N
    WKSP1(J)=DATA1(J)
    WKSP2(J)=DATA2(J)
11  CONTINUE
CALL SORT2(N,WKSP1,WKSP2)
CALL CRANK(N,WKSP1,SF)
CALL SORT2(N,WKSP2,WKSP1)
CALL CRANK(N,WKSP2,SG)
D=0.
DO 12 J=1,N
    D=D+(WKSP1(J)-WKSP2(J))**2
12  CONTINUE
EN=N
EN3N=EN**3-EN
FAC=(1.-SF/EN3N)*(1.-SG/EN3N)
RS=(1.-(6./EN3N)*(D+0.5*(SF+SG)))/FAC
AVED=EN3N/6.-(SF+SG)/12.

```

```
VARD=((EN-1.)*EN**2*(EN+1.)**2/36.)*FAC
ZD=(D-AVED)/SQRT(VARD)
PROBD=ERFCC(ABS(ZD)/SQRT(2.0))
T=RS*SQRT((EN-2.)/(((1.+RS)+TINY)*((1.-RS)+TINY)))
DF=EN-2.
PROBRS=BETAI(0.5*DF,0.5,DF/(DF+T**2))
RETURN
END
```